國立臺灣大學工學院化學工程學系

碩士論文

Department of Chemical Engineering

College of Engineering

National Taiwan University

Master’s Thesis

醇類輔助低溫二氧化碳氫化生成甲醇：觸媒研發及反應機制探討

Low-Temperature Methanol Synthesis via Alcohol-Assisted CO$_2$ Hydrogenation: Catalyst Development and Mechanistic Investigation

劉紫冰

Zhi Pin Law

指導教授：游文岳 博士

Advisor: Wen-Yueh Yu, Ph.D.

中華民國 114 年 07 月

July, 2025

doi:10.6342/NTU202502278

國立臺灣大學碩士學位論文
口試委員會審定書
MASTER THESIS ACCEPTANCE CERTIFICATE
NATIONAL TAIWAN UNIVERSITY

醇類輔助低溫二氧化碳氫化生成甲醇：觸媒研發及反應機制探討

Low-Temperature Methanol Synthesis via Alcohol-Assisted
CO_2 Hydrogenation: Catalyst Development and Mechanistic Investigation

本論文係 劉紫冰 (R12524135) 在國立臺灣大學 化學工程學系 完成之碩士學位論文，於民國 114 年 7 月 11 日承下列考試委員審查通過及口試及格，特此證明。

The undersigned, appointed by the Department of Chemical Engineering on 2025/7/11, have examined a Master's Thesis entitled above presented by Law Zhi Pin (R12524135) candidate and hereby certify that it is worthy of acceptance.

口試委員 Oral examination committee:

游文岳 李奕霈

（指導教授 Advisor）

吳紀聖 陳靖天

系（所、學位學程）主管 Director: 廖英志

doi:10.6342/NTU202502278

致謝

自 2023 年 8 月 26 日以非旅遊的目的入境台灣，8 月 28 日第一次到鄭江樓 N511 報到，直到今日，我想感謝的人不勝枚舉。

首先，我想感謝我的指導教授，游文岳老師。感謝老師僅透過一次線上會議，就決定“賭一把”接納我成為您的學生。老師可以說是我在觸媒領域的啟蒙者，從觸媒化學課、實驗研究、邏輯思考到成果報告，我都在老師的指導與幫助下收穫良多。更因為老師的鼓勵，讓我有了繼續在學術界努力的信心。

謝謝三位口試委員：吳紀聖老師、李奕霈老師和清大化工陳靖天老師撥冗參與我的論文口試，提出許多專業的建議與指導，讓我可以修正論文的不足，使這項研究更趨完善。同時也要謝謝李老師實驗室的陳景淳同學於 DFT 計算的付出，讓我可以有實驗數據以外的證據，勾勒出可能的理論機制。

實驗室的成員中，首先要感謝的當然是致豪。感謝學長一路拉拔我成長，從我還是個小菜鳥開始，耐心一步一步引導我，到現在仍持續為我答疑解惑。從實驗精神到報告整理，我都深受你的影響。雖然可能只是你無心的一句話，但你曾說過:“有壓力才會進步”，我印象非常深刻。儘管你拋下我跑到 deNOx 組、時常情勒我、慫恿我花錢，我還是很感謝你願意和我討論數據、給我建議。一日學長、終身學長，您的大恩大德，我沒齒難忘！再來是沉穩可靠的昱碩學姐。有時候我糾結老半天，只要妳輕輕一點，什麼問題都立刻豁然開朗！非常感恩二位曾在我情緒崩潰的時候，給了我極大的安慰與支持。在我眼中，你們是閃閃發亮、特別耀眼的人哦！

感謝珊妮和韋丞，總是在我需要的時候和我一起討論數據、抱團取暖。還要特別感謝韋丞讓我深刻體會到台灣人對諧音梗的執著，更重要的是幫我搶演唱會門票！謝謝恩琪和昀容，兩位貼心的小天使，願意聽我分享追星的快樂。謝謝承晏、孝元和禹辰，在我忙得焦頭爛額的時候幫我處理大小事，減輕我的負擔。雖然接觸時間不長，但也想感謝已經畢業的學長姐，夢蝶、冠博、Kantika 和 Stang，在我需要時給予我幫助。感謝楷融大掌櫃，總是滿足我們大大小小的需求，也常陪我一起嘆氣、感嘆人生。謝謝董哥的關心與鼓勵。如果沒有董哥和鄭崢，我的流力、熱質傳和中等數值可能就無法及格了。還有菡書、鋕偉、妍安、翊安、任佑和沛如，也

doi:10.6342/NTU202502278

謝謝你們為我的碩班生活增添許多色彩。

謝謝親來阿姨在非親非故的情況下常常請我們吃飯。此外，也感謝遠在馬來西亞和新加坡的朋友們，即使工作繁忙，仍持續與我聯絡，遠端陪我度過開心與難過的時光。當然還要謝謝我的精神糧食—五月天和 Super Junior。

感謝爸爸媽媽和哥哥支持我出國留學的決定，讓我可以無後顧之憂地專心求學。謝謝阿姨、舅舅和表妹們，在我和姊姊不在家的時候，陪伴著媽媽。另外，最最最最感謝的就是我姊姊。每當我遇到挫折，妳總能精準且有效地安慰並鼓勵我。從研究困境、未來發展，到娛樂追星、渡假旅行，因為有妳，我才不會覺得孤單。謝謝妳一直走在我前面，讓我可以放心地、勇敢地走在妳走過的路上。無論未來我們身在何處，我永遠是妳的頭號粉絲！

最後，我想要感謝我自己。雖然研究過程跌跌撞撞、充滿疲憊，但我撐過來了。不論生活還是學術，我都因為這些困難與挑戰而成長了不少。接下來，我也會繼續努力，健康且快樂地迎接所有挑戰。

“某一天、某一刻、某次呼吸，我們終將再分離。而我的自傳裡曾經有你，沒有遺憾的詩句，詩句裡充滿感激”——《如果我們不曾相遇》by 五月天。由衷地感謝所有人，也感謝自己，讓「赴台灣念研究所」這個決定，成為我目前人生中最勇敢、也最無悔的選擇。

劉紫冰　僅誌
2025 年 7 月
於台灣大學化學工程學系鄭江樓 N511 室

doi:10.6342/NTU202502278

摘要

本研究旨在探討乙醇輔助二氧化碳(CO_2)氫化低溫合成甲醇之反應機制。所使用之觸媒為以共沉澱法製備的 $CuZnCeO_x$ 系列觸媒。研究表明，甲酸乙酯(EtFm)為關鍵中間體，係由 CO_2 與 H_2 生成的甲酸根與催化溶劑乙醇反應形成。該中間體經加氫裂解(hydrogenolysis)可快速轉化為甲醇，從而降低 CO_2 氫化合成甲醇的反應溫度。鑒於過去研究多以銅鋅氧化物作為觸媒，本研究引入鈰(Ce)作為促進劑，探討其對與甲醇產率及選擇率之影響。

觸媒活性測試結果顯示，相較於 CuZnO，部分以 Ce 取代 Zn 可提升 EtFm 及甲醇的生成量。透過調控 Ce 與 Zn 的比例，本研究進一步釐清兩者在反應中的角色。Ce 有助於促進 EtFm 的生成，惟過量的 Ce 則會抑制其後續轉化為甲醇；相對的，Zn 則可有效促進 EtFm 經由氫解反應生成甲醇。研究結果顯示，適量添加 Ce 不僅有助於中間體 EtFm 的生成，亦能兼顧其高效轉化，進一步提升甲醇之產率與選擇率。

本研究使用原位擴散反射紅外線傅立葉轉換光譜(in-situ DRIFTS)技術，探討 Ce 與 Zn 在反應機制中所扮演的角色。光譜結果顯示，乙酸乙酯(EtFm)在 CuZnO 上的訊號較弱且持續時間短，顯示其吸附較弱並易於轉化；相對地，在 $CuCeO_2$上則觀察到較強且持續時間較長的 EtFm 吸附訊號，顯示其在表面具有較強的吸附力。根據這些觀察，推論 EtFm 在 Ce 含量較高的觸媒上傾向以單點氧(η^1-O)模式吸附於表面，造成氫解反應受阻，進而降低其轉化效率；而 Zn 含量較高的觸媒則促進 EtFm 以雙點碳氧(η^2-(C,O))模式吸附，有助於羰基活化，進一步與銅表面解離之氫反應，有效轉化為甲醇。

綜上所述，本研究指出促進劑表面之吸附結構為影響觸媒性能的關鍵因素，並提出可藉由調控觸媒組成，達成提升甲醇生成效率、抑制副反應之設計準則，對推動高效、低溫 CO_2 氫化生成甲醇製程的發展具有實質貢獻。

關鍵字：二氧化碳、甲醇、銅觸媒、鈰、紅外線光譜

ABSTRACT

This study investigates ethanol (EtOH)-assisted CO_2 hydrogenation for low-temperature methanol (MeOH) synthesis using a series of $CuZnCeO_x$ catalysts synthesized *via* the co-precipitation method. Ethyl formate (EtFm) is identified as a key intermediate, formed through the reaction between formate species (derived from CO_2 and H_2) and EtOH, which serves as a catalytic solvent. Subsequent hydrogenolysis of EtFm enables MeOH production at temperatures lower than those required for conventional CO_2 hydrogenation. While previous studies have focused primarily on CuZnO system, this work introduces cerium (Ce) as a promoter aimed at improving MeOH yield and selectivity.

Catalytic testing demonstrated that partial substitution of Zn with Ce markedly increases EtFm formation and concurrently boosts MeOH yield compared to CuZnO. Systematic variation of the Ce/(Ce+Zn) ratio revealed bifunctional behavior: Ce promotes EtFm generation but excessive Ce content shows inhibitory effect in EtFm conversion, whereas Zn effectively converts EtFm into MeOH *via* hydrogenolysis. An optimal Ce/Zn ratio was identified, achieving a balance between intermediate formation and conversion, resulting in the optimal MeOH yield and selectivity.

Based on the results of in-situ DRIFT spectroscopy, this study proposes that the adsorption configuration of ethyl formate (EtFm) on the catalyst surface is a key factor governing the distinct catalytic behaviors. Spectral observations revealed that the EtFm signal on CuZnO was relatively weak and short-lived, suggesting weak adsorption and facile conversion. In contrast, $CuCeO_2$ exhibited a stronger and more persistent EtFm signal, indicating stronger surface binding. These differences imply that EtFm is preferentially stabilized in an η^1-O adsorption geometry on Ce-rich catalysts, which

doi:10.6342/NTU202502278

inhibits hydrogenolysis to methanol (MeOH). Conversely, Zn-rich catalysts promote an η^2-(C,O) adsorption mode that facilitates C=O activation and enables effective conversion to MeOH via surface hydrogen species. These findings underscore the crucial role of adsorption geometry in determining reaction pathways and product selectivity. This work offers valuable design principles for optimizing Cu-based catalysts in alcohol-assisted CO_2 hydrogenation, paving the way for efficient, low-temperature MeOH synthesis.

Keywords: carbon dioxide, methanol, copper catalysts, cerium, infrared spectroscopy

TABLE OF CONTENTS

doi:10.6342/NTU202502278

LIST OF FIGURES

doi:10.6342/NTU202502278

LIST OF TABLES

LIST OF APPENDICES

doi:10.6342/NTU202502278

CHAPTER 1 INTRODUCTION

1.1 Research Background

1.1.1 CO_2 Utilization

Although alternative and unconventional energy sources have advanced, fossil fuels continue to dominate the global energy landscape, with no foreseeable large-scale replacement. The continued reliance on fossil fuels along with growing industrial activities, has led to a sustained increase in CO_2 emissions, a primary driver of climate change.[1] As illustrated in **Figure 1.1**, global annual CO_2 emissions per capita have increased significantly since the 1850s, reaching 4.7 tonnes in 2023.[2] Furthermore, total CO_2 emissions are projected to rise from 40.6 billion tonnes in 2023 to 41.6 tonnes in 2024. According to the Global Carbon Budget, fossil fuel combustion accounts for 37.4 billion tonnes of these emissions, with the remainder primarily attributed to deforestation.[3]

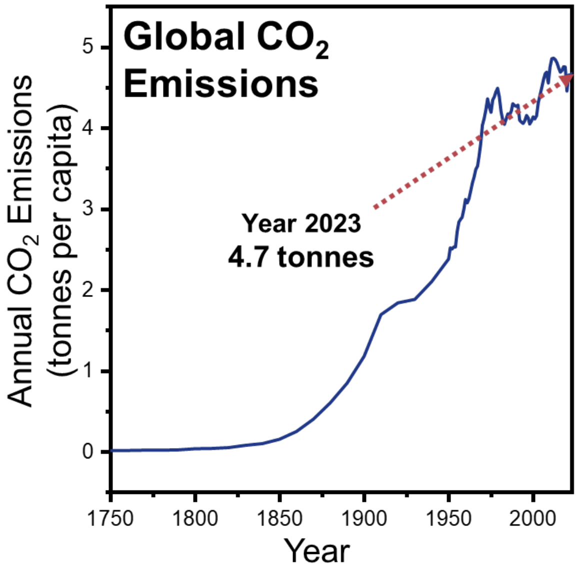

Figure 1.1 Global CO_2 emissions from fossil fuels and industry.

doi:10.6342/NTU202502278

To mitigate the escalating CO_2 emissions and their environmental impact, the integration of CO_2 capture with subsequent conversion processes has become an urgent priority. CO_2 valorization strategies are generally categorized into direct utilization and chemical conversion into fuels or high-value chemicals. Small-scale applications of CO_2 include its use in carbonated beverages, dry ice production, fire extinguishers, and refrigerants. On a larger scale, CO_2 can be utilized to enhance industrial processes, such as enhanced oil recovery (EOR), enhanced gas recovery (EGR), and enhanced geothermal systems (EGS). It is important to note that direct utilization do not alter the molecular structure of CO_2.[4]

As an alternative approach, the chemical conversion of CO_2 into fuels and chemicals presents a promising solution for reducing atmospheric CO_2 levels. This transformation can be categorized into reductive and non-reductive processes, as illustrated in **Figure 1.2.**

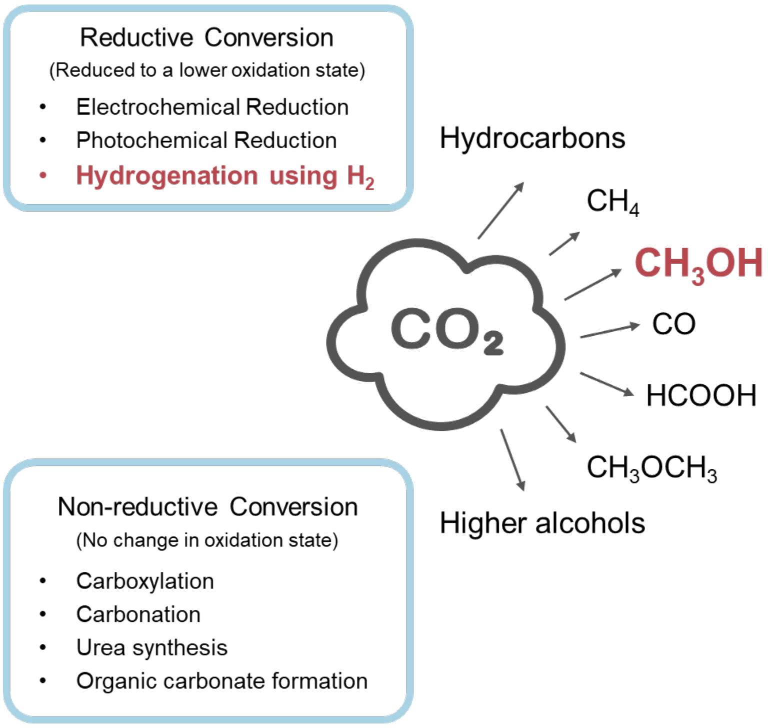

Figure 1.2 Chemical (reductive and non-reductive) conversion of CO_2.

As its name implies, non-reductive conversion preserves the oxidation state of the carbon atom (+4) throughout the reaction. This process offers several advantages, primarily its lower energy requirement compared to reductive conversion, as it does not involve altering the carbon atom's oxidation state. Moreover, the utilization of CO_2 in this approach can eliminate the need for certain toxic reagents traditionally used in industrial processes, such as phosgene and carbon monoxide required for urea synthesis, thereby enhancing both environmental and operational sustainability.[5]

Despite these benefits, reductive conversion stands out as a particularly attractive approach for CO_2 utilization. This method enables the transformation of CO_2 into energy-dense compounds that can function as fuels or chemical feedstocks. By reducing CO_2 into valuable C1 or C2+ species, reductive conversion transforms "waste" carbon into "useful" carbon, offering a sustainable route for carbon recycling and energy generation.[6] Hydrogen, a high-energy material, is a promising reductant for CO_2 reduction due to the thermodynamic stability of CO_2.[7] The products resulting from CO_2 hydrogenation are shown in **Figure 1.2**. Among these products, methanol (MeOH) and dimethyl ether (DME) are highly efficient fuels for combustion engines, while MeOH and formic acid are widely used as key building blocks in the chemical industry.

1.1.2 CO_2 Hydrogenation for Methanol Synthesis

MeOH is a fundamental bulk chemical in the chemical industry.[8] Due to its high octane rating, it is often used as an additive in gasoline for internal combustion engines, modifies diesel engines, or direct MeOH fuel cells, where it can be converted into electrical power by harnessing its chemical energy.[9] Furthermore, MeOH serves as a key feedstock for a range of chemicals, including formaldehyde, acetic acid, and methyl *tert-*

doi:10.6342/NTU202502278

butyl ether. It can also be converted into ethylene and propylene, the foundational building blocks of polymers, through the methanol-to-olefins (MTO) process. In 2023, global MeOH demand reached 91 million metric tons, with projections indicating an additional increase of 17 million metric tons over the following five years.[10] MeOH is typically synthesized from syngas, a mixture of CO, CO_2, and H_2, which can be obtained from various carbon feedstocks through gasification. CO_2 is incorporated to balance the C/H ratio, as CO_2 consumes more hydrogen than CO, as shown in **Equations 1.1 and 1.2**.[11]

$CO_2 + 3H_2 \leftrightarrow CH_3OH + H_2O$ $\Delta H_{298K} = -49.16$ kJ/mol **Equation 1.1**
$CO + 2H_2 \leftrightarrow CH_3OH$ $\Delta H_{298K} = -90.77$ kJ/mol **Equation 1.2**
$CO_2 + H_2 \leftrightarrow CO + H_2O$ $\Delta H_{298K} = +41.21$ kJ/mol **Equation 1.3**

Due to its low cost and abundance, CO_2 conversion into MeOH presents a viable industrial opportunity. The transforming CO_2 into value-added chemicals, particularly MeOH – a high-demand chemical – offers both a viable strategy for mitigating climate change and a sustainable approach to chemical production. MeOH synthesis from CO_2 can proceed *via* two primary pathways: (1) direct hydrogenation of CO_2 (**Equation 1.1**) or (2) an indirect route involving the reverse water-gas shift (RWGS) reaction to convert CO_2 into CO (**Equation 1.3**), followed by subsequent CO hydrogenation (**Equation 1.2**). Both pathways must be considered when CO_2 serves as the primary feedstock.[11]

The industrial production of MeOH dates back to 1923 when BASF developed the first MeOH plant using syngas as the feedstock.[1] In contrast, the first pilot plant for CO_2-to-methanol conversion was established much later, in 1994.[11] Since then, Cu/Zn-based catalysts have been extensively studied for this reaction; however, the nature of the active sites responsible for CO_2 hydrogenation to MeOH remains a subject of debate. While some suggest that Zn primarily acts as a structural spacer, improving Cu dispersion during catalyst preparation, others argue that the reaction occurs on metallic Cu surfaces, the Cu-ZnO_x interface, or CuZn alloys.[1]

Recent studies have further explored the role of different oxidation states of Cu in this reaction. For instance, Wei Huang and his co-workers demonstrated that metallic Cu (Cu^0) and Cu^+ serve as the main active sites for CO_2 and CO hydrogenation, respectively, during MeOH synthesis.[12] Similarly, Robert Schlögl and his team investigated the active sites of MeOH synthesis over $Cu/ZnO/Al_2O_3$ catalysts and identified two key factors contributing to high activity: the stabilization of stepped Cu sites by bulk defect, which enhances intermediate binding, and a dynamic strong metal-support interaction (SMSI) effect that promotes ZnO_x coverage.[13] Beyond active site composition, other factors such as Cu loading[14] and Cu particle size[15] have also been studied to optimize catalytic performance. Additionally, catalyst supports have been widely investigated for their role in enhancing Cu dispersion[16] and modifying the electron state of Cu[17], further improving the activity, selectivity and stability of catalysts.

Despite these advancements, several challenges remain in MeOH synthesis from CO_2 hydrogenation. One major limitation is the thermodynamic constraints of the reaction. As shown in **Equations 1.3**, the total number of moles decreases from reactants to products during the hydrogenation of CO_2 to MeOH. Additionally, while the hydrogenation of CO_2 and CO to MeOH is exothermic, the reverse water-gas shift reaction is endothermic.[18] According to Le Chatelier’s principle, higher pressures and lower temperatures favor MeOH formation by shifting the equilibrium, thereby enhancing selectivity. However, a higher reaction temperature is always necessary in converting CO_2 into MeOH due to the stable intermediates during the reaction.

doi:10.6342/NTU202502278

1.2 Alcohol-Assisted CO_2 Hydrogenation for Methanol Synthesis

Developing a low-temperature approach for MeOH synthesis from CO_2 is crucial for reducing production costs and leveraging thermodynamic advantages that significantly enhance MeOH selectivity. As previously mentioned, two primary reaction pathways have been proposed for CO_2-to-methanol conversion: (1) the formate (**Equation 1.1**) and (2) the RWGS followed by CO hydrogenation pathway (**Equations 1.2 and 1.3**).[19] The formate pathway, illustrated in **Figure 1.3**, has been identified as the lower-energy route, where the hydrogenation of the methoxy intermediate to MeOH serves as the rate-limiting step, particularly when a high CO_2 feed ratio is used.[20]

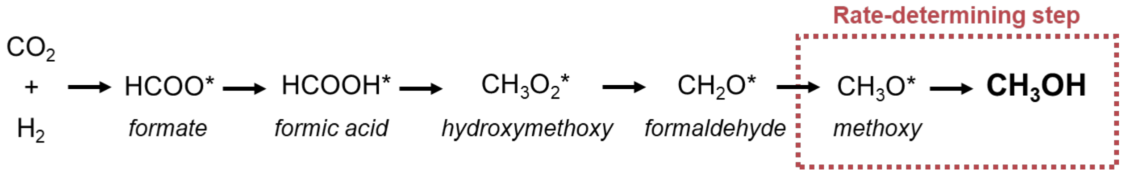

Figure 1.3 Mechanism of conventional CO_2 hydrogenation for methanol (MeOH) synthesis.

Conventional CO_2 hydrogenation typically requires high temperatures and pressures to convert methoxy species into MeOH. To overcome these thermodynamic limitations, Tsubaki and his team proposed a novel low-temperature MeOH synthesis method using alcohol as a catalytic solvent, which alters the reaction intermediates.[21] Compared to the conventional route, which operates at 300 – 350 °C and 50 – 100 bar [9], the alcohol-assisted method enables MeOH synthesis under significantly milder conditions, typically 150 – 170 °C and 30 – 50 bar, when ethanol (EtOH) is used as the catalytic solvent.[21]

Figure 1.4 shows the proposed alcohol-assisted CO_2 hydrogenation pathway for low-temperature MeOH synthesis with syngas ($CO/CO_2/H_2$) as the feedstock. In the presence of water, CO undergoes a water-gas shift reaction to generate CO_2 and H_2 (step 1). The resulting CO_2 then reacts with H_2 to form formate (HCOO) species (step 2), following a mechanism similar to the conventional pathway shown in **Figure 1.3**. In step 3, alcohol (ROH) reacts with HCOO to form alkyl formate (HCOOR), which subsequently undergoes hydrogenolysis to regenerate ROH and yield MeOH as the desired product (step 4). The rapid conversion of alkyl formate into MeOH lowers the required reaction temperature and pressure, enabling milder conditions for MeOH synthesis *via* CO_2 hydrogenation.

Using i*n-situ* diffuse reflectance infrared Fourier transform spectroscopy (DRIFTS), Tsubaki and his co-workers revealed that the key intermediate, ethyl formate (EtFm), is formed by the reaction of adsorbed formate (HCOO*) with gas-phase EtOH (catalytic solvent). Both gas-phase and physisorbed EtFm are reduced by hydrogen atoms, leading to the formation of gas-phase MeOH.[22]

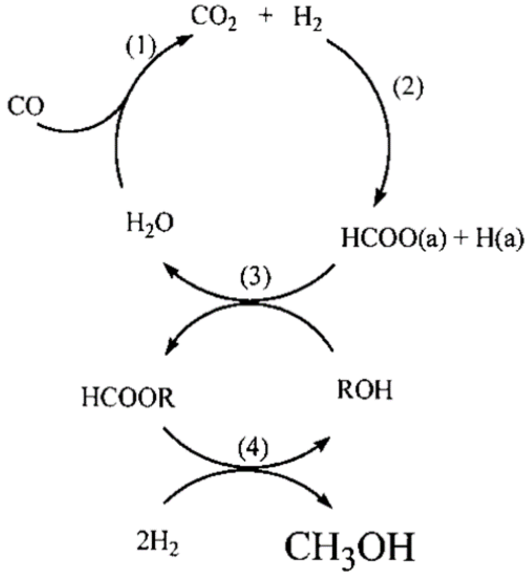

Figure 1.4 Mechanism of alcohol-assisted CO_2 hydrogenation for methanol (MeOH) synthesis.[21]

As illustrated in **Figure 1.5**, Tsubaki's team has published a total of 50 studies on low-temperature MeOH synthesis using alcohol as a catalytic solvent. **Figure 1.6** summarizes the catalysts employed in these studies, with Cu/ZnO being the most commonly used, followed by Cu/MgO, Cu/ZnO/Al_2O_3, and Cu/ZnO/SiO_2.

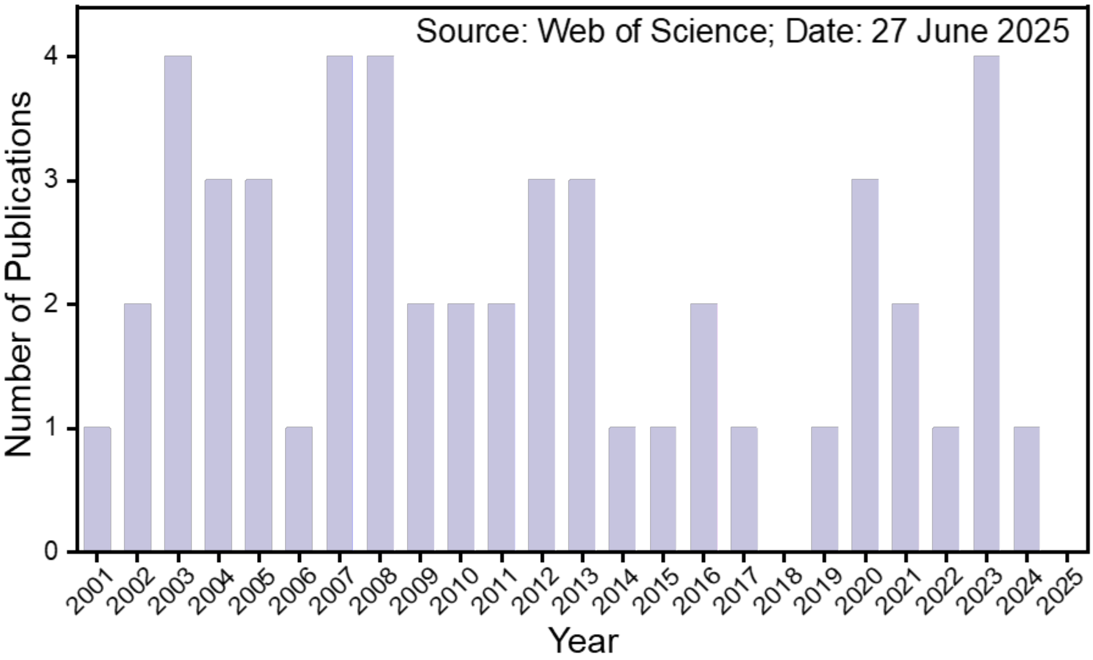

Figure 1.5 Publications of Tsubaki and his team regarding alcohol-assisted CO_2 hydrogenation from 2001 to 2025. Source: Scopus; Keywords: low-temperature methanol synthesis.

Jung and his team have investigated the influence of Cu/ZnO catalyst preparation on EtOH-assisted CO_2 hydrogenation for MeOH production. Their studies found that Cu/ZnO synthesized at a pH of 8 [23] and subjected to an aging time of 5 hours [24] exhibited optimal catalytic performance and structural stability. Additionally, they demonstrated that a Cu/ZnO catalyst with a Cu/(Cu+Zn) molar ratio of 0.5 achieved high copper dispersion and sufficient acid sites, resulting in the highest MeOH yield.[25] Similarly, Kim-Lohsoontorn and her co-workers reported that a precipitation temperature of 60 °C and a pH value of 8 led to the smallest crystalline size and highest catalyst dispersion, thereby maximizing MeOH yield.[26] Furthermore, the same group investigated the effect of molecular sieves (3A, 5A and a combination of 3A+5A) by physically mixing them with Cu/ZnO catalysts. Their findings revealed that MeOH yield improved due to the enhanced water adsorption provided by the 3A molecular sieve.[27] Beyond Cu/ZnO catalysts, other copper-based systems such as Cu/Cr_2CuO_4, Cu/Mo_2C [28] have also been explored for alcohol-assisted CO_2 hydrogenation. Additionally, Pd-supported catalysts, including Pd/ZnO, Pd/Al_2O_3, Pd/SiO_2 [29] and Pd/MgO [30] have also been investigated for their potential to enhance catalytic performance under similar reaction conditions.

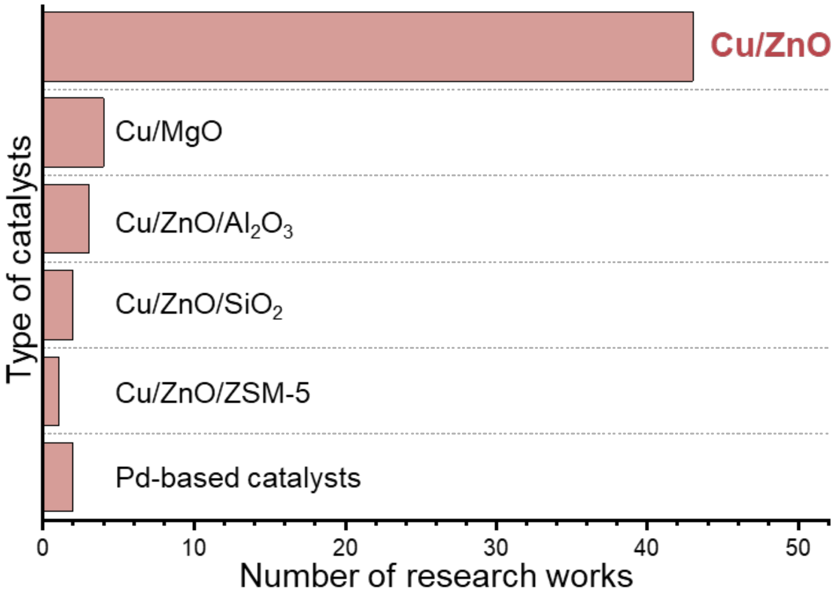

Figure 1.6 Catalysts studied in the previously reported works by the group of Tsubaki, N., Jung, J. C.[23-25,31], Kim-Lohsoontorn, P.[26,32], Thompson, L. T.[33], Nieminen, H.[34], D. J. Heldebrant[29,35], and Lin, H. F.[30]

doi:10.6342/NTU202502278

1.3 Alcohol Dehydrogenation as Side Reactions

In this low-temperature MeOH synthesis method, alcohol serves as a catalytic solvent and is theoretically not consumed during the reaction. However, its interaction with the catalyst is unavoidable, often leading to the formation of undesired side products. Kim-Lohsoontorn and her team investigated the influence of alcohol type on catalytic performance and found that n-alcohols exhibited superior performance compared to branched alcohols, with MeOH yield decreasing as the size of the alcohol molecule increased.[32] The lower reactivity of branched alcohols was attributed to their higher steric hindrance, which hindered nucleophilic attack on formate species, thereby reducing MeOH yield.[21] Their study also revealed that different alcohols produced distinct by-products through dehydrogenation, as summarized in **Table 1.1**.

Table 1.1 By-products of different alcohols.

n-Alcohols	By-products	Branched alcohols	By-products
Ethanol	Ethyl acetate	2-propanol	Acetone
1-propanol	Propyl propanoate	2-butanol	Methyl ethyl ketone
1-butanol	Butyl butanoate	Iso-butanol	Isobutyl isobutyrate
1-pentanol	Pentyl pentanoate		

Ethyl acetate (EtAc), acetone, and methyl ethyl ketone – the dehydrogenation and coupling products of EtOH, 2-propanol, and 2-butanol, respectively – form azeotropic mixtures with MeOH, creating separation challenges after the reaction.[32] For instance, the boiling point of MeOH is 64.7 °C, whereas the boiling point of EtAc (EtOH coupling product) is 77.1 °C. It has been reported that, compared to 1-propanol, EtOH resulted in a higher MeOH yield; however, it simultaneously resulted in a higher selectivity of by-

doi:10.6342/NTU202502278

products (i.e. EtAc), complicating the post-reaction product purification.[32] Therefore, it is essential to investigate the factors that promote or inhibit the side reaction. The mechanism of EtOH dehydrogenation over Cu-based catalysts has been reported by Hanukovich *et al.* [36], while the pathway for EtAc formation from EtOH has been elucidated by Colley *et al.* [37] and Wu *et al.*[38] A comprehensive mechanism that integrates both reactions was then proposed by Phung [39], and is summarized as follows from step 1 to step 4.

$$C_2H_5OH \rightarrow C_2H_5O^* + H^* \qquad \text{(Step 1)}$$

$$C_2H_5O^* \rightarrow CH_3CHO + H^* \qquad \text{(Step 2)}$$

$$CH_3CHO^* \rightarrow CH_3CO^* + H^* \qquad \text{(Step 3)}$$

$$CH_3CO^* + C_2H_5O^* \rightarrow CH_3COOC_2H_5 \qquad \text{(Step 4)}$$

In the proposed mechanism, EtOH (C_2H_5OH) adsorbs to the acid site of support and dissociates by O-H bond cleavage, whereby ethoxy species ($C_2H_5O^*$) are formed on acid sites while the H radical (H*) is adsorbed on the basic support (step 1). The ethoxy species is converted into MeCHO (CH_3CHO) *via* $C\alpha$-H bond cleavage (step 2), after which it can either desorb or adsorb to further convert into acetyl species (CH_3CO^*) by another C-H bond cleavage (step 3). Then, the adsorbed ethoxy and acetyl species react to form EtAc ($CH_3COOC_2H_5$) species (step 4). The mechanism is summarized in **Figure 1.7**, in which both ethoxy and acetyl species are necessary for the formation of EtAc.

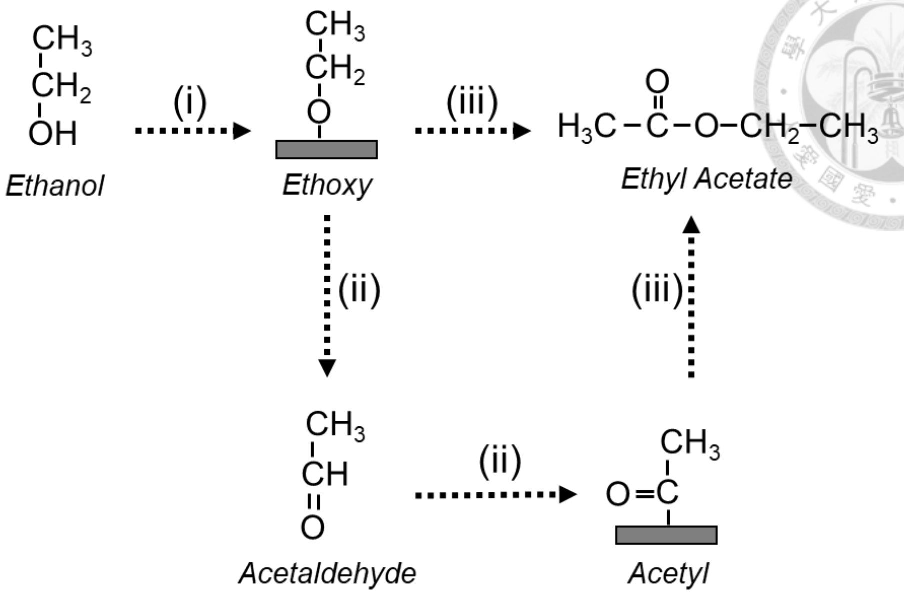

Figure 1.7 Formation of acetaldehyde (MeCHO) and ethyl acetate (EtAc) *via* (i) dissociation, (ii) dehydrogenation and (iii) coupling of ethanol (EtOH).

doi:10.6342/NTU202502278

1.4 Research Objectives

CuZnO-based catalysts represent the benchmark for EtOH-assisted CO_2 hydrogenation to MeOH. However, further advancements in activity and selectivity remain essential to meet the demanding efficiency and sustainability requirements for industrial deployment. Previous studies had identified that key structural properties, namely smaller particle size, higher copper dispersion, and increased specific surface area, play decisive roles in enhancing the performance of these catalysts under EtOH-assisted conditions.[23-26]

In conventional CO_2 hydrogenation, the methanol synthesis rate is well known to correlate with the accessible metallic Cu surface area.[40] Finely dispersed Cu nanoparticles provide a higher density of active sites, thereby enabling more efficient CO_2 conversion. Therefore, strategies that enhance copper dispersion are vital to advancing catalyst efficacy.[41] Among various promoters, ceria (CeO_2) has emerged as a highly attractive candidate due to its multifunctional contributions to catalyst design and performance. When incorporated into Cu-based catalysts, CeO_2 establishes strong metal-support interaction (SMSI) with Cu species, which not only promotes the formation of smaller Cu nanoparticles but also enhances interfacial contact between Cu and the support.[42] Consequently, $CuCeO_2$ systems often exhibits a greater exposed Cu surface area than their CeO_2-free counterparts, directly translating into higher catalytic activity for CO_2 hydrogenation.

Beyond improving copper dispersion, CeO_2 also contributed critically to CO_2 activation. Its exceptional oxygen storage capacity, driven by the facile Ce^{4+}/Ce^{3+} redox cycle and the dynamic formation of oxygen vacancies, enables effective CO_2 adsorption and polarization, [43] facilitating their conversion into reactive intermediates such as formate species.[44] The stabilization of formate species is critical, as they serves as key precursors in MeOH formation pathways. Importantly, this promotional effect extends to EtOH-assisted CO_2 hydrogenation, where the formation of ethyl formate (EtFm) serves as a central mechanistic step.

In summary, this research is motivated by the hypothesis that ceria-promoted CuZnO catalysts can surpass the performance limitations of conventional systems by leveraging the multifunctionality of CeO_2. Through enhancing copper dispersion, accelerated CO_2 activation, and improved intermediate stabilization, CeO_2 address the fundamental challenges currently constraining catalytic efficiency. The rational integration of CeO_2 into the Cu/ZnO matrix is thus anticipated to unlock new levels of activity and selectivity, propelling EtOH-assisted CO_2 hydrogenation toward more viable and practicable MeOH production route.

doi:10.6342/NTU202502278

CHAPTER 2 METHODOLOGY

2.1 Chemicals and Reagents

Table 2.1 Chemicals and reagents used in this study.

Chemical Name	**Chemical Formula**	**Brand**	**Purity**
Copper(II) nitrate trihydrate	$Cu(NO_3)_2 \cdot 3H_2O$	Thermo	99%
Zinc nitrate hexahydrate	$Zn(NO_3)_2 \cdot 6H_2O$	Acros	98%
Cerium(III) nitrate hexahydrate	$Ce(NO_3)_3 \cdot 6H_2O$	Acros	99.5%
Sodium Carbonate	Na_2CO_3	Showa	99.5%
Ethanol	C_2H_5OH	Echo Chemical	99.5%
Methanol	CH_3OH	Acros	99.8%
Acetaldehyde	CH_3CHO	Thermo	98.5%
Ethyl formate	$HCOOC_2H_5$	Thermo	97%
Ethyl acetate	$CH_3COOC_2H_5$	Fisher	99.8%
n-decane	$C_{10}H_{22}$	Alfa	99%

doi:10.6342/NTU202502278

2.2 Catalyst Preparation

The catalysts in this study were synthesized using the co-precipitation method. **Table 2.2** summarizes the targeted molar ratios of Cu, Zn and Ce used for systematic comparison. The co-promoted catalysts are denoted as $CuZnCeO_x$(Y), where Y indicates the molar ratio of Ce/(Ce+Zn).

Table 2.2 Molar ratios of Cu, Zn, and Ce for each catalyst sample.

Catalyst	**Cu:Zn:Ce (molar ratio)**
CuZnO	1:1:0
$CuZnCeO_x$(0.2)	5:4:1
$CuZnCeO_x$(0.4)	5:3:2
$CuZnCeO_x$(0.75)	4:1:3
$CuCeO_2$	1:0:1

Each metal nitrate was precisely weighed and dissolved in 40 mL of deionized water to prepare 1M precursor solutions. These solutions were then mixed in designated ratios to form an 80 mL mixture. Separately, a 1.5 M sodium carbonate (Na_2CO_3) solution was prepared as the precipitating agent. The metal precursor mixture and the Na_2CO_3 solution were transferred into separate burettes. A beaker containing 300 mL of deionized water and a magnetic stirrer was placed on a hot plate and maintained at 65 °C and 350 rpm. The metal precursor mixture was added dropwise to the beaker, while the Na_2CO_3 solution was simultaneously added dropwise to maintain a constant pH of 8. The setup for co-precipitation is shown in **Figure 2.1**. Once all the metal precursor solution was added, the mixture was stirred at 65 °C for 1 hour and then left undisturbed overnight for sedimentation.

doi:10.6342/NTU202502278

The precipitate was separated by centrifugation and washed with deionized water until the rinse water reached a neutral pH. The solid was then dried overnight in a vacuum oven and ground into a fine powder using a mortar and pestle. The resulting powder was calcined at 350 °C for $CuCeO_2$ and 500 °C for catalysts containing ZnO, using a heating rate of 10 °C/min for 5 hours. Before the catalytic activity test, the catalyst was reduced in a 50% H_2/N_2 atmosphere at 300 °C with a heating rate of 10 °C/min for 3 hours to ensure complete reduction of copper to its metallic state.

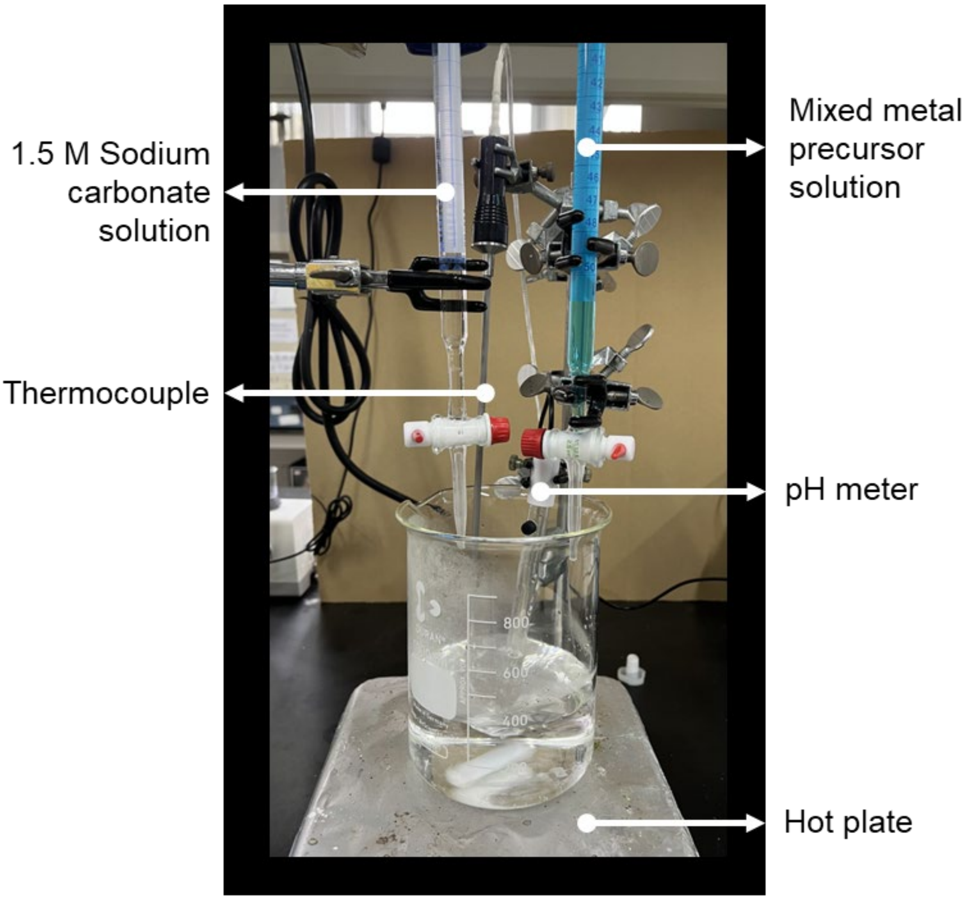

Figure 2.1 Experimental setup for catalyst preparation *via* the co-precipitation method.

doi:10.6342/NTU202502278

2.3 Catalytic Activity Test and Product Characterization

2.3.1 Reaction System

The high-pressure batch reactor used in this study was a 100 mL Parr 4760 reactor. 50 mg catalyst, 20 mL of ethanol (EtOH), and a magnetic stirrer were placed in the reactor, which was then sealed with a cap equipped with a pressure gauge and gas valves. The reactor was purged with nitrogen (N_2) five times to remove any residual air. Subsequently, CO_2 was introduced at 7.5 bar, followed by hydrogen (H_2) at 22.5 bar. Notably, each feeding of gas was held for 2 minutes to ensure gas equilibrium in the reactor. The reactor was then positioned on a hot place and stirred at 600 rpm. As shown in **Figure 2.2**, the bottom section of the reactor was surrounded by a heating ring connected to a temperature controller, while a thermocouple installed at the top of the reaction monitored real-time temperature changes and transmitted signals to the controller. The reaction time was recorded only after the reaction temperature (150 °C) was reached.

Upon completion of the reaction, the reactor was placed in an ice bath to cool to room temperature. Before detaching the cap, part of the gas was transferred to a gas bag for gas-phase product characterization, whereas the residual gas was carefully released in a fume hood. Subsequently, 100 μL of internal standard (n-decane) was added to the reactor prior to collecting the liquid product for characterization. A syringe filter was used to separate the catalyst, and the resulting filtrate was stored in vial bottles for further analysis.

doi:10.6342/NTU202502278

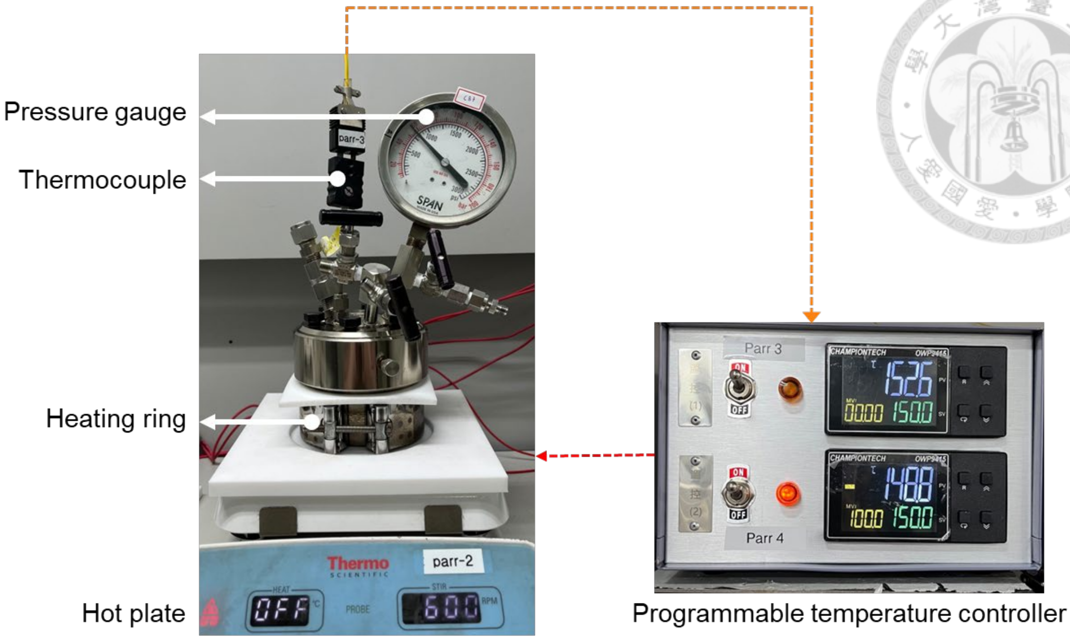

Figure 2.2 Experimental setup of catalytic activity tests.

2.3.2 Gas Chromatography with Flame Ionization Detector (GC-FID)

In this study, the quantitative analysis of reaction products was conducted using gas chromatography equipped with flame ionization detector (GC-FID). When the sample is injected through the injection port, it is instantly vaporized and carried by the mobile phase into the analytical column. Within the column, differences in interactions between the analytes and the stationary phase facilitate the separation of compounds, leading to variations in retention times. The analytes are then combusted in a hydrogen-air mixture and subsequently ionized in the detector. Under a high-voltage electric field, the resulting ions generate an ion flow, which is amplified and recorded as a detectable signal.

The model of GC-FID used is Agilent 6890N, while the model of column used is DB-WAX with 5N nitrogen (99.999% N_2) as mobile phase. The mixture of pure hydrogen and air was used for combustion in FID. The temperature of injection port was specified at 290 °C, whereas the temperature profile of the oven was shown in **Figure 2.3**.

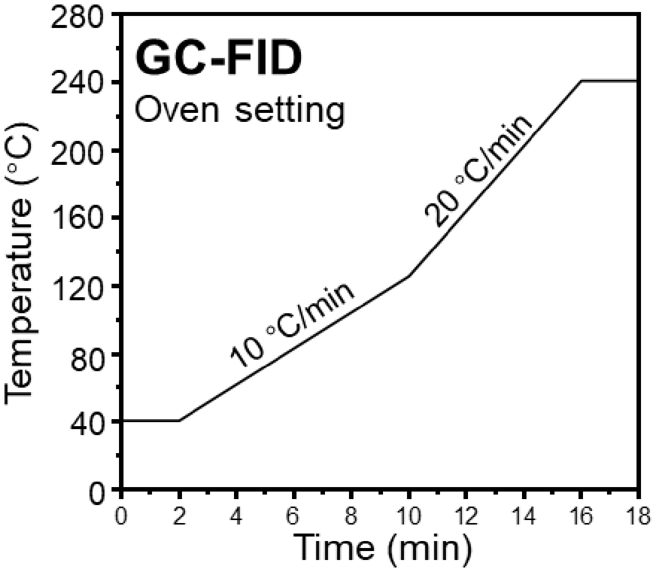

Figure 2.3 Temperature profile of oven in GC-FID.

doi:10.6342/NTU202502278

Figure 2.4 and Table 2.3 summarize the retention times of all the target compounds in this study. **Figure 2.5** demonstrates the calibration curves of each compound, wherein the gradient of the curve is used in determining the concentration of the compound in the solution after reaction (**Equation 2.1**).

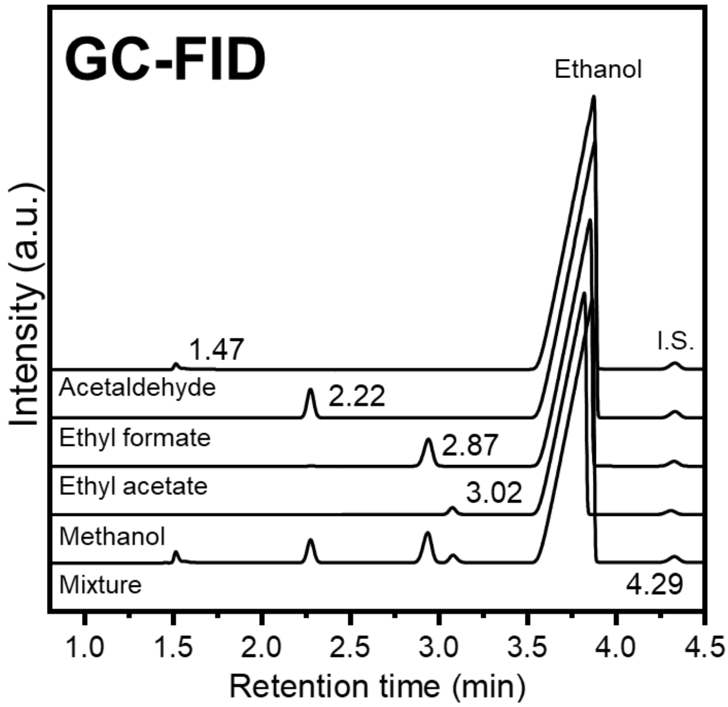

Figure 2.4 Retention times of the target compounds in GC-FID. I.S. refers to internal standard, n-decane.

Table 2.3 Retention times and FID sensitivity of the target compounds in this study.

Compounds	Retention Time in GC-FID (min)	FID Sensitivity
Ethanol	3.76	0.1958
Methanol	3.02	0.0827
Ethyl formate	2.22	0.1612
Acetaldehyde	1.47	0.0616
Ethyl acetate	2.87	0.3329
n-decane	4.25	-

doi:10.6342/NTU202502278

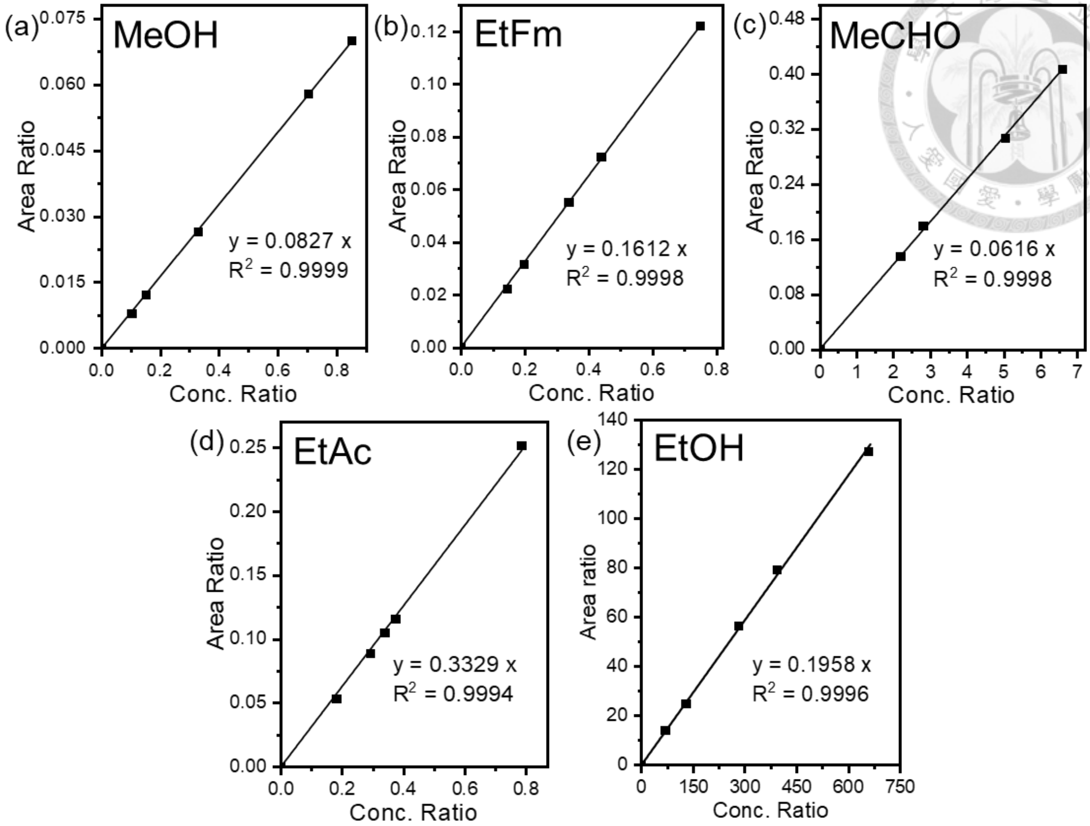

Figure 2.5 Calibration curves of (a) methanol (MeOH), (b) ethyl formate (EtFm), (c) acetaldehyde (MeCHO), (d) ethyl acetate (EtAc), and (e) ethanol (EtOH).

$$Conc_i = \frac{A_i}{A_{IS}} \times \frac{Conc_{IS}}{FID\ sensitivity_i} \qquad \textbf{Equation 2.1}$$

where

$Conc_i$: Concentration of product (mmol)

$Conc_{IS}$: Concentration of internal standard (mmol)

A_i : Detected area of product in GC-FID (a.u.)

A_{IS} : Detected area of internal standard in GC-FID (a.u.)

$FID\ sensitivity_i$: Sensitivity of product in GC-FID, as summarized in **Table 2.3**

2.3.3 Gas Chromatography with Thermal Conductivity Detector (GC-TCD)

The quantitative analysis of gas-phase reaction products was performed using gas chromatography equipped with a thermal conductivity detector (GC-TCD). In GC, the sample is first vaporized at high temperature and then introduced into the analytical column *via* a reference gas. The separation of components is achieved based on differences in retention time, which result from varying interactions between analytes and the stationary phase within the column. The TCD employed in this study operates on the principle of a Wheatstone bridge circuit. The reference gas, free of analytes, flows through one resistor, while the gas containing the sample passes through another. As electric current flows through the resistors, they heat up; however, due to the differing thermal conductivities of the two gas streams, the resistors reach different temperatures, leading to variations in resistance. This creates a potential difference across the Wheatstone bridge, generating an electrical signal proportional to the gas concentration.

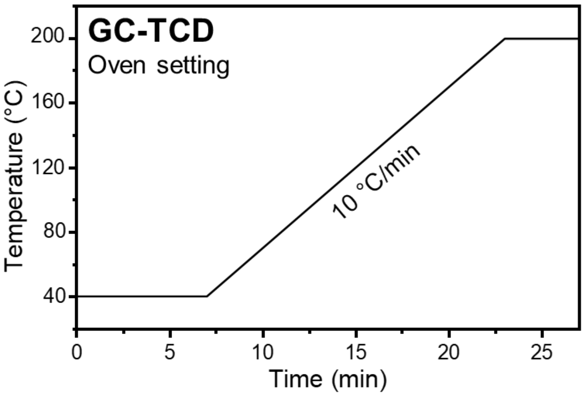

Figure 2.6 Temperature profile of oven in GC-TCD.

The GC-TCD system used in this study was a Shimadzu GC-2014, equipped with a Carboxen-1000 analytical column. High purity argon (99.999% Ar) was used as the reference gas at a flow rate of 50 mL/min. Both the injection port and detector temperatures were maintained at 200 °C. The oven temperature program is presented in **Figure 2.6**. This setup enabled the detection of carbon dioxide (CO_2), hydrogen (H_2), nitrogen (N_2), oxygen (O_2) and carbon monoxide (CO), as illustrated in **Figure 2.7**. Since O_2 is introduced in trace amounts during gas transfer from the reactor to the gas bag, calibration curves were specifically prepared for H_2, N_2, CO, and CO_2, as shown in **Figure 2.8**. The concentration of the product gas was calculated using **Equation 2.2** by assuming the Ideal Gas Law, negligible pressure drop, and ethanol consumption after the reaction.

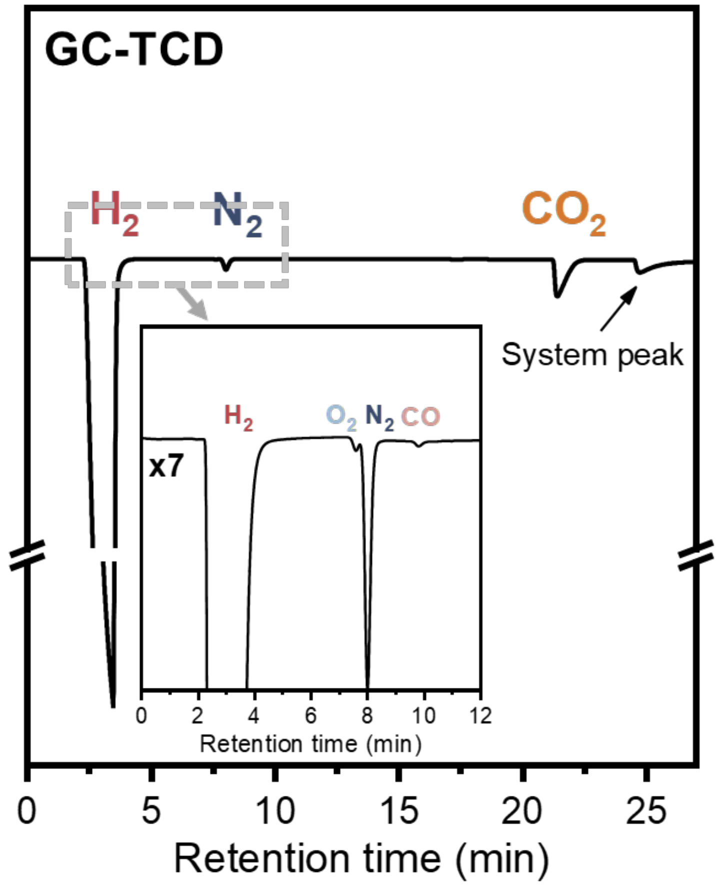

Figure 2.7 GC-TCD chromatogram of gas phase reactants and products.

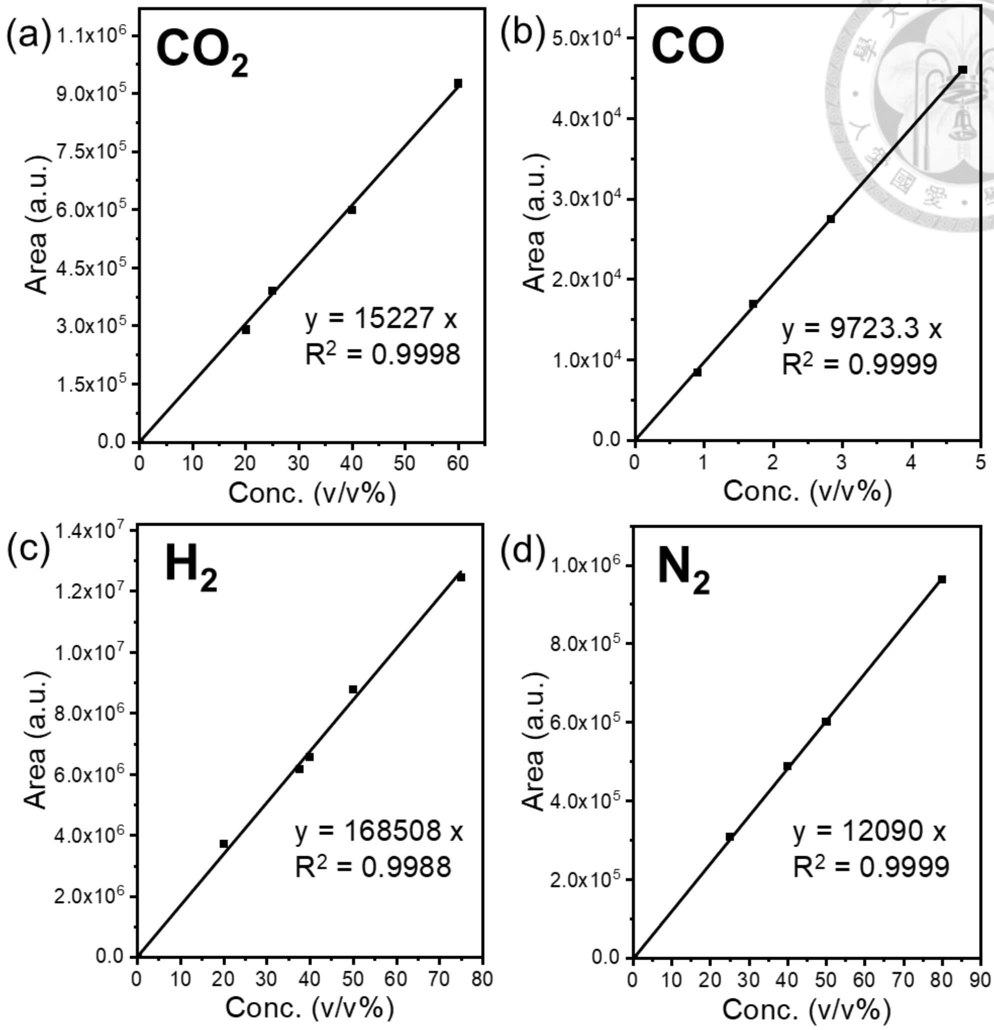

Figure 2.8 Calibration curves of (a) CO_2, (b) CO, (c) H_2 and (d) N_2.

$$Conc_i = \frac{A_i}{TCD\ Sensitivity_i} \times \frac{1}{100\ \%} \times \left(\frac{PV}{RT}\right)_{reactor}$$ **Equation 2.2**

where

$Conc_i$: Concentration of product (mmol)

A_i : Detected area of product in GC-TCD (a.u.)

$TCD\ Sensitivity_i$: Sensitivity of product in TCD, as shown in **Figure 2.8**.

$\left(\frac{PV}{RT}\right)_{reactor}$: Total number of moles of gas in the reactor after reaction and cooled down to room temperature (mmol)

2.4 Catalyst Characterization

2.4.1 X-ray Diffraction (XRD)

X-ray diffraction (XRD) is a technique used to determine the crystalline structure of catalysts by detecting X-rays of a specific wavelength, which are generated when high-speed electrons collide with a metal target. Diffraction occurs when the angle between the incident X-ray and a specific crystal plane of the sample satisfies Bragg's law. The resulting diffraction angles and corresponding intensities are recorded. By comparing the observed 2θ diffraction angles with standard crystallographic reference patterns, the crystal structure and lattice parameters can be identified.

In this study, XRD was utilized to confirm the structure of catalysts synthesized *via* co-precipitation and to compare their crystalline structures before and after reduction. The X-ray diffraction analysis was performed using a Rigaku Ultima IV diffractometer with a copper (Cu) target as the X-ray source (Cu Kα = 1.546 Å). The instrument operated at a voltage of 40 kV and a current of 40 mA. Measurements were conducted in the 2θ range of 20° to 90°, with a scanning speed of 10°/min and a step size of 0.01°.

doi:10.6342/NTU202502278

2.4.2 Inductively Coupled Plasma Optical Emission Spectroscopy (ICP-OES)

Inductive coupled plasma optical emission spectroscopy (ICP-OES) is used to quantify metal loading by measuring the concentration of each metal species present in a catalyst. The principle of ICP-OES involves introducing the sample solution into the system *via* a peristaltic pump, where it is nebulized into an aerosol before entering the inductively coupled plasma. Within the high-energy plasma, the aerosolized sample undergoes vaporization and ionization. The excited ions, in an unstable state, return to their ground state, emitting characteristic wavelengths of light. The intensity of this emission correlates with the ion concentration, allowing for precise quantification through electronic multipliers or solid-state semiconductor detectors. In this study, ICP-OES was employed to measure the loading of Cu and Zn metal in catalyst samples using a Thermo Fisher Scientific iCAP PRO instrument.

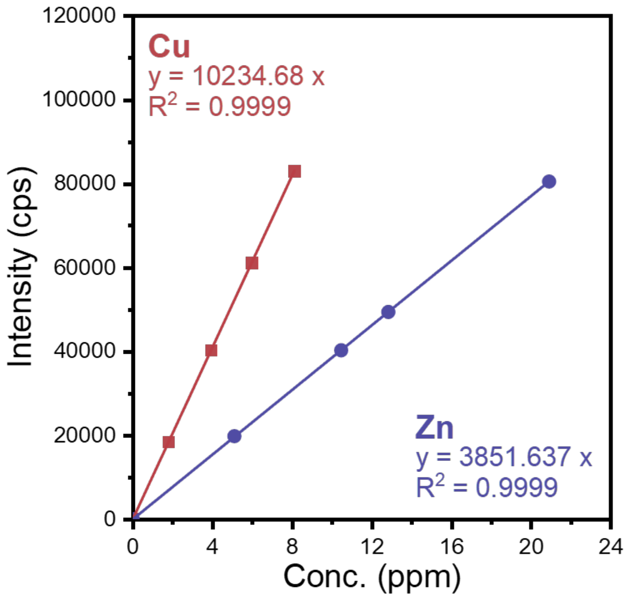

Figure 2.9 Calibration curves of Cu and Zn concentration in ICP-OES.

- Preparation of Calibration Curves

The purchased copper (Fisher Scientific, 10000 ppm Cu in 1 M HNO_3) and zinc (Fisher Scientific 10000 ppm in 1 M HNO_3) standard solutions were diluted with 3 wt.% nitric acid solution to prepare calibration solutions of varying concentration, each with a total volume of 20 mL. These calibration solutions, which can contain both metal ions simultaneously, were used to establish the calibration curves correlating the concentration of Cu and Zn with their respective absorbance values, as shown in **Figure 2.9**.

- Preparation of Sample Solution

10 mg of the catalyst sample was weighed using a microbalance and placed in a 20 mL polypropylene (PP) bottle. Then, 10 mL of aqua regia (HNO_3:HCl = 1:3 v/v) was added, and the mixture was left to stand overnight to dissolve the catalysts. 200 μL of the resulting solution was taken and diluted to a final volume of 20 mL with 3 wt.% nitric acid solution to ensure that the metal concentration fell within the calibration curve range.

2.4.3 Accelerated Surface Area and Porosimetry (ASAP)

In this study, the specific surface area of the catalysts was determined using an Accelerated Surface Area and Porosimetry System (ASAP) through the isothermal adsorption-desorption method. At a constant temperature, gases such as N_2, Ar or Kr were used to evaluate the effect of partial pressure (P/P_0) on gas adsorption, generating an adsorption-desorption curve. By applying different calculation models, for instance, Brunauer-Emmett-Teller (BET), Langmuir, and Barrett-Joyner-Halenda (BJH), the specific surface area and pore size distribution of the samples were determined.

The specific surface area analysis was conducted using a Micromeritics ASAP 2010 instrument. To ensure measurement accuracy, the total surface area of the sample was required to be at least 4 m^2. Accordingly, approximately 0.2 g of the catalyst was placed into the sample tube, followed by the insertion of a filling rod. The sample tube was then leaded onto the degas port for overnight pretreatment at 100 °C and 4 μmHg to remove moisture and impurities.

After pretreatment, the sample tube was covered with an isothermal jacker and transferred to the analysis port. During measurement, the sample tube was immersed in a Dewar flask containing liquid nitrogen to maintain the analysis at the boiling point of liquid nitrogen (77 K). Using the BET model, as represented in **Equation 2.3**, the specific surface area of the catalyst sample was determined.

$$\frac{P}{V(P_0-P)}=\frac{1}{V_mC}+\frac{(C-1)P}{V_mCP_0} \qquad \textbf{Equation 2.3}$$

P	:	Equilibrium pressure at 77 K	P_0	:	Saturation pressure at 77 K
V	:	Volume of adsorbed gas	V_m	:	Volume of monolayer adsorbed gas
C	:	BET constant			

doi:10.6342/NTU202502278

2.4.4 Transmission Electron Microscopy (TEM)

Transmission electron microscopy (TEM) is a powerful analytical technique that utilizes a high-energy electron beam to probe the internal structure of materials. In TEM, the focused electron beam interacts with the sample, generating transmitted and scattered electrons due to variations in sample thickness and composition. The transmitted electron signal produces contrast in the resulting image, and diffraction patterns enable the analysis of crystal structures. Additionally, TEM can be equipped with energy-dispersive X-ray spectroscopy (EDS) to investigate elemental composition and distribution. EDS operates by detecting characteristic X-rays emitted when high-energy electrons excite inner-shell electrons, leading to electron transitions that release energy as X-ray emission, which is element-specific.

In this study, a field-emission TEM (FE-TEM, JEOL JEM-2100F) operated at 200 kV was employed to examine the crystalline morphology and exposed crystal facets of the catalyst. Elemental analysis was conducted using an Oxford X-MaxN TSR EDS detector.

Sample preparation:

1. 1 mg of catalyst sample was dispersed in 20 mL of EtOH, followed by ultrasonication for 1 hour to ensure a uniform suspension.
2. 20 μL of the suspension was then drop-cast onto a 200-mesh carbon-coated nickel grid and dried in a vacuum oven at 100 °C overnight to ensure complete removal of the remaining solvent.

doi:10.6342/NTU202502278

2.4.5 Hydrogen Temperature Programmed Reduction (H_2-TPR)

During the ramping program, a continuous flow of 10% H_2/Ar was introduced into the tube containing the catalyst sample. The variations in gas concentration within the designated temperature range were detected by a thermal conductivity detector (TCD) to assess the reducibility of the metal oxide in the catalyst. **Equation 2.4** represents the reduction reaction of copper oxide (CuO) to metallic copper (Cu) using hydrogen (H_2) as the reducing agent.

$$CuO + H_2 \rightarrow Cu^0 + H_2O \qquad \textbf{Equation 2.4}$$

Detailed procedures:

1. Pretrement:

- 50 mg of the calcined catalyst was heated in a rate of 10 °C/min to 300 °C for 10 minutes under an Ar flow of 50 mL/min to remove the moisture and impurities.

2. Cooling:

- The sample was cooled down to 50 °C while maintaining the Ar flow.

3. Stabilization of TCD signal:

- A 50 mL/min of 10% H_2/Ar was introduced, and the TCD signal was allowed to stabilize for 30 minutes.

4. H_2-TPR:

- The sample was heated to 300 °C at a rate of 5 °C/min under a 50 mL/min flow of 10% H_2/Ar.

2.4.6 Carbon Dioxide and Ammonia Temperature Programmed Desorption (CO_2-TPD & NH_3-TPD)

Temperature-programmed desorption (TPD) is a technique used to characterize the interaction between a probe gas and the surface of a catalyst. Additionally, depending on the acidic and basic nature of the probe gas, TPD results can be used to evaluate the acidity and basicity of the catalyst sample.

In the experiment, the probe gas was continuously flowed through the tube containing the catalyst sample at a constant temperature for a specific duration to allow complete adsorption. Subsequently, an inert gas was introduced to remove any physisorbed gas. The catalyst was then heated at a constant ramping rate, as specified by the program, under an inert gas flow. As the temperature increased, the adsorbed gas desorbed accordingly. The desorption temperature and the amount of desorbed gas were recorded to analyze the surface properties of the catalyst sample.

Detailed procedures:

1. Pretrement:

- 50 mg of the calcined catalyst was heated at a rate of 10 °C/min to 300 °C for 10 minutes under an Ar flow of 50 mL/min to remove the moisture and impurities.
- The sample was then cooled down to 300 °C, and a 50 mL/min flow of 10% H_2/Ar was introduced for 30 minutes to ensure that the copper in the catalyst was in its metallic state during measurement.
- The sample was subsequently cooled down to 50 °C under a 50 mL/min Ar flow.

doi:10.6342/NTU202502278

2. Probe gas feeding:

- A 50 mL/min flow of CO_2 (or 1% NH_3/Ar) was introduced for 30 minutes to achieve full adsorption.
- This was followed by an Ar purge for 30 minutes to remove any remaining and physisorbed gas.

3. Stabilization of TCD signal:

- The TCD signal was allowed to stabilize for 30 minutes under an Ar flow of 50 mL/min.

4. Temperature programmed desorption (TPD):

- The sample was heated at a rate of 5 °C/min to 600 °C under a 50 mL/min Ar flow.

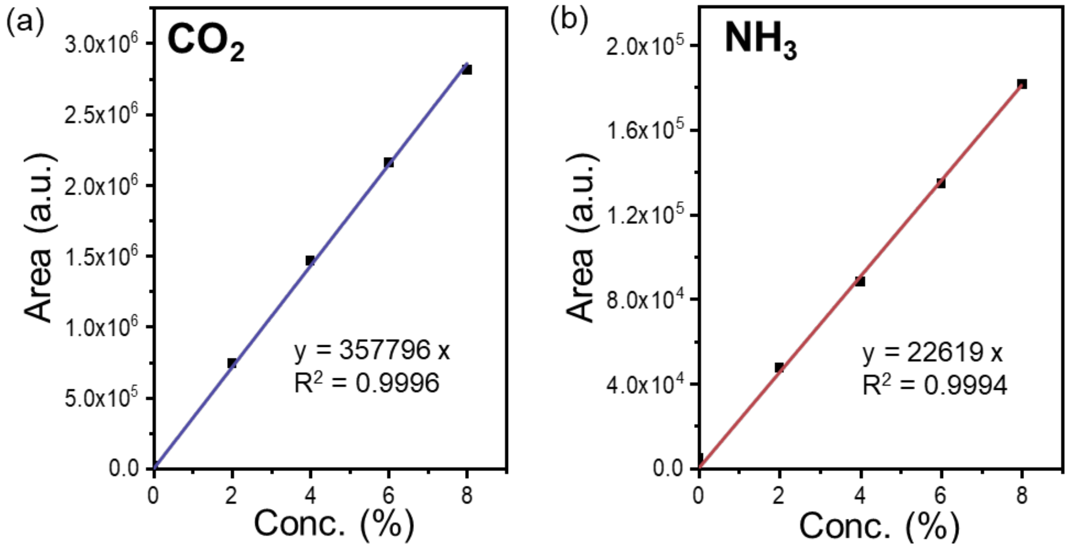

Figure 2.10 Calibration curves of (a) CO_2 and (b) NH_3 for TPD experiments.

2.4.7 N_2O Titration

To accurately quantify the oxygen vacancies in ceria-containing catalysts, the combined N_2O titration method developed by E. J. M. Hensen *et al.* was employed.[45] Characterizing CeO_2-containing catalysts using only N_2O as the probe molecule presents challenges, as N_2O interacts with both copper and the oxygen vacancies of CeO_2. In the N_2O titration method, CO_2 serves as a blocking agent, selectively occupying oxygen vacancies in CeO_2-supported catalysts, thereby improving measurement accuracy. **Figure 2.11.** shows the sequence of this method to quantify the oxygen vacancies of the sample.

By assuming that N_2O interacts with oxygen vacancies in a ratio of 1:1 (N_2O:O_v), N_2O oxidizes exposed surface Cu into Cu_2O (**Equation 2.5**), the surface oxygen vacancies can be estimated using **Equation 2.6**. Additionally, Cu dispersion can be estimated using **Equation 2.7** with the assumption where ratio of N_2O to Cu is 1:2.

$$2Cu + N_2O \rightarrow Cu_2O + N_2 \qquad \textbf{Equation 2.5}$$

$$N_{Ov}=\frac{N_{N2O,1}-N_{N2O,2}}{m_{cat}} \qquad \textbf{Equation 2.6}$$

$$D_{Cu}: \frac{2\times N_{N2O,2}\times M_{Cu}}{W_{Cu}}\times 100\% \qquad \textbf{Equation 2.7}$$

where

N_{Ov} : Number of oxygen vacancies (mol/g-cat)

m_{cat} : Mass of catalyst (g)

$N_{N2O,1}$: Amount of consumed N_2O in the 1st pulsing (mol)

$N_{N2O,2}$: Amount of consumed N_2O in the 2nd pulsing (mol)

M_{Cu} : Molar mass of Cu (63.546 g/mol)

W_{Cu} : Cu loading in the catalysts measured by ICP-OES (g-Cu)

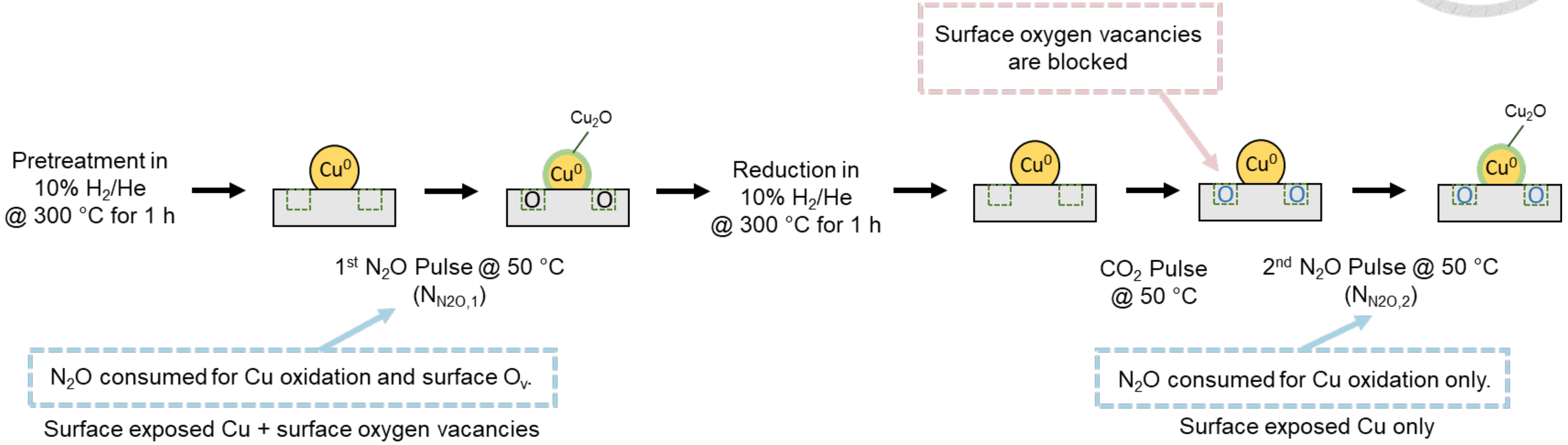

Figure 2.11 N$_2$O titration method for measurement of surface oxygen vacancies and Cu dispersion.

doi:10.6342/NTU202502278

Detailed procedure

1. First Pretreatment

- 50 mg of the calcined catalyst was heated at a rate of 10 °C/min to 300 °C for 10 minutes under an Ar flow of 50 mL/min to remove the moisture and impurities.
- The sample was then reduced in 10% H_2/He flow (50 mL/min) for 1 hour.
- After reduction, the sample was cooled to 50 °C under a 50 mL/min Ar flow.

2. First N_2O pulsing

- 2% N_2O/He was periodically injected using a sample loop (pulse injection) for 20 pulses to ensure complete saturation.
- The N_2O consumptions was recorded as $N_{N2O,1}$.

3. Second Pretreatment

- The sample was reheated to 300 °C at a rate of 10 °C/min and treated again under a 10% H_2/He flow (50 mL/min) for 1 hour.
- The sample was then cooled to 50 °C under a 50 mL/min Ar flow.

4. CO_2 feeding

- 20 pulses of pure CO_2 were injected at 50 °C to selectively block the oxygen vacancies of the sample.

5. 2^{nd} N_2O pulsing

- 2% N_2O/He was periodically injected using a sample loop (pulse injection) for 20 pulses to ensure complete saturation.
- The N_2O consumption in this step was denoted as $N_{N2O,2}$.

doi:10.6342/NTU202502278

2.4.8 Infrared Spectroscopy (IR)

Fourier transform infrared spectroscopy (FTIR) is a widely used analytical technique for characterizing molecular structures based on infrared (IR) absorption. When molecules absorb IR radiation, specific chemical bonds undergo vibrational and rotational transitions, leading to characteristic absorption bands that provide insights into functional groups and molecular composition. FTIR operates using a Michelson interferometer, which splits the IR light source into two beams – one reflected by a fixed mirror and the other by a moving mirror. The movement of the mirror creates an optical path difference, resulting in constructive and destructive interference patterns. These interference signals are processed through Fourier transformation to generate an infrared absorption spectrum.

In this study, FTIR was employed to investigate the *in-situ* surface reactions of EtOH and other solvents. A Nicolet iS50 FTIR spectrometer, as shown in **Figure 2.12**, equipped with a Mercury-Cadmium-Telluride (MCT) detector was used, and data acquisition was performed in diffuse reflectance mode (DRIFTS). Spectra were collected with 64 scans at a resolution of 4 cm^{-1}, using a ZnSe window as the background reference.

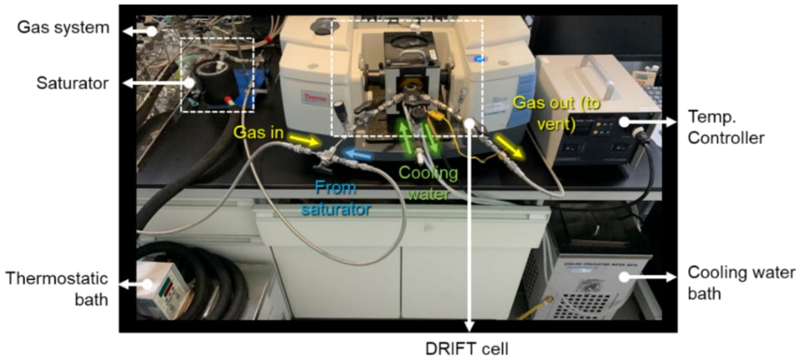

Figure 2.12 Setup of diffuse reflectance infrared Fourier transform spectroscopy (DRIFTS).

Detailed procedure

(A) To observed adsorbed species, without *in-situ* reaction

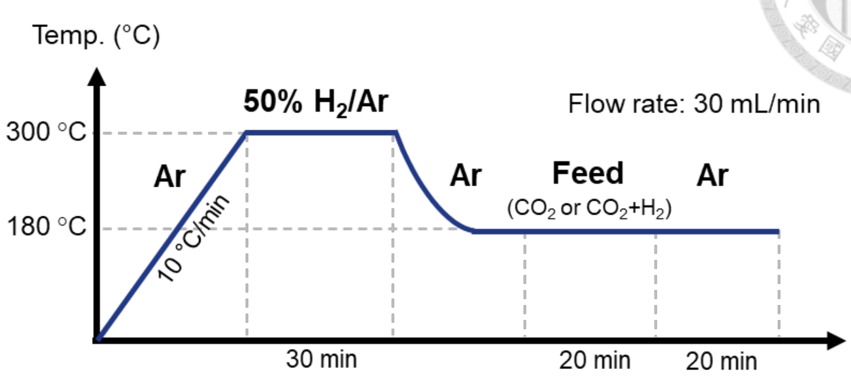

(B) *In-situ* reaction of adsorbed species with external solvent

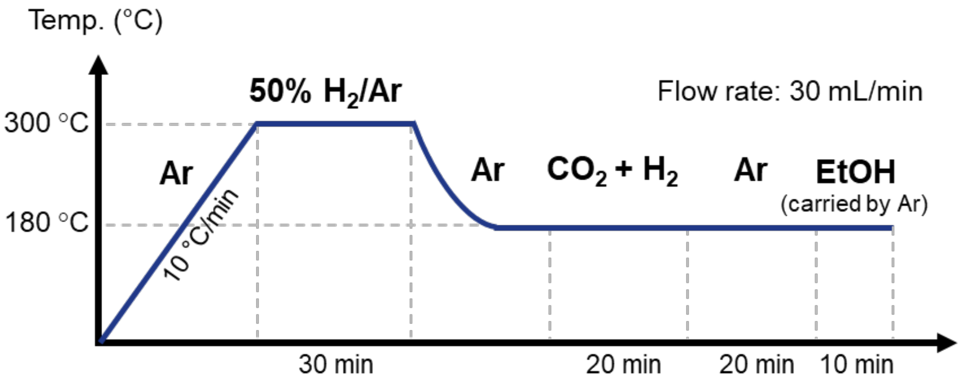

(C) Transformation of adsorbed species with increasing temperature

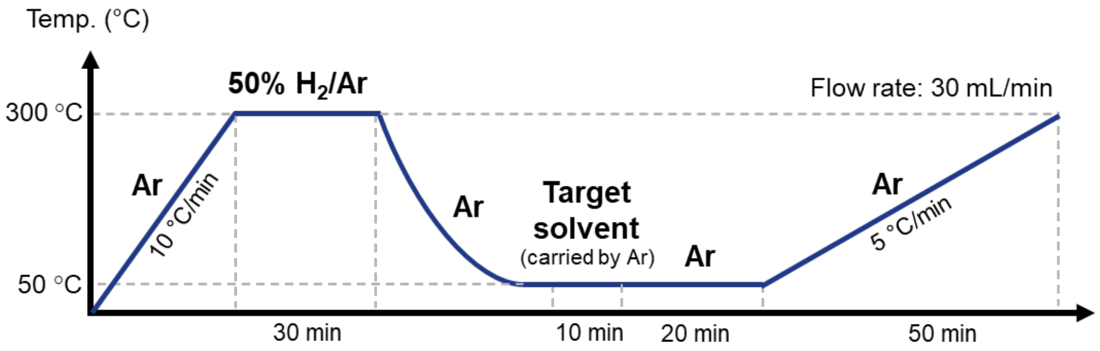

CHAPTER 3 RESULTS AND DISCUSSION

3.1 Catalyst Characterization

3.1.1 H_2-Temperature Programmed Reduction (H_2-TPR)

In this study, the reduction behavior of the catalysts was investigated by H_2-TPR to establish the appropriate reduction condition. **Figure 3.1** shows that complete reduction of Cu species occurred below 300 °C for all samples.

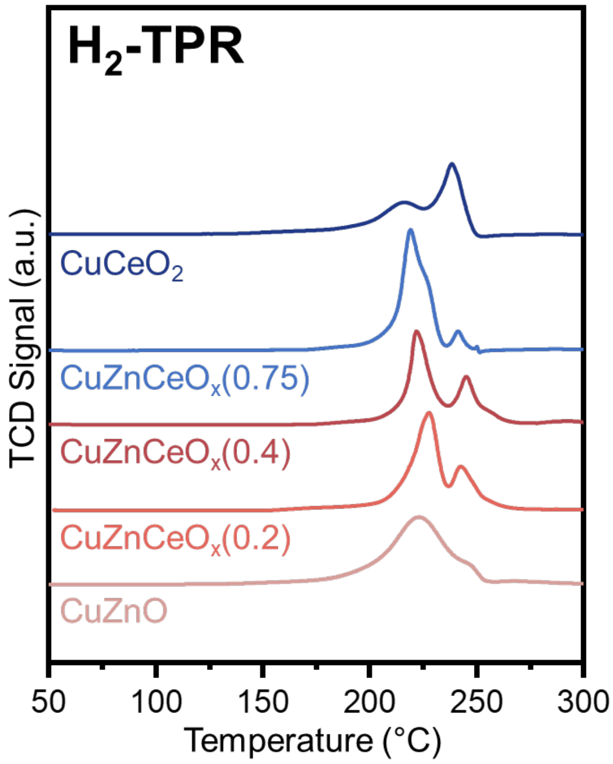

Figure 3.1 H_2-TPR profile of catalysts.

The CuZnO catalyst displays a broad, asymmetric reduction peak centered around 230 °C, characteristic of CuO_x species moderately interacting with the ZnO matrix. Upon incorporation of CeO_2, as in CuZnCeO$_x$(0.2), the reduction peak shifts slightly to higher

doi:10.6342/NTU202502278

temperatures, indicative of enhanced Cu dispersion and stronger metal-support interactions with CeO_2. This behavior is attributed to the formation of highly dispersed Cu species with stronger Cu-Ce interactions, which require elevated temperatures for reduction. Interestingly, with further increases in CeO_2 content, as in $CuZnCeO_x(0.4)$ and $CuZnCeO_x(0.75)$, the reduction peaks become progressively narrower and shift toward lower temperatures. This trend reflects the dual function of ceria: it strengthens Cu dispersion and metal-support interactions, while its intrinsic redox properties, particularly the Ce^{3+}/Ce^{4+} cycle, facilitate the reduction of CuO_x species. The narrowing of the peaks suggests a more readily reduction, which is completed within a smaller thermal window.

In contrast, the reduction profile of the $CuCeO_2$ differs significantly from that of the Ce-modified $CuZnCeO_x$ series, showing distinct peak shapes and a shift of the main reduction peak toward higher temperatures. This change in reduction behavior is likely attributed to the formation of Cu-O_v-Ce solid solutions [45,46] or the embedding of CuO_x within the ceria matrix, both of which typically require higher activation temperatures due to stronger confinement within the ceria lattice.

Table 3.1 H_2 consumption of catalysts in H_2-TPR.

Catalyst	Cu (mmol/50 mg)	H_2 consumed (mmol)	H_2/Cu ratio
CuZnO	0.3383	0.3386	1.00
$CuZnCeO_x(0.2)$	0.2990	0.2992	1.00
$CuZnCeO_x(0.4)$	0.2675	0.2690	1.01
$CuZnCeO_x(0.75)$	0.2360	0.2801	1.19
$CuCeO_2$	0.1967	0.2634	1.34

doi:10.6342/NTU202502278

Table 3.1 showed the ratio of H_2 consumed during TPR to the theoretical H_2 consumption based on Cu content in the catalysts sample (H_2/Cu). When Ce was absent or at low levels, the H_2/Cu ratio approached unity, indicating that hydrogen consumption was primarily due to CuO_x reduction. With increased Ce content, the H_2/Cu ration exceeded unity, consistent with additional hydrogen uptake from partial CeO_2 reduction *via* hydrogen spillover from metallic Cu.[47,48] Notably, pure CeO_2 exhibited no reduction below 300 °C in the absence of Cu (**Appendix 1**), highlighting the critical role of Cu in enabling low-temperature CeO_2 reduction.

doi:10.6342/NTU202502278

3.1.2 X-ray Diffraction (XRD)

As outlined in Section 2.2, the catalysts in this study were synthesized *via* the co-precipitation method. Following calcination, catalysts containing CuO species were obtained, as shown in **Figure 3.2 (a).** Subsequent reduction at 300 °C resulted in the complete transformation of CuO into metallic Cu, as illustrated in **Figure 3.2 (b),** confirming that the reduction temperature determined by H_2-TPR was suitable for achieving full reduction of the copper species.

In comparison to the sharp diffraction peaks observed for CuZnO, $CuCeO_2$ catalyst exhibited no discernible CeO_2 diffraction peaks, indicating that it predominantly existed in an amorphous state. Moreover, the overall intensity of crystalline phases decreased with increasing Ce content across the catalyst series. This trend suggests that the incorporation of Ce promotes structural amorphization, in agreement with findings reported in the literature.[47]

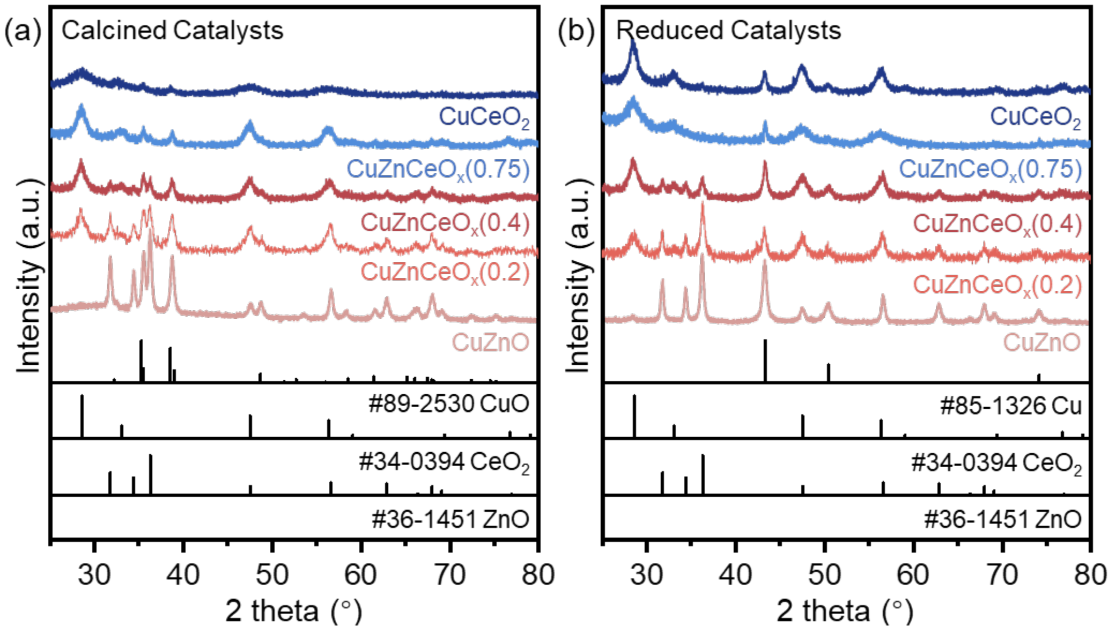

Figure 3.2 XRD patterns of (a) calcined catalysts and (b) reduced catalysts.

3.1.3 Physicochemical Properties

The molar ratio of Cu to the total support metals (Zn and Ce) was maintained at 0.5 during synthesis. However, due to the higher atomic mass of Ce relative to Zn, the overall Cu loading decreased with increasing Ce content. Since Ce cannot be dissolved in aqua regia, after the composition of Cu and Zn was confirmed in ICP-OES, the Ce content was then determined using SEM-EDAX. **Table 3.2** shows the theoretical and actual composition of catalysts as-prepared.

Table 3.2 Theoretical and actual composition of catalysts.

Catalysts	Cu loading (wt.%)[a]		Zn loading (wt.%)[a]		Cu : Zn : Ce[b]	
	Theoretical	Actual	Theoretical	Actual	Theoretical	Actual
CuZnO	43.8	43	45.1	46	1 : 1 : 0	1 : 1.1 :0
$CuZnCeO_x$(0.2)	38.9	38	32.1	34	5 : 4 : 1	5 : 3.8 : 1.1
$CuZnCeO_x$(0.4)	35.1	34	21.6	22	5 : 3 : 2	5 : 2.9 : 2.2
$CuZnCeO_x$(0.75)	29.8	30	7.7	7	4 : 1 : 3	4 : 1.1 : 2.9
$CuCeO_2$	26.9	25	0	0	1 : 1 : 0	1 : 0 : 1.1

[a] Measured by ICP-OES
[b] Measured by SEM-EDAX

Table 3.3 summarizes the physicochemical properties of catalysts, including the specific surface area determined by N_2 isothermal adsorption. The morphologies of the reduced catalysts were observed by SEM (**Figure 3.3**) and TEM (**Figure 3.4**). CuZnO catalyst exhibits large, aggregated nanoparticles with irregular surfaces, and an average particle size of approximately 37.4 nm, which is significantly larger than that of the Ce-containing counterparts. Upon Ce incorporation, a substantial reduction in particle size is observed, which is consistent with previous reports indicating that CeO_2 inhibits particle growth during synthesis and calcination.[42] $CuZnCeO_x$(0.2) shows the smallest average particle size (*ca.* 7.52 nm), along with increased surface roughness, features that are expected to contribute to higher species surface area. With further increase in Ce content, as in $CuZnCeO_x$(0.4) and $CuZnCeO_x$(0.75), the particles appear increasingly fragmented and less defined, consistent with partial structural collapse and the formation of disorders, amorphous-like domains inferred from XRD results. In $CuCeO_2$, the fragmented particles tend to agglomerate into dense clusters, resulting in an increase in average particle size to approximately 21.7 nm.

Further insights into copper dispersion were obtained from TEM elemental mapping (**Figure 3.5)**. The results revealed that all metals were generally well-dispersed across the catalyst matrices. While some localized agglomeration of copper was observed in CuZnO, $CuZnCeO_x$(0.4) and $CuZnCeO_x$(0.75), a more uniform and finely dispersed Cu distribution was evident in $CuZnCeO_x$(0.2) and $CuCeO_2$.

Table 3.3 Physicochemical properties of as-prepared catalysts

Catalysts	Cu loading (wt.%)[a]	S_A (m^2/g)[b]	Average particle size (nm)[c]	Total basicity (mmol CO_2/g-cat.)[d]	Total acidity (mmol NH_3/g-cat.)[e]
CuZnO	43	12.4	37.4	0.54	0.20
$CuZnCeO_x$(0.2)	38	25.2	7.52	1.05	0.31
$CuZnCeO_x$(0.4)	34	23.8	7.62	1.08	0.30
$CuZnCeO_x$(0.75)	30	23.6	7.99	1.87	0.32
$CuCeO_2$	25	19.5	21.7	2.28	0.35

[α] Measured by ICP-OES

[b] Measured by N_2 isothermal adsorption with BET method

[c] Measured by TEM

[d] Measured by CO_2-TPD

[e] Measured by NH_3-TPD

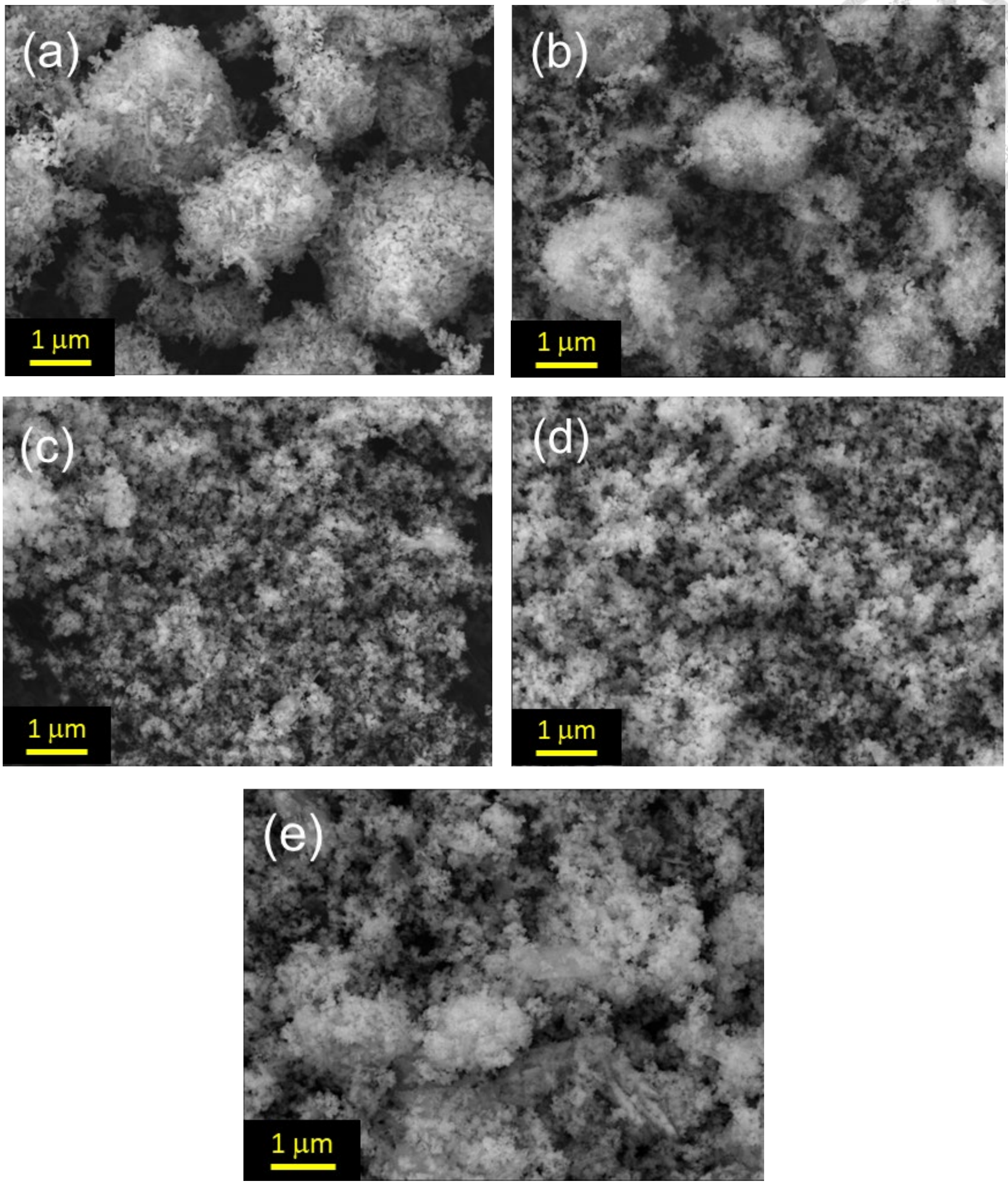

Figure 3.3 SEM images and the particle size distribution of (a) CuZnO, (b) CuZnCeO$_x$(0.2), (c) CuZnCeO$_x$(0.4), (d) CuZnCeO$_x$(0.75) and (e) CuCeO$_2$.

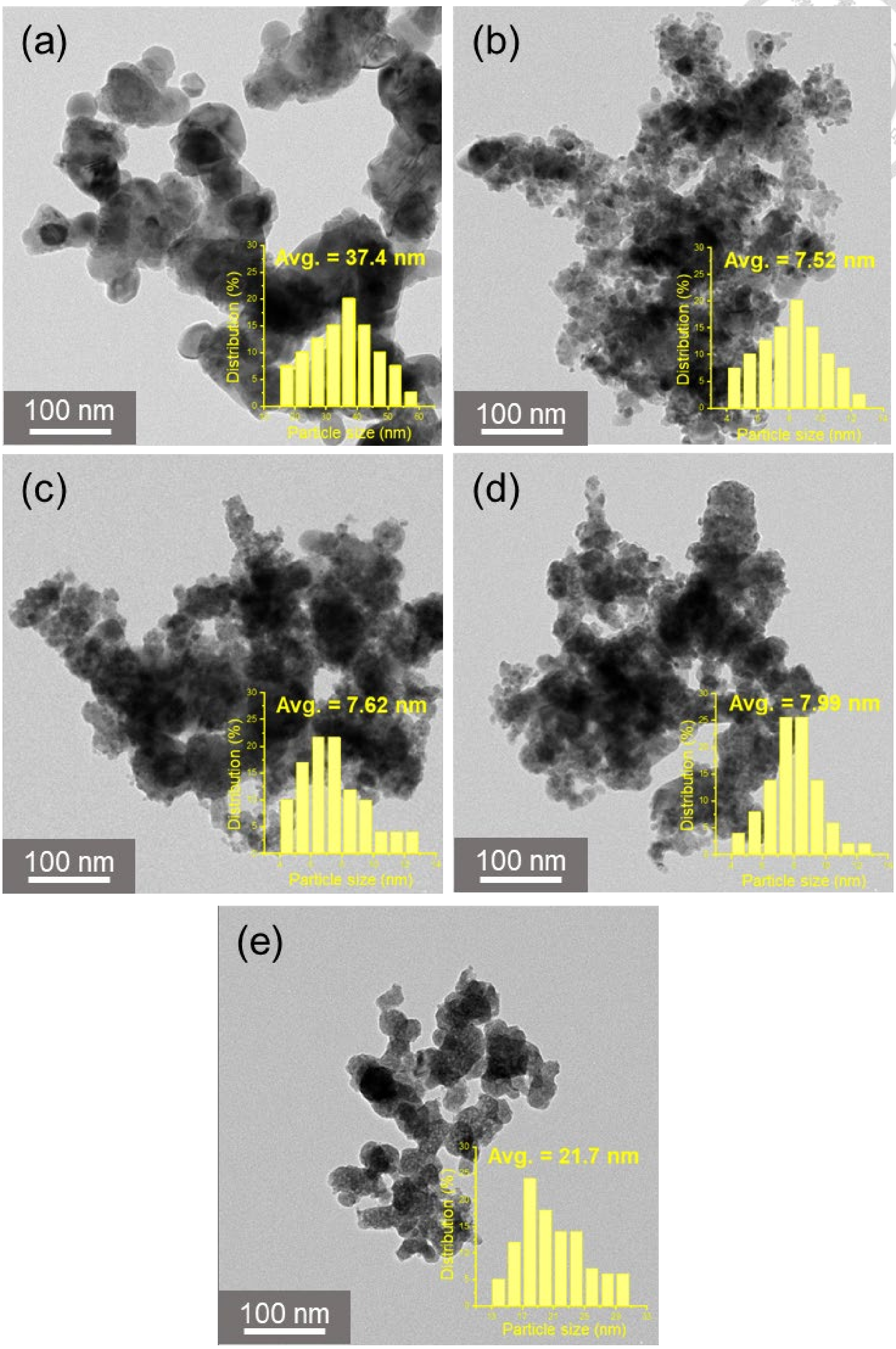

Figure 3.4 TEM images and the particle size distribution of (a) CuZnO, (b) CuZnCeO$_x$(0.2), (c) CuZnCeO$_x$(0.4), (d) CuZnCeO$_x$(0.75) and (e) CuCeO$_2$.

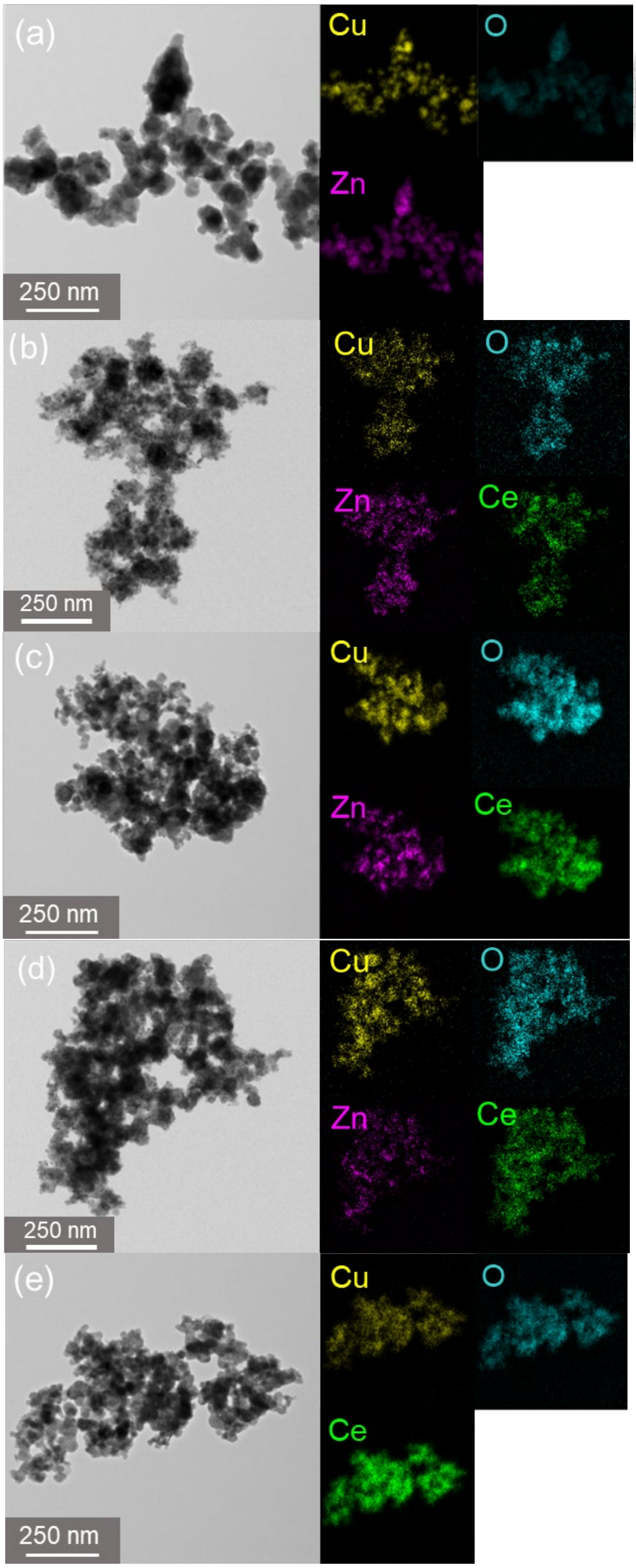

Figure 3.5 TEM images with elemental mapping of (a) CuZnO, (b) $CuZnCeO_x(0.2)$, (c) $CuZnCeO_x(0.4)$, (d) $CuZnCeO_x(0.75)$ and (e) $CuCeO_2$.

In addition to the structural and compositional characteristics, the surface properties of the catalysts, particularly their CO_2 adsorption behavior, play a critical role in catalytic performance. The interaction at the metal-support interface governs not only the adsorption of gas-phase reactants but also the reactivity of surface elementary steps. Metal oxides, commonly employed as supports or promoters, rely on their intrinsic basicity and reducibility to facilitate CO_2 adsorption and activation during catalytic reactions.[49]

Figure 3.6 illustrates the potential CO_2 adsorption sites on CuZnO and $CuCeO_2$. For CuZnO, CO_2 interacts primarily with surface hydroxyl groups and lattice O^{2-} species, forming bicarbonate [50] and various carbonate species, including monodentate and bidentate forms.[51] In contrast, $CuCeO_2$ features not only surface hydroxyl groups and O^{2-} sites but also a high concentration of surface oxygen vacancies, which further enhance CO_2 adsorption and activation, promoting the formation of carbonate species.[52] The nature of the adsorbed CO_2 will be further discussed in detail using infrared spectroscopy in a later section.

The strong CO_2 adsorption capability of CeO_2 was clearly reflected in the CO_2-TPD results (**Figure 3.7 (a)**). As summarized in **Table 3.3**, an increase in Ce content resulted in a substantial enhancement of CO_2 adsorption capacity across the catalyst series.

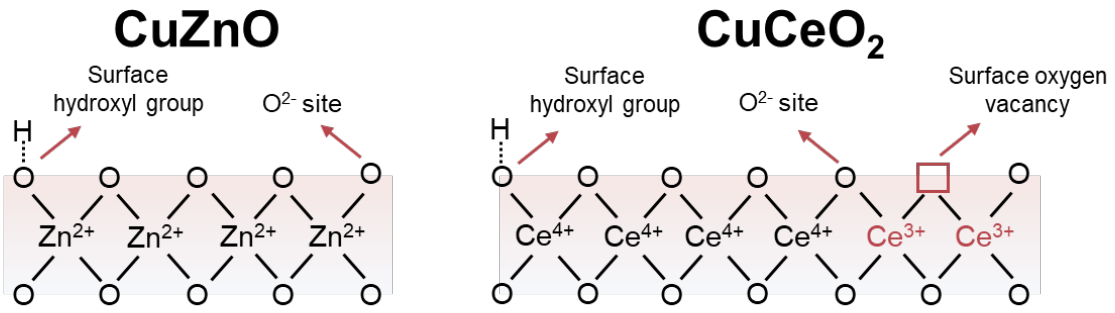

Figure 3.6 Adsorption sites of CO_2 on CuZnO and $CuCeO_2$.

doi:10.6342/NTU202502278

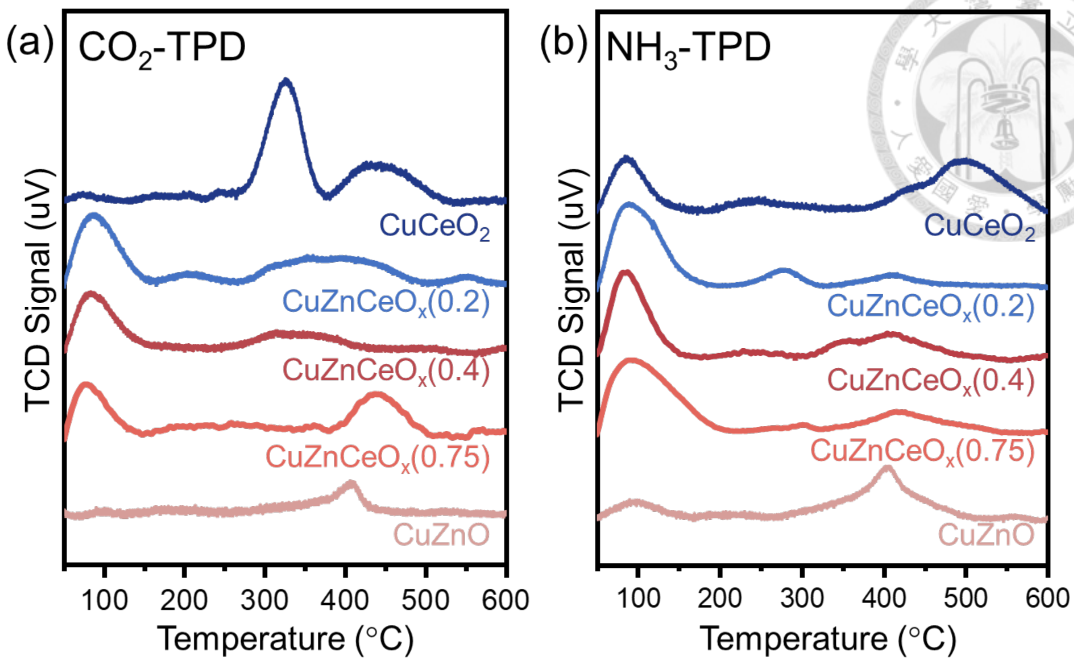

Figure 3.7 (a) CO_2- and (b) NH_3-TPD profiles of catalysts.

The surface acidity of the catalysts also plays an essential role in CO_2 hydrogenation. Lewis acid sites are known to stabilize key intermediates, such as formate species, thereby facilitating MeOH formation.[53] In alcohol-assisted CO_2 hydrogenation systems, a positive correlation between catalyst acidity and MeOH yield has been reported.[24]

Figure 3.7 (b) presents the NH_3-TPD profiles of the catalysts, and the quantified acidity values were summarized in **Table 3.3**. A notable increase in acidity was observed upon the initial incorporation of Ce. However, further increase in Ce content did not significantly alter the overall acidity. The slight shift of the NH_3 desorption peak to higher temperatures with increasing Ce loading suggests a change in acid site strength rather than quantity. This behavior can be attributed to the replacement of Zn^{2+} (a weaker Lewis acid) by Ce^{4+} (a stronger Lewis acid). Although the introduction of Ce created stronger acid sites, the simultaneous reduction in Zn-associated acid sites partially offset this gain, resulting in an overall unchanged NH_3 uptake.

doi:10.6342/NTU202502278

3.1.4 Surface Oxygen Vacancies and Cu Dispersion

In additional to acidity and basicity, the presence of surface oxygen vacancies has been reported as one of the critical factors influencing CO_2 activation. To quantitatively assess the surface oxygen vacancies (Ov) in Ce-containing catalysts, N_2O titration was performed following the method established by Hensen and co-workers.[45,54] Given that CO_2 selectively adsorbs onto surface oxygen vacancies in ceria-based catalysts,[55] CO_2 was used as a probe molecule to pre-occupy these sites prior to N_2O exposure. By comparing the N_2O uptake between two sequential pulse experiments, with and without prior CO_2 treatment, the amount of accessible Ov and Cu dispersion were quantitatively determined (**Table 3.4**).

Table 3.4 Surface oxygen vacancies and Cu dispersion of catalysts determined using N_2O titration method.

Catalysts	Surface oxygen vacancies (μmol N_2O/g-cat.)^f	Cu Dispersion (%)^f
CuZnO	13	9.5
$CuZnCeO_x$(0.2)	106	20.9
$CuZnCeO_x$(0.4)	276	32.4
$CuZnCeO_x$(0.75)	475	7.3
$CuCeO_2$	1300	5.9

^{f} Measured by N_2O titration method.

The experimental results are shown in **Figure 3.8**, where the remaining N_2O concentration in each pulse is plotted. The plateau region, where the pulse height stabilizes, signifies the point at which N_2O is no longer consumed by the catalyst. For the CuZnO sample, no significant difference in N_2O uptake was observed between the two

doi:10.6342/NTU202502278

pulses, indicating the absence of Ov that could be blocked by CO_2. In contrast, Ce-containing catalysts exhibited a clear decrease in N_2O uptake after CO_2 pre-treatment, suggesting that surface oxygen vacancies were effectively blocked by CO_2. As a results, the subsequent N_2O consumption was primarily attributed to the oxidation of metallic Cu species.

The trend in Cu dispersion is highly correlated with the specific surface area and particle size of the catalysts. When the particle size decreased upon incorporation of Ce, as in $CuZnCeO_x$(0.2), the Cu dispersion enhanced significantly. While the co-promoted catalysts exhibited similar Cu dispersion, the drop in Cu dispersion in $CuCeO_2$ is attributed to the collapse of structure as observed in SEM image (**Figure 3.3 (e)**).

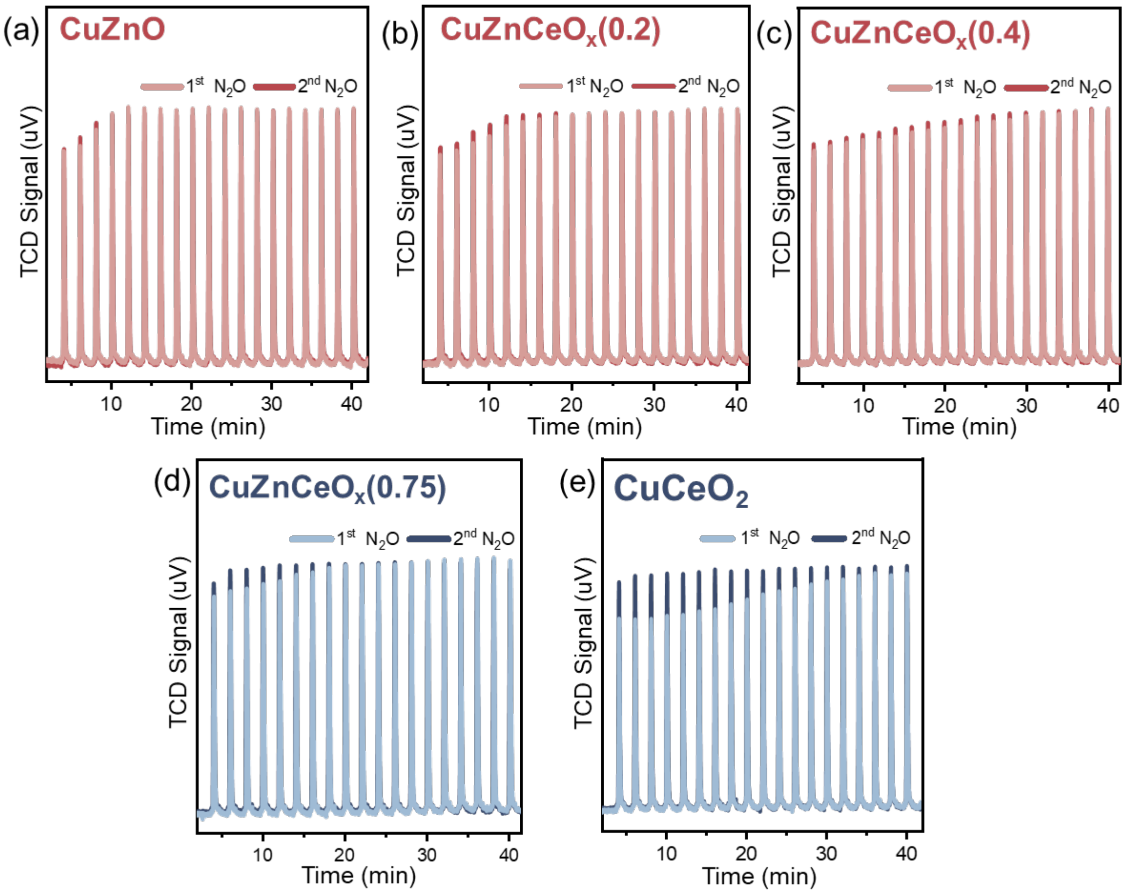

Figure 3.8 N_2O titration profiles of (a) CuZnO, (b) $CuZnCeO_x$(0.2), (c) $CuZnCeO_x$(0.4), (d) $CuZnCeO_x$(0.75) and (e) $CuCeO_2$.

3.2 Catalytic Activity Test

3.2.1 Comparison between CuZnO and $CuCeO_2$

As discussed in the preceding sections, during ethanol (EtOH)-assisted CO_2 hydrogenation for methanol (MeOH) synthesis, EtOH serves as a catalytic solvent, promoting the transformation of surface-bound formate intermediates into ethyl formate (EtFm). EtFm subsequently undergoes hydrogenolysis to produce MeOH, with concurrent regeneration of EtOH (**Equation 3.1**). In parallel, EtOH can also undergo dehydrogenation to form acetaldehyde (MeCHO) or participate in coupling reactions to generate ethyl acetate (EtAc). Moreover, the reverse water-gas shift (RWGS) reaction proceeds competitively under these conditions, leading to the formation of CO as a second product. **Figure 3.9** illustrates the possible reactions involved in this study.

$$HCOOC_2H_5 + 2H_2 \rightarrow CH_3OH + C_2H_5OH \qquad \textbf{Equation 3.1}$$

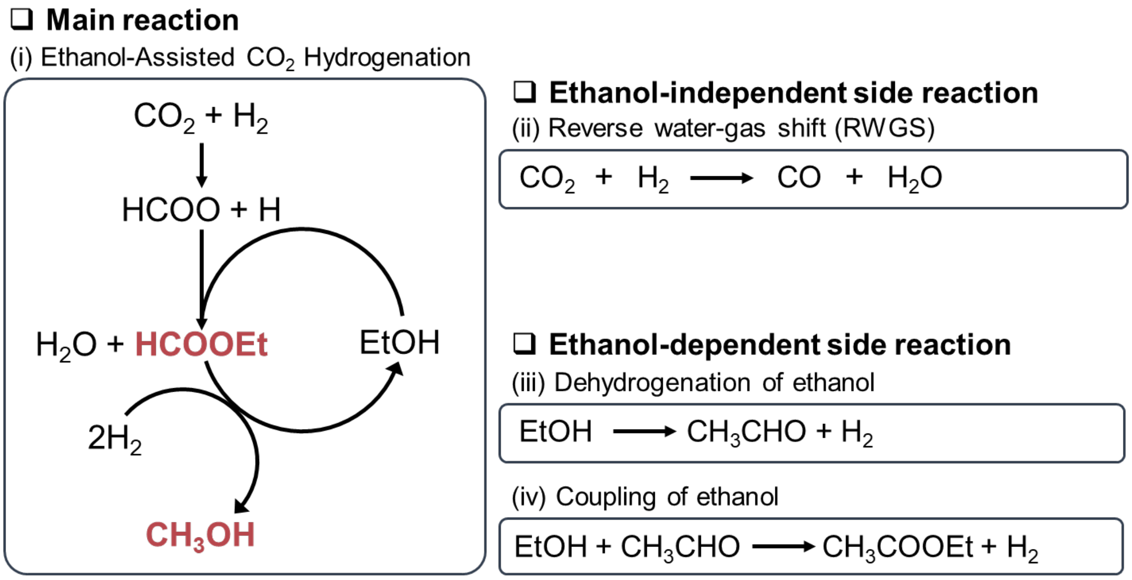

Figure 3.9 Possible reactions in this study.

doi:10.6342/NTU202502278

In this context, MeOH and EtFm are considered desired products, while MeCHO, EtAc and CO are classified as undesired byproducts. To evaluate the catalytic activity and selectivity of CuZnO and $CuCeO_2$ in EtOH-assisted CO_2 hydrogenation, catalytic tests were conducted over reaction times of 6 and 12 hours. The corresponding results are shown in **Figure 3.10**. Notably, when ZnO and CeO_2 were used to carry out the reaction under similar reaction conditions, negligible EtFm and MeOH were observed, underscoring the critical roles of Cu in this reaction (**Table 3.5**). Therefore, the product yield in this study was normalized with the amount of Cu (g-Cu) for the analysis of catalytic performance.

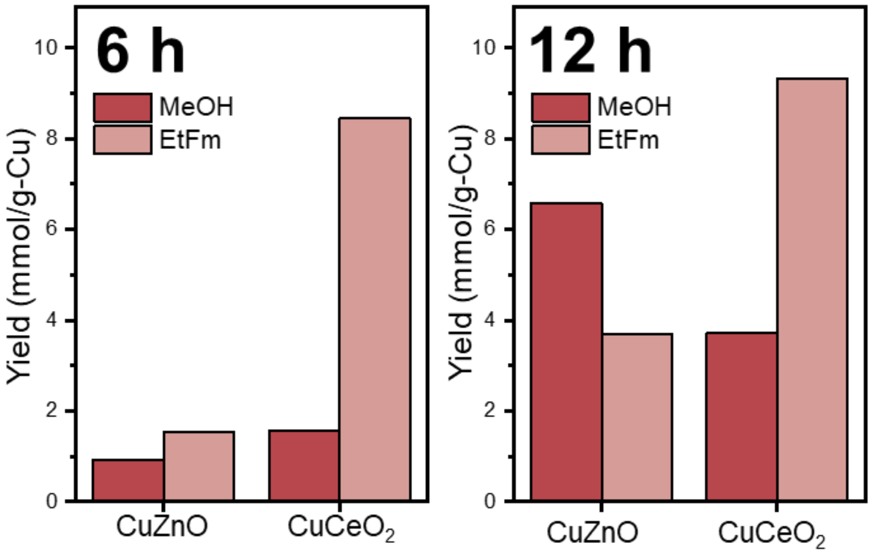

Figure 3.10 Catalytic performance of CuZnO and $CuCeO_2$ for 6 h and 12 h EtOH-assisted CO_2 hydrogenation. Reaction condition: 180 °C, 30 bar at room temperature ($H_2/CO_2 = 3$), 12 h, 0.4 g catalysts in 100 mL reactor.

After 6 hours of reaction, the product distribution over CuZnO and $CuCeO_2$ catalysts was generally comparable, with the notable exception of EtFm. While the MeOH yields remained nearly identical for both catalysts, the EtFm yield over $CuCeO_2$

doi:10.6342/NTU202502278

was approximately five times higher than that over CuZnO.

Table 3.5 Catalytic performance of ZnO and CeO_2 in EtOH-assisted CO_2 hydrogenation.

Catalyst	Product yield (mmol)				
	Desired		Undesired		
	MeOH	EtFm	MeCHO	EtAc	CO
ZnO	0.00	0.22	0.03	0.01	0.00
CeO_2	0.00	0.18	0.05	0.04	0.00
CuZnO	1.14	0.64	0.00	1.00	0.61
$CuCeO_2$	0.37	0.93	0.03	0.20	0.33

Reaction condition: 180 °C, 30 bar at room temperature ($H_2/CO_2 = 3$), 12 h, 0.4 g catalysts in 100 mL reactor.

Table 3.6 CO_2 hydrogenation without ethanol added under similar reaction conditions.

Solvent	Catalyst	Product Yield (mmol/g-Cu)				
		Desired		Undesired		
		MeOH	EtFm	MeCHO	EtAc	CO
Without Solvent	CuZnO	1.40	-	-	-	20.5
	$CuCeO_2$	0.09	-	-	-	1.64
With 20 mL of Ethanol	CuZnO	6.57	3.69	0.02	5.82	3.55
	$CuCeO_2$	3.73	9.32	0.26	1.99	3.31

Reaction condition: 180 °C, 30 bar at room temperature ($H_2/CO_2 = 3$), 12 h, 0.4 g catalysts in 100 mL reactor.

When the reaction time was extended to 12 hours, a distinct shift in product selectivity was observed. The MeOH yield over CuZnO increased significantly, reaching nearly twice that of $CuCeO_2$, while the EtFm yield over $CuCeO_2$ remained approximately two-fold higher than that of CuZnO. Given that direct CO_2 hydrogenation to MeOH is negligible at such low reaction temperatures (**Table 3.6**), the observed MeOH production can be attributed primarily to the hydrogenolysis of EtFm. Considering the combined yields of MeOH and EtFm, CuZnO achieved a total of 10.26 mmol/g-Cu with an EtFm conversion of 64.0 %, whereas $CuCeO_2$ exhibited a higher total yield of 13.05 mmol/g-Cu but a substantial lower EtFm conversion of 28.6 %. These results suggest that ceria promotes the formation of EtFm but hinders its subsequent hydrogenolysis to MeOH, while Zn-based catalysts exhibit superior activity in EtFm hydrogenolysis.

To further investigate the balance between EtFm formation and its conversion to MeOH, catalysts with varying Ce/(Ce+Zn) molar ratios were prepared and evaluated to identify an optimal composition that maximized MeOH yield while minimizing undesired byproducts.

doi:10.6342/NTU202502278

3.2.2 Catalytic Performance with Different Ce Loading

Building on the preceding insights, where $CuCeO_2$ exhibited superior EtFm productivity and CuZnO demonstrated enhanced efficiency in EtFm hydrogenolysis to MeOH, a series of bifunctional catalysts were designed by integrating Ce and Zn components to synergistically tune product selectivity. Specifically, three compositions with varying Ce/(Ce+Zn) molar ratios of 0.20, 0.40, and 0.75 were synthesized, denoted as $CuZnCeO_x(0.2)$, $CuZnCeO_x(0.4)$, and $CuZnCeO_x(0.75)$, respectively. This compositionally tuned catalyst series was aimed at balancing the high EtFm formation capability of ceria with the superior hydrogenolysis activity of Zn-containing systems. The product yields obtained after 12 hours of reaction are summarized in **Table 3.7** and presented in **Figure 3.11.**

Table 3.7 Product yield of catalysts with different Ce loading.

Catalyst	Yield (mmol/g-Cu)				
	Desired		Undesired		
	MeOH	EtFm	MeCHO	EtAc	CO
CuZnO	6.57	3.69	0.02	5.82	3.55
$CuZnCeO_x(0.2)$	15.47	3.15	0.05	5.01	3.16
$CuZnCeO_x(0.4)$	14.55	5.56	0.13	4.83	2.51
$CuZnCeO_x(0.75)$	9.70	6.26	0.17	4.08	1.79
$CuCeO_2$	3.73	9.32	0.26	1.99	3.31

Reaction condition: 180 °C, 30 bar at room temperature ($H_2/CO_2 = 3$), 12 h, 0.4 g catalysts, 20 mL EtOH in 100 mL reactor.

Catalytic performance tests revealed that Ce modest incorporation into CuZnO significantly enhanced MeOH production. Compared to CuZnO, $CuZnCeO_x(0.2)$ catalyst delivered a markedly higher total EtFm productivity of 18.62 mmol/g-Cu and an EtFm conversion of 83.1 %. This substantial improvement in both EtFm and MeOH yields is attributed to the reduced particle size (as evidenced in **Figure 3.4**), which increases the specific surface area (**Table 3.3**) and promotes higher Cu dispersion. The enhanced dispersion facilitates both the esterification of formate with EtOH and the subsequent hydrogenolysis of EtFm.

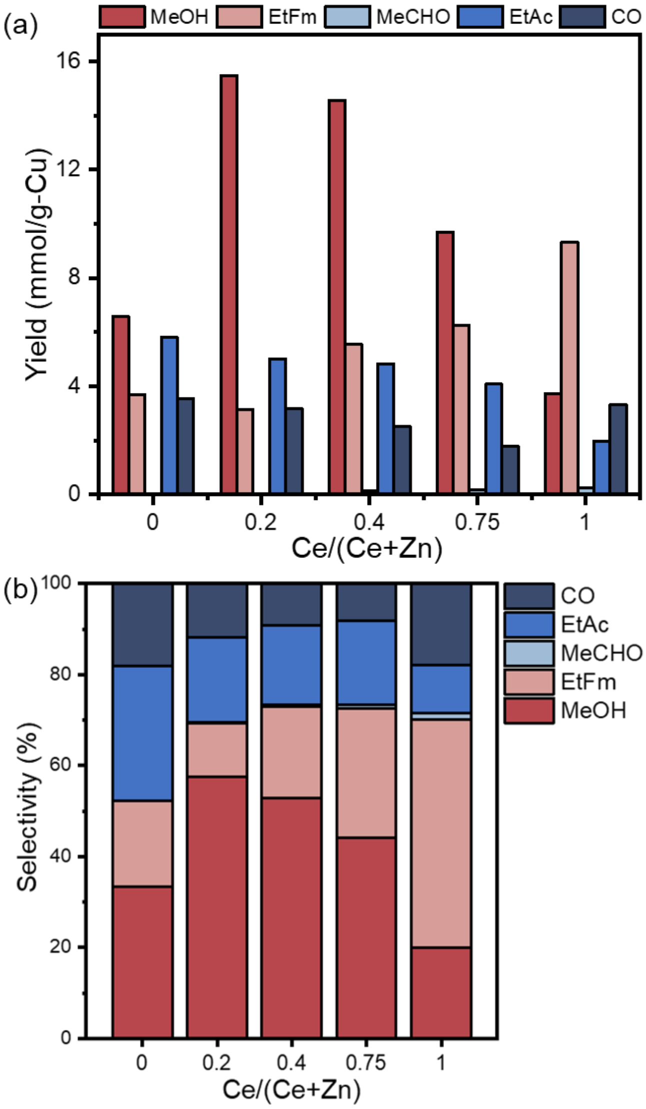

Figure 3.11 (a) Yields and (b) selectivity of products in catalytic activity tests of the catalyst with different Ce/(Ce+Zn).

Further increasing the Ce content to $CuZnCeO_x$(0.4) led to a total EtFm yield rose to 20.11 mmol/g-Cu; however, the EtFm conversion declined to 72.4%, suggesting that although EtFm formation was further promoted with high catalyst specific surface area, its subsequent hydrogenolysis to MeOH became inhibited. This behavior is likely due to excessive ceria coverage or reduced Zn-associated active sites essential for EtFm hydrogenolysis. The inhibitory effect became more pronounced at higher Ce loading: when CuZnCeO$_x$(0.75) catalyst was employed, both the total MeOH yield and EtFm conversion decreased to 15.95 mmol/g-Cu and 60.8%, respectively.

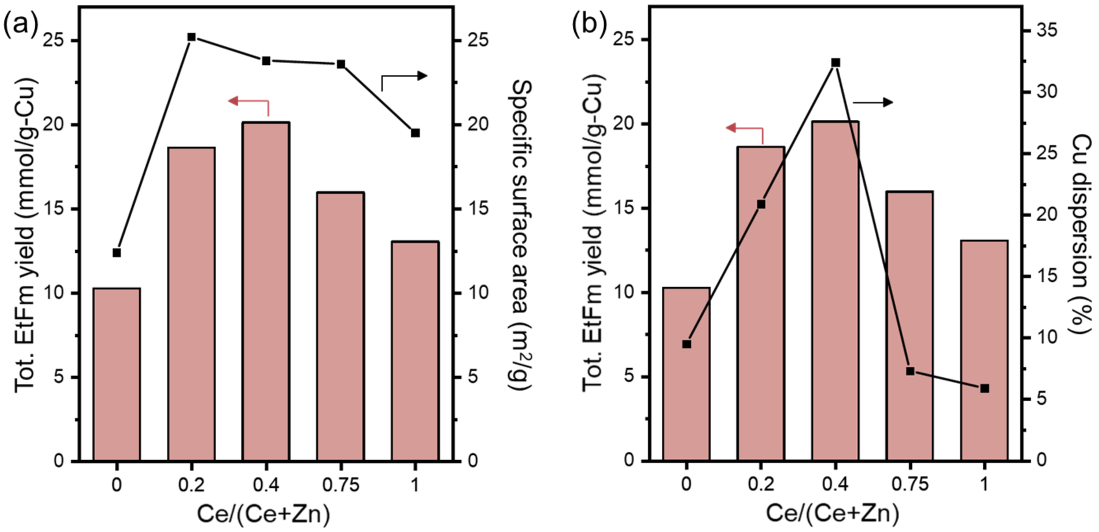

Figure 3.12 Correlation of total yields of EtFm with (a) specific surface area and (b) Cu dispersion of CuZnCeO$_x$ catalysts.

By comparing to other catalytic properties (**Appendix 10**), the catalyst specific surface area and Cu dispersion exhibited strong correlation with the total EtFm yield, as illustrated in **Figure 3.12**. As discussed in the catalyst characterization, the particle size reduced significantly upon Ce incorporation into CuZnO, leading to an increase in specific surface area. This improvement accounted for the enhancement in Cu dispersion, where more Cu surface was exposed. As the main active sites (**Table 3.5**), the higher accessibility to the Cu sites resulted in the higher EtFm yield.

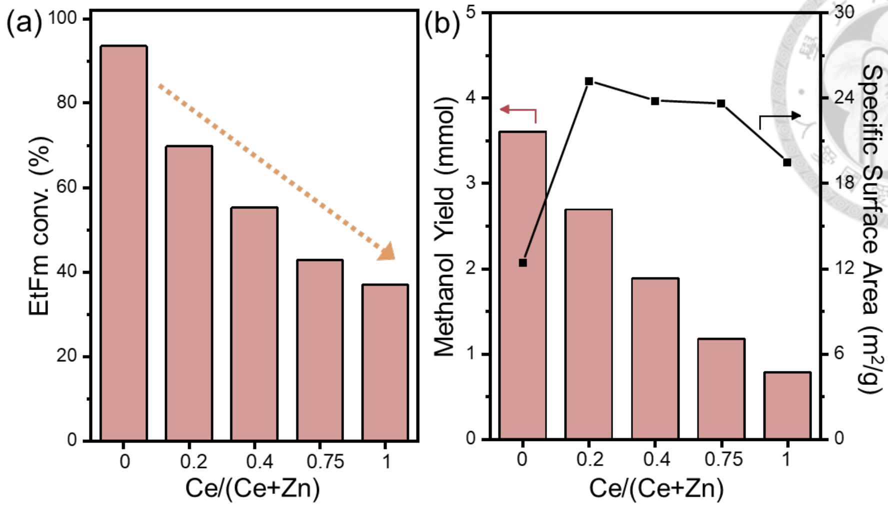

Figure 3.13 (a) EtFm conversion and (b) MeOH yield during hydrogenolysis of EtFm. Reaction condition: 180 °C, 30 bar at room temperature ($H_2/N_2 = 3$), 0.4 g catalysts, 20 mL EtOH and 5 mmol (400 μL) EtFm in 100 mL reactor.

To validate this hypothesis, a series of hydrogenolysis reactions were conducted using EtFm as the feedstock over the same set of catalysts. The results revealed that the hydrogenolysis of EtFm is not a spontaneous process and requires catalysts to proceed efficiently, thereby confirming that the differences in EtFm conversion and MeOH yield originate from the intrinsic properties of the catalysts. Consistent with the trends observed during EtOH-assisted CO_2 hydrogenation, EtFm conversion systematically decreased with increasing Ce content (**Figure 3.13**). These findings further corroborate that while ceria promotes EtFm formation (**Figure 3.10**), excessive Ce loading impedes its subsequent hydrogenolysis to MeOH, likely by modifying the surface properties and reducing the number of active hydrogenolysis sites. In contrast, Zn-containing sites were found to facilitate EtFm hydrogenolysis effectively, emphasizing the critical importance of achieving an optimal balance between Ce and Zn components to maximize overall catalytic performance in terms of MeOH yield and selectivity, as shown in **Figure 3.11**.

3.3 IR Spectroscopy – Impact of Ce Incorporation on Product Selectivity

3.3.1 Carbonate and Formate Species on Catalyst Surface

Infrared (IR) spectroscopy was employed to investigate surface-adsorbed species and gain molecular-level insights into the interaction between reactants and the catalyst surface, which can critically influence catalytic performance. In this study, diffuse reflectance infrared Fourier transform spectroscopy (DRIFTS) was utilized to observe the molecular transformation under *in-situ* conditions.

As previously discussed, CO_2 can adsorb onto catalysts surfaces in various configurations, forming carbonate species that differ depending on the nature of the adsorption site and the strength of surface interactions. For example, CO_2 may react with surface hydroxyl groups to form bicarbonate species, However, in the present study, the characteristic bands of δ(OH) and ν(OH) near 1200 and 3600 cm^{-1}, respectively, were absent upon the CO_2 adsorption. As a result, bicarbonate species were excluded from further discussion. Instead, the analysis focused on monodentate, bidentate, and bridged carbonate species, with their corresponding vibrational assignments summarized in **Table 3.8**.

Following the introduction of the CO_2 and H_2 gas mixture to the catalyst surface, the formation of surface-bound formate species was anticipated, provided that suitable active sites were available. Similar to carbonate species, formate can adsorb in various geometries, monodentate, bidentate, or bridged, depending on the nature of its interaction with catalyst surface. These adsorption configurations result in distinct vibrational features, and the corresponding IR band assignments are summarized in **Table 3.9**.

doi:10.6342/NTU202502278

Table 3.8 General assignment of IR bands of CO_2 adsorbed on CuZnO and $CuCeO_x$. M denotes a metal center (Cu, Zn and/or Ce), where the adsorbate may bind to a single metal atom or bridge two distinct metal atoms.[56-61]

Carbonate	Configuration	Vibration	This study		Literature	
			IR bands (cm^{-1})		IR bands (cm^{-1})	
			CuZnO	$CuCeO_2$	CuZnO	$CuCeO_2$
Monodentate	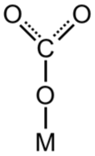	$\nu(CO)$	-	-	-	1020
		$\nu_s(CO_3)$	1370	-	1370	1358
		$\nu_{as}(CO_3)$	1480	-	1480	1464
Bidentate	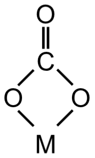	$\nu(CO)$	-	1020	-	1020
		$\nu_s(CO_3)$	1330	1290	1323	1292
		$\nu_{as}(CO_3)$	1515	1590	1515	1589
Bridged	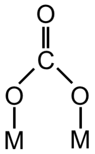	$\delta(CO_3)$	-	1020	1020	1020
		$\nu_s(CO_3)$	-	1290	1220	1290
		$\nu_{as}(CO_3)$	-	1620	1600	1620

Table 3.9 General assignment of IR bands of formate adsorbed on ZnO and CeO_2. M denotes a metal center (Cu, Zn and/or Ce), where the adsorbate may bind to a single metal atom or bridge two distinct metal atoms.[56,57,62,63]

Formate	Configuration	Vibration	This study		Literature	
			IR bands (cm^{-1})		IR bands (cm^{-1})	
			CuZnO	$CuCeO_2$	CuZnO	$CuCeO_2$
Monodentate	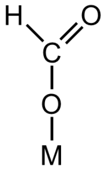	$\nu_s(OCO)$	-	-	1320	1320
		$\delta(CH)$	-	-	1371	1369
		$\nu_{as}(OCO)$	-	-	1605	1600
Bidentate	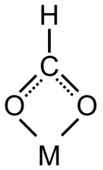	$\nu_s(OCO)$	-	-	1371	1360
		$\delta(CH)$	-	-	1381	1372
		$\nu_{as}(OCO)$	-	-	1572	1545
Bridged	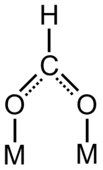	$\nu_s(OCO)$	1370	1360	1363	1370
		$\delta(CH)$	1380	-	1383	-
		$\nu_{as}(OCO)$	1580	1590	1581	1585

After catalyst pretreatment, either CO_2 or a H_2/CO_2 gas mixture (3:1) was introduced to ZnO or CuZnO for 20 minutes to allow for saturated adsorption of surface species. Subsequently, pure Ar was flowed over the catalysts for an additional 20 minutes to purge gaseous-phase molecules and physisorbed species. DRIFTS spectra were then captured under Ar flow at 180 °C, as presented in **Figure 3.14**.

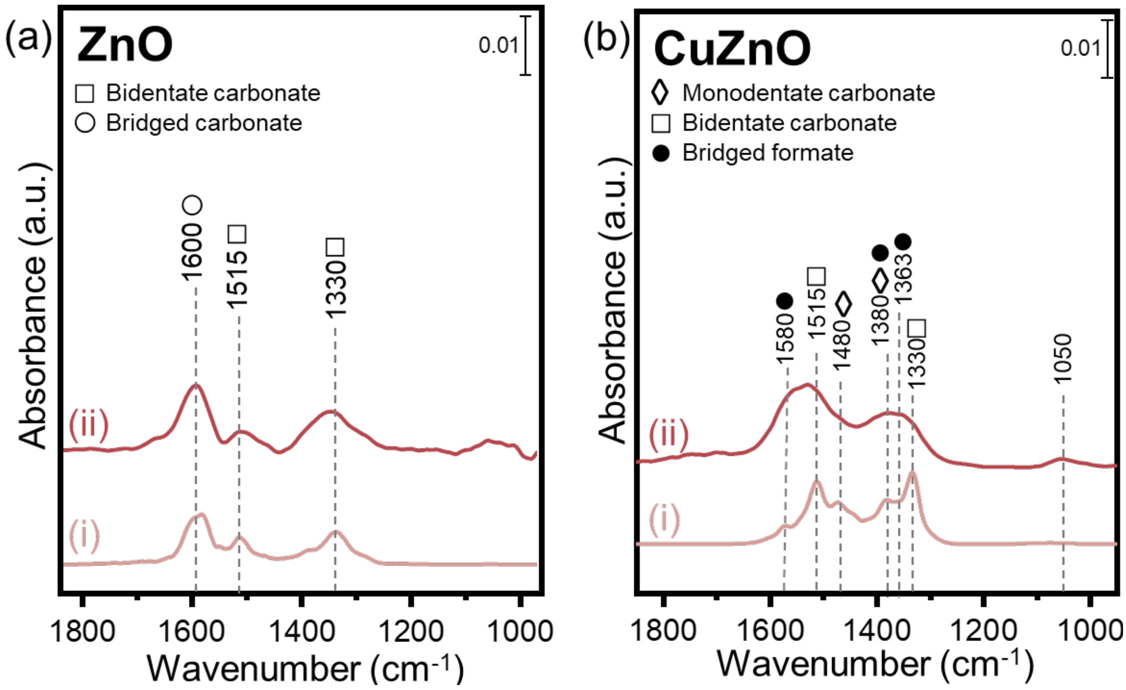

Figure 3.14 Adsorbed species on (a) ZnO and (b) CuZnO after exposure to (i) CO_2 or (ii) $CO_2 + H_2$ for 20 minutes, followed by Ar purging for 20 minutes at 180 °C.

Distinct differences were observed in the DRIFTS spectra of ZnO and CuZnO following CO_2 exposure, as illustrated in **Figure 3.14.** For ZnO, IR bands appeared at 1330, 1515 and 1600 cm^{-1}. The bands at 1330 and 1515 cm^{-1} are assigned to the symmetric ($\nu_s(CO_3)$) and asymmetric ($\nu_{as}(CO_3)$) stretching vibration of bidentate carbonate, respectively. The band at 1600 cm^{-1}, observed exclusively on ZnO is attributed to the $\nu_{as}(CO_3)$ of bridged carbonate species. In contrast, CuZnO exhibited two additional bands at 1370 and 1480 cm^{-1}, which are characteristic $\nu_s(CO_3)$ and $\nu_{as}(CO_3)$ stretching vibration of monodentate carbonate species. The emergence of these bands upon Cu incorporation suggests a modified surface adsorption environment, likely arising from electronic alterations in ZnO induced by the presence of Cu.[64] These changes influence the coordination geometry and binding mode of CO_2-derived species on the catalysts surface.

Upon exposure to a CO_2 and H_2 gas mixture, ZnO exhibited IR spectra nearly identical to those observed under CO_2 alone, with bands at 1330, 1515, and 1600 cm^{-1} corresponding to bidentate and bridged carbonate species, respectively. The absence of formate-related bands indicates that ZnO alone lacks the capacity to activate H_2 and convert the carbonate species into surface formate intermediates, and is thus inactive for MeOH synthesis. In contrast, CuZnO displayed distinct spectral changes under CO_2/H_2 conditions, most notably the appearance of a band at 1580 cm^{-1}, which is attributed to the asymmetric ($\nu_s(OCO)$) stretching vibration of bridged formate species. Although overlapping features around 1363 and 1380 cm^{-1} obscured clear assignments for the symmetric ($\nu_s(OCO)$) and ($\delta(CH)$), the presence of the 1580 cm^{-1} band provides strong evidence for the formation of surface-bound formate species on Cu-containing catalysts under reaction conditions. Additionally, a weak band at 1050 cm^{-1} was observed, corresponding to surface methoxy species, indicating partial hydrogenation of formate intermediates on CuZnO.

Similar to ZnO, CeO_2 exhibited bidentate and bridged carbonate species upon CO_2 exposure (**Figure 3.15**). The IR bands of 1020, 1290 and 1580 cm^{-1} are assigned to the $\nu(CO)$, symmetric $\nu_s(CO_3)$ and asymmetric $\nu_{as}(CO_3)$ stretching vibrations of bidentate carbonate, respectively. In contrast, bridged carbonate species were observed on $CuCeO_2$, with bands at 1290 and 1620 cm^{-1}, which correspond to $\nu_s(CO_3)$ and $\nu_{as}(CO_3)$ stretching vibrations. Additionally, the formation of carboxylate-like species was confirmed by a distinct band at 1690 cm^{-1}, also observed in prior studies.[65]

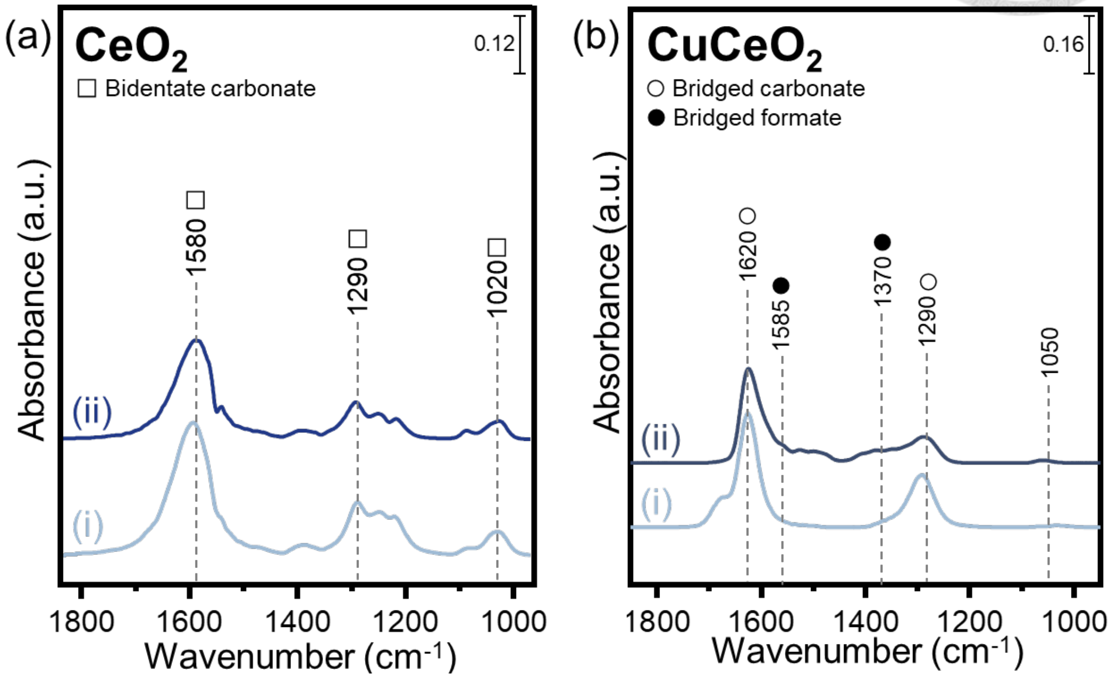

Figure 3.15 Adsorbed species on (i) CeO_2 and (ii) $CuCeO_2$ after exposure to (a) CO_2 or (b) $CO_2 + H_2$ for 20 minutes, followed by Ar purging for 20 minutes at 180 °C.

When exposed to a CO_2/H_2 gas mixture, CeO_2 exhibited no significant changes in its IR spectra compared to CO_2 alone. The persistent bands at 1290 and 1590 cm^{-1} (bidentate carbonate) suggests that CeO_2 alone is incapable of converting adsorbed carbonate species into formate intermediates in the absence of Cu. In contrast, $CuCeO_2$ exhibited weak bands at 1370 and 1585 cm^{-1}, which are attributed to the symmetric ν_s(OCO) and asymmetric ν_{as}(OCO) stretching vibrations of the bridged formate species. Additionally, a weak band at 1050 cm^{-1} was also detected on $CuCeO_2$ formed, suggesting partial hydrogenation of formate intermediates. Furthermore, the disappearance of the 1690 cm^{-1} carboxylate band upon CO_2/H_2 exposure is likely due to its consumption *via*

doi:10.6342/NTU202502278

the reverse water-gas shift (RWGS) reaction, leading to CO formation.[19]

The DRIFTS spectra discussed above highlight that the promoter oxides alone (i.e. ZnO and CeO_2) lack the intrinsic ability to activate H_2 and generate formate species under these conditions. In contrast, Cu incorporation into ZnO and CeO_2 significantly alters surface reactivity, enabling the formation of bidentate formate species on CuZnO and $CuCeO_2$. The next section will examine the reactivity of these surface-bound formate species upon EtOH introduction, offering further mechanistic insight into EtOH-assisted CO_2 hydrogenation.

doi:10.6342/NTU202502278

3.3.2 *In-situ* Reaction of Formate with Ethanol

In EtOH-assisted CO_2 hydrogenation, a critical step involves the esterification of surface-bound formate species with EtOH to generate EtFm, which subsequently undergoes hydrogenolysis to produce MeOH. In this study, formate species were first generated by exposing the catalyst to a CO_2/H_2 gas mixture, followed by Ar purging to remove vapor-phase molecules and weakly adsorbed species. EtOH, carried by an Ar flow, was then introduced over the formate-precovered surface, and the evolution of surface species was monitored *in-situ*. The spectral changes during the initial 0.7 minutes of EtOH exposure are presented in **Figure 3.16**.

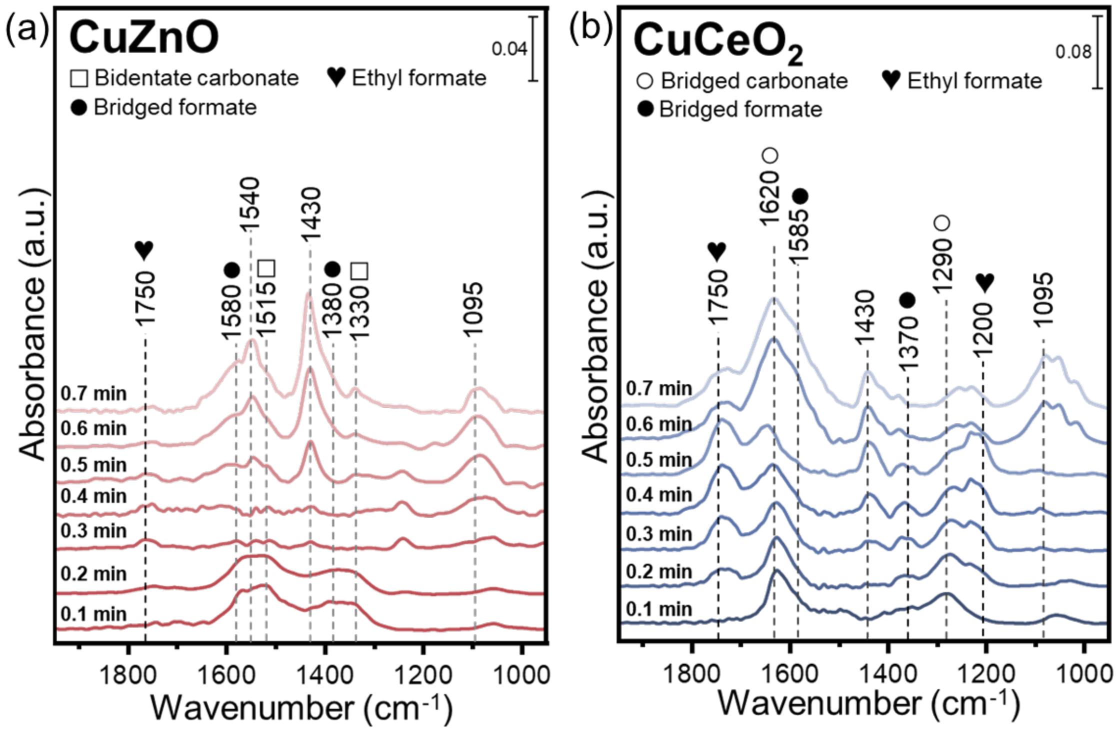

Figure 3.16 *In-situ* reaction of formate species upon introduction of ethanol at 180 °C.

On CuZnO, the bridged formate species, characterized by bands at 1380 (δ(CH)) and 1580 cm^{-1} (ν_{as}(OCO)), rapidly decreased and eventually disappeared following EtOH introduction. Concurrently, the bidentate carbonate signal at 1330 and 1515 cm^{-1} also declined, which is attributed to reactions between CO_2 and EtOH leading to the formation of organic carbonates, though this lies beyond the scope of the present study. The characteristic C=O stretching (ν(C=O) of EtFm, typically near 1750 cm^{-1} (**Figure 3.17**), was not distinctly observed and is further discussed through comparison with $CuCeO_2$. The disappearance of formate bands is ascribed to their reaction with EtOH rather than desorption, since weakly bound formate would have been effectively removed during Ar purging. Following formate consumption, new bands emerged at 1095, 1430 and 1540 cm^{-1}. The 1095 cm^{-1} band corresponds to the C-O stretching vibration of surface-bound ethoxy species[66], while the 1430 and 1540 cm^{-1} bands are assigned to acetate species[67], likely arising from transformation of MeCHO, the primary dehydrogenation product of EtOH. The similar IR bands were detected as EtOH adsorbed on CuZnO at 180 °C, as illustrated in **Figure 3.18**.

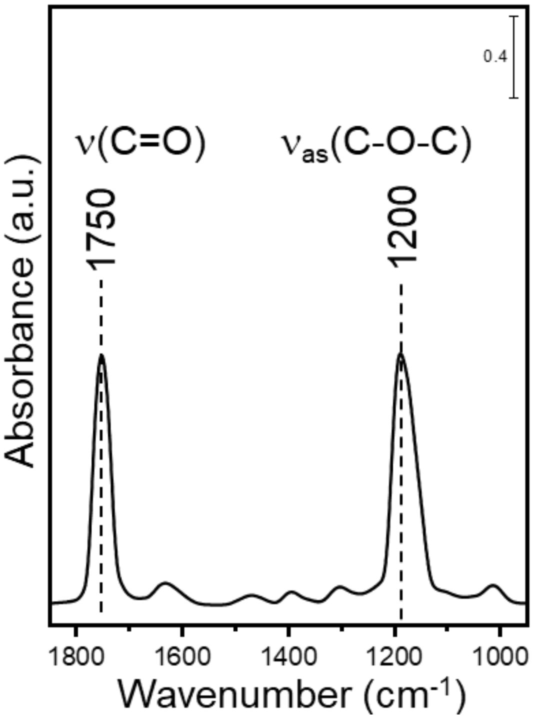

Figure 3.17 DRIFTS spectrum of ethyl formate (EtFm).

doi:10.6342/NTU202502278

A similar trend was observed on $CuCeO_2$, where the signals corresponding to bridged formate (1370 and 1585 cm^{-1}) and bridged carbonate species (1290 and 1620 cm^{-1}) diminished following EtOH introduction. Simultaneously, bands at 1200 and 1750 cm^{-1} intensified, accompanied by the appearance of a weak band at 1430 cm^{-1}. The 1200 and 1750 cm^{-1} bands are assigned to the asymmetric C-O-C stretching (ν_{as}(O-C-O)) and the C=O stretching (ν(C=O)) of EtFm, respectively,[68] while the weak 1430 cm^{-1} band indicates a relatively low concentration of acetate species compared to CuZnO (**Figure 3.17 (a)**). A key distinction from CuZnO is the sharp increase in the 1620 cm^{-1} band, attributed to the $\nu_{as}(CO_3)$ of bridged carbonate species. Additionally, the more intense 1750 cm^{-1} signal observed on $CuCeO_2$, relative to CuZnO, is consistent with catalytic results, suggesting the role of Ce in promoting EtFm formation while simultaneously inhibiting its further hydrogenolysis.

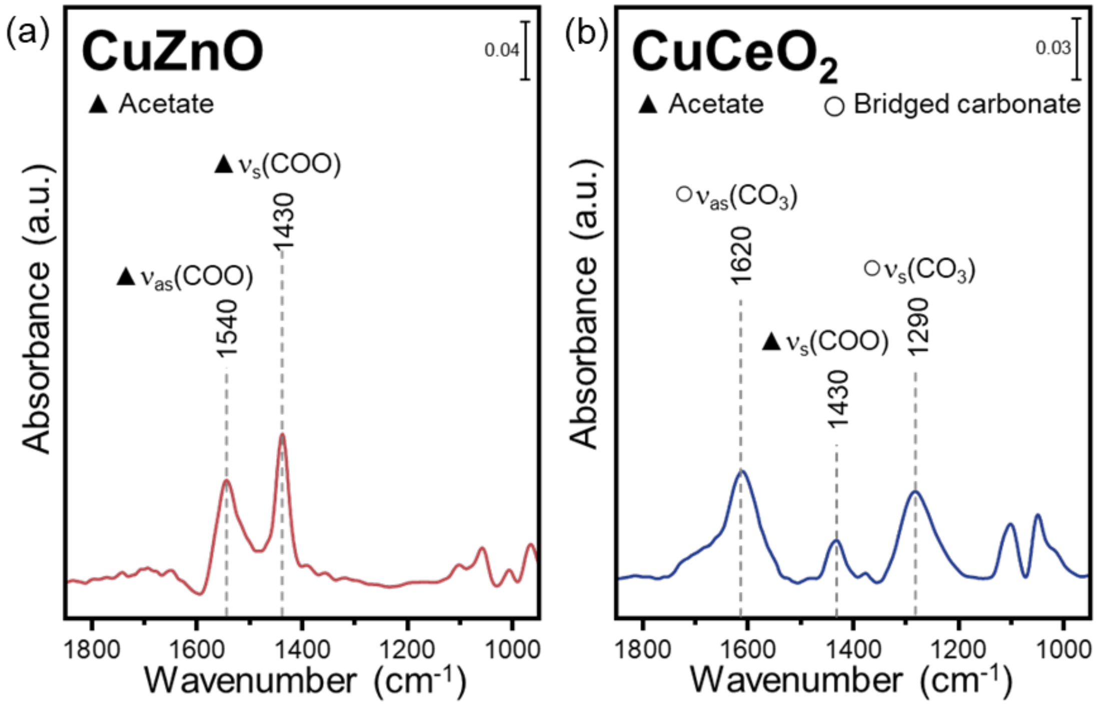

Figure 3.18 DRIFTS spectra of adsorbed EtOH on (a) CuZnO and (b) $CuCeO_2$ at 180 °C.

A previous study employing isotope labeling demonstrated that the co-adsorption of the carbonyl (C=O) group in methyl formate is essential for its complete hydrogenolysis into two MeOH molecules.[69] The reported mechanism was illustrated in **Figure 3.19**. By analogy, it is proposed that a similar adsorption configuration is required for the conversion of EtFm into MeOH and EtOH. Based on the distinct surface species observed on CuZnO and $CuCeO_2$, this study suggests that EtFm adopts different adsorption geometries and interactions depending on the catalyst surface. These variations in surface binding modes are believed to underlie the divergent catalytic behaviors observed during EtOH-assisted CO_2 hydrogenation.

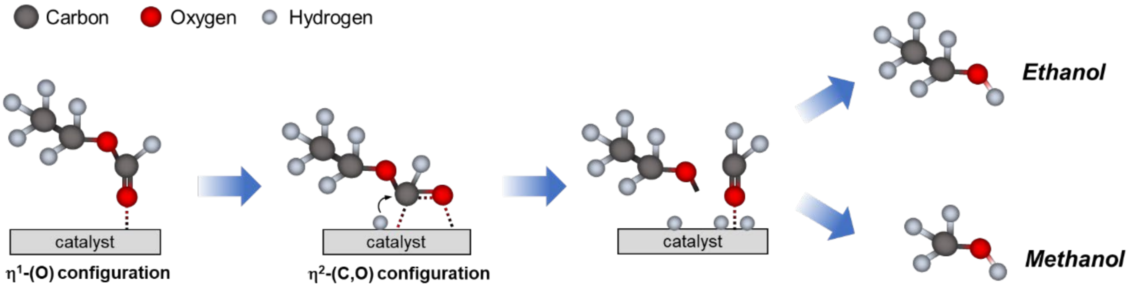

Figure 3.19 Mechanism of ethyl formate (EtFm) hydrogenolysis analogous to the reported mechanism of methyl formate hydrogenolysis.[69]

Figure 3.20 illustrates the proposed adsorption configurations of EtFm on CuZnO and $CuCeO_2$ surfaces, which are key to understanding their distinct catalytic behaviors. On CuZnO, the relatively shorter interatomic distances between surface atoms allow both the carbon and oxygen atoms of the carbonyl group (C=O) to simultaneously interact with the surface, stabilizing an η^2 adsorption geometry. In this configuration, hydrogen activated by Cu sites can readily attack the carbonyl carbon, promoting C=O bond activation and subsequent conversion *via* hydrogenolysis. This reaction pathway leads to the readily C-O ester bond breaking to form ethoxy and methoxy intermediates, which are further hydrogenated to yield EtOH and MeOH, respectively.

In contrast, the suppression of hydrogenolysis of EtFm on $CuCeO_2$ is attributed to the less favorable η^1 adsorption geometry. Due to the larger interatomic spacing between Ce atoms compared to Zn, the surface cannot effectively stabilize η^2-bound EtFm. Instead, EtFm interacts weakly with the surface *via* single-point (η^1) coordination. This limited interaction hinders the activation of the carbonyl group, thereby preventing ester bond cleavage. As a result, EtFm is prominently observed in **Figure 3.17 (b)** when EtOH was introduced to formate-precovered $CuCeO_2$. EtFm remains largely unreactive on $CuCeO_2$, leading to its accumulation and the inhibition of subsequent hydrogenolysis.

doi:10.6342/NTU202502278

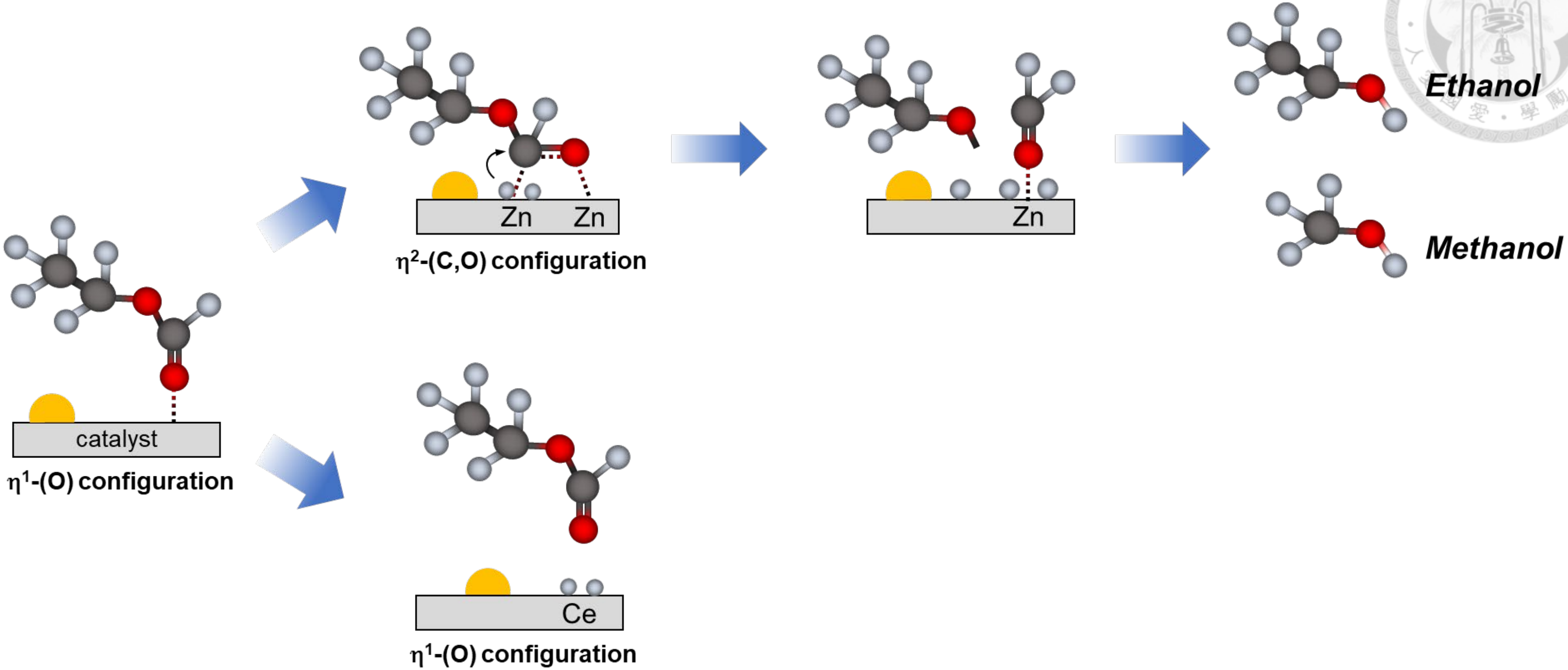

Figure 3.20 Proposed adsorption and interaction of ethyl formate (EtFm) over CuZnO and $CuCeO_2$, which leads to different catalytic performance.

doi:10.6342/NTU202502278

3.4 RWGS and Alcohol-Dependent Side Reactions

RWGS reaction is an unavoidable reaction during CO_2 hydrogenation, even though the selectivity is relatively low at the reaction conditions in this study. As shown in **Figure 3.21**, the yield of CO remains below 4 mmol/g-Cu across all catalysts.

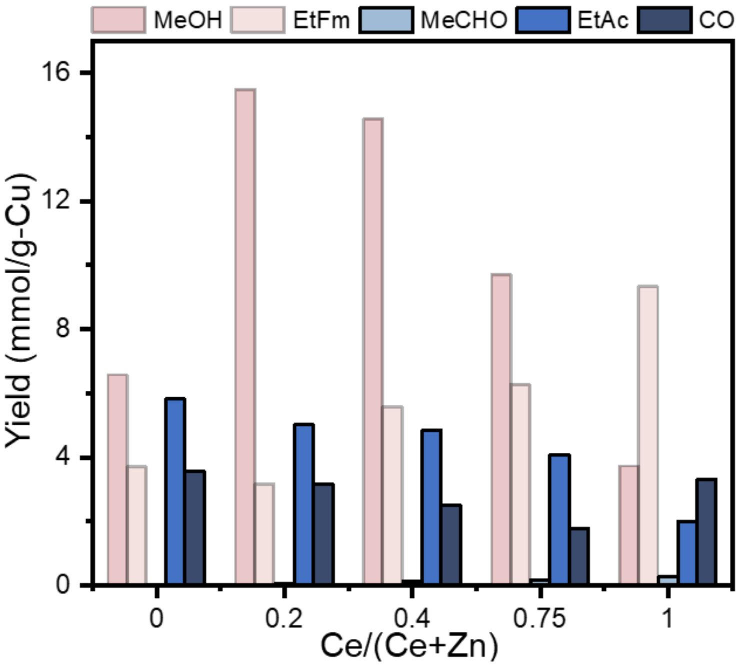

Figure 3.21 Yield of acetaldehyde (MeCHO), ethyl acetate (EtAc), and carbon monoxide (CO) in catalytic activity test using catalysts with different Ce/(Ce+Zn).

Two factors rationalize this trend. First, the slight increase in Lewis acidity imparted by Ce^{4+} stabilizes surface formate, thereby disfavoring its decomposition to CO.[70] The $CuZnCeO_x$ catalyst, which possesses large species surface areas, further channels formate into esterification with EtOH, suppressing RWGS-derived CO. Second, at the highest Ce loading (*i.e.*, $CuCeO_2$), the abundance of Ce^{3+} stabilizes carboxylate intermediates,[71] providing an alternative pathway for CO formation that is independent of formate decomposition.[19] Consequently, the optimal catalyst $CuZnCeO_x$(0.2) combines minimal CO evolution with low by-product formation while maximizing MeOH productivity, underscoring the balanced role of Ce in steering both desired and undesired reaction channels.

Meanwhile. EtOH inevitably interacts with catalysts, undergoing dehydrogenation and coupling reactions, which lead to the formation of MeCHO and EtAc, respectively. A trend emerged whereby increasing Ce content resulted in higher MeCHO yield and lower EtAc yields (**Figure 3.21**). According to the established mechanism for EtAc ($CH_3COOCH_2CH_3$) formation from EtOH (**Figure 1.7** in section 1.3), MeCHO must first form acetyl (CH_3CO) species, which subsequently react with EtOH-derived ethoxy (CH_3CH_2O) species to complete the coupling process. It is hypothesized that MeCHO interacts weakly with the CeO_2 surface, thereby suppressing the formation of surface-bound acetyl intermediates. As a result, EtAc formation is hindered, leading to the accumulation of MeCHO as Ce content increases.

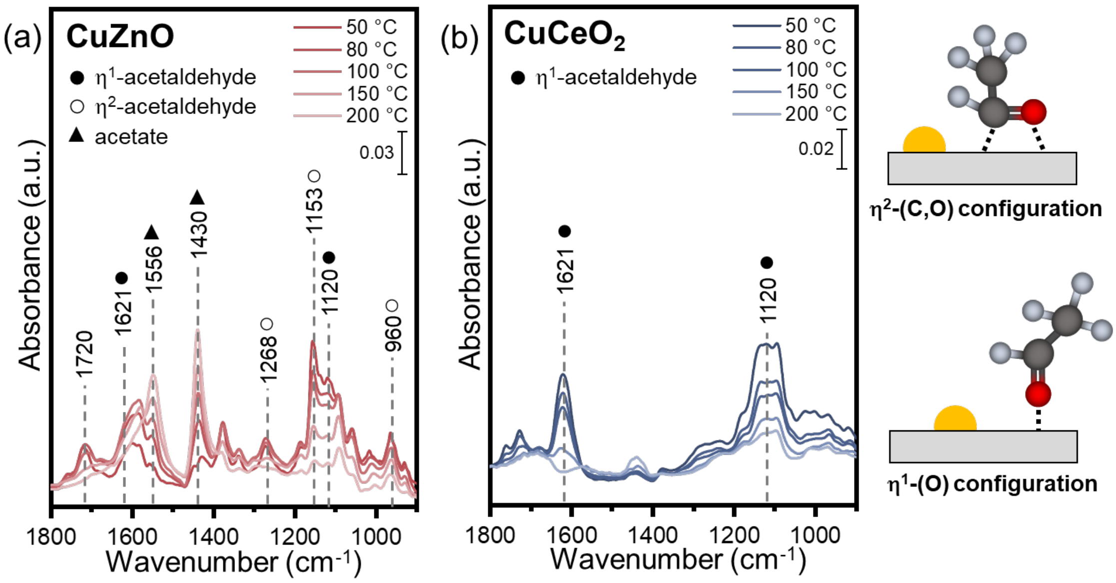

Figure 3.22 *In-situ* DRIFTS spectra of adsorption and interaction of acetaldehyde (MeCHO) on (a) CuZnO and (b) $CuCeO_2$.

To elucidate the mechanistic basis of this relationship, *in-situ* DRIFT spectroscopy was employed to investigate the adsorption behavior and surface interactions of MeCHO on CuZnO and CuCeO$_2$, as presented in **Figure 3.22**. The DRIFTS spectra collected at 50 °C revealed distinct differences in the adsorption modes of MeCHO between the two catalysts. On both CuZnO and CuCeO$_2$, IR bands at 1120 and 1621 cm^{-1} were observed and are assigned to the ν(C-C) and ν(C=O) vibrations of η^1-MeCHO species, respectively.[72] However, additional IR bands at 960, 1153 and 1268 cm^{-1} were exclusively detected on CuZnO. These bands are attributed to ρ(CH$_3$), ν(C-C), and ν(C-O) vibrations of η^2-MeCHO species,[73] indicating a more diverse and stronger adsorption configuration on CuZnO.

Upon heating, the thermal behavior of the adsorbed MeCHO species diverges significantly between the catalysts. On CuCeO$_2$, the η^1-MeCHO bands gradually diminished with increasing temperature without the appearance of new IR features, suggesting weak adsorption and subsequent desorption without further reaction. In contrast, on CuZnO, the η^1-MeCHO bands at 1621 cm^{-1} remained relatively stable, while the η^2-MeCHO bands (960, 1153, and 1268 cm^{-1}) decreased in intensity. Concurrently, new bands emerged at 1430 and 1556 cm^{-1}, corresponding to the symmetric (ν_s(COO)) and asymmetric (ν_{as}(COO) stretching vibrations of acetate species, respectively. These results suggest that MeCHO, when adsorbed as η^2-MeCHO on CuZnO, undergoes further surface transformations with η^2-MeCHO serving as a reactive intermediate to acetate formation.

These spectroscopic insights align with the catalytic trends discussed earlier, where increasing Ce content in the catalyst composition led to decreased EtAc production and a corresponding increase in MeCHO accumulation. The *in-situ* DRIFTS data support this observation by showing that $CuCeO_2$ favors the formation of η^1-MeCHO, which interacts only weakly with the surface and does not undergo further transformation. Literature reports have shown that the surface oxygen species can oxygenate acetyl intermediates to form acetate.[74] However, since η^1-MeCHO lacks the necessary reactivity to form acetyl species, its prevalence suppresses the pathway to EtAc formation, as illustrated in **Figure 1.7**.

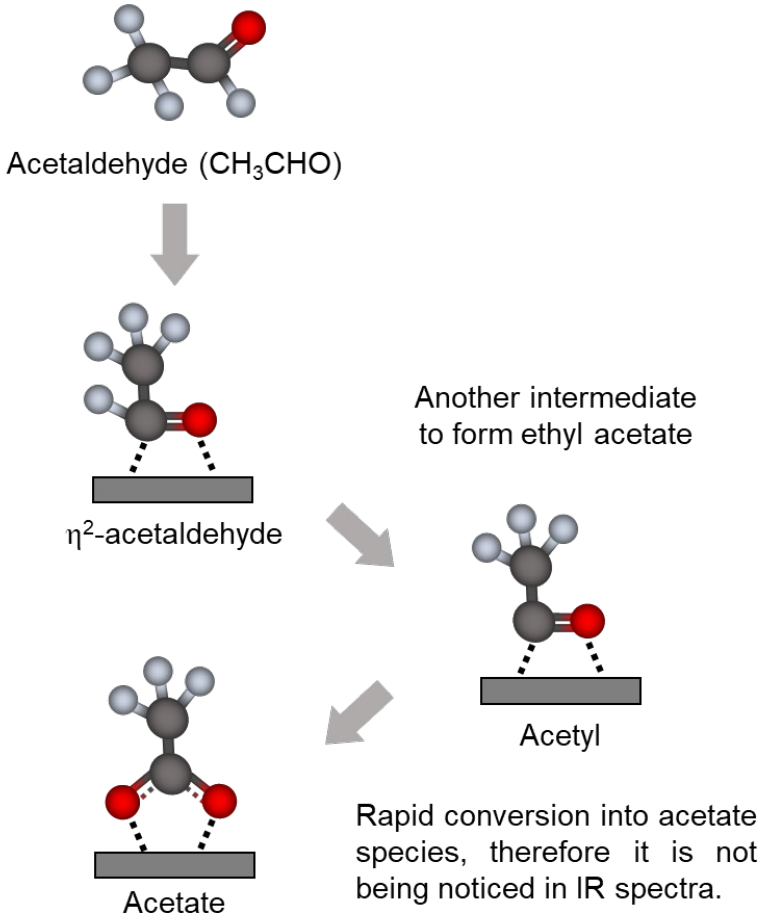

Figure 3.23 Proposed interaction of η^2-MeCHO over CuZnO to form acetate species.

Conversely, η^2-MeCHO is capable of further C-H bond activation, generating the acetyl intermediate (CH_3CO). This intermediate may follow one of two pathways: it can couple with surface ethoxy species to produce EtAc, or it may be oxidized by lattice

doi:10.6342/NTU202502278

oxygen to yield acetate (CH_3COO^-). This mechanistic framework, shown in **Figure 3.23**, provides a coherent explanation for the higher EtAc yields and lower MeCHO accumulation observed on Zn-rich catalysts. Although the characteristic IR band of the acetyl intermediate, typically reported around 1650 cm^{-1} (ν(C=O)), was not observed in this study, its absence is likely due to its transient nature and rapid surface reactivity. In the presence of ethoxy species, the acetyl intermediate is expected to rapidly couple to form EtAc. Alternatively, in the absence of ethoxy species, swift oxidation of the acetyl intermediate to acetate may occur, as seen in **Figure 3.22 (a).** These rapid transformations likely prevent the accumulation of detectable acetyl species under the experimental conditions.

doi:10.6342/NTU202502278

CHAPTER 4 CONCLUSION

In this study, a series of $CuZnCeO_x$ catalysts were prepared *via* co-precipitation method and evaluated for ethanol (EtOH)-assisted CO_2 hydrogenation at low temperatures, with a focus on methanol (MeOH) production. A comprehensive suite of characterization techniques, coupled with *in-situ* DRIFTS, was employed to elucidate the key physicochemical factors affecting catalytic activity and product selectivity.

Catalytic testing revealed that the incorporation of cerium (Ce) significantly influenced performance, enhancing both MeOH yield and selectivity. Systematic variation of the Ce/(Ce+Zn) ratio uncovered a bifunctional promotional effect: Ce facilitated the formation of ethyl formate (EtFm), a crucial reaction intermediate, while Zn promoted its subsequent hydrogenolysis to MeOH. Among the catalysts tested, those with moderate Ce content delivered the optimal MeOH yield, effectively balancing intermediate formation with downstream conversion.

Mechanistic insights derived from in-situ DRIFTS studies provided further clarification of the origin of the observed catalytic behaviors. Upon introducing ethanol to formate-preadsorbed catalysts, distinct surface transformations were detected. On CuZnO, the EtFm-related bands were relatively weak and transient, indicating weak adsorption and rapid conversion. In contrast, $CuCeO_2$ exhibited stronger and more persistent EtFm signals, suggesting stronger surface binding and slower transformation. These differences are attributed to the distinct adsorption geometries stabilized on each catalyst. The relatively short interatomic distances on CuZnO favored an η^2-(C,O) adsorption configuration, which enabled efficient activation of the carbonyl group and subsequent hydrogenolysis to methanol. Conversely, the larger interatomic spacing on $CuCeO_2$ stabilized EtFm in an η^1-O binding mode, which limited interaction with surface hydrogen species and suppressed its conversion to methanol.

These findings underscore the critical role of adsorption geometry in determining reaction pathways and catalytic outcomes. Most importantly, the results demonstrate that fine-tuning promoter composition, specifically Ce/(Ce+Zn) ratio, can strategically modulate the balance between intermediate generation and product formation. This work offers valuable design principles for the development of next-generation Cu-based catalysts for efficient alcohol-assisted CO_2 hydrogenation under mild conditions.

doi:10.6342/NTU202502278

CHAPTER 5 FUTURE WORK

1. Catalyst Design Optimization

Future studies should systematically reduce Cu loading to suppress agglomeration and increase the fraction of exposed active sites. Catalysts can be synthesized by dispersion-oriented routes, such as deposition-precipitation and wetness impregnation, and benchmarked against the current co-precipitated baseline. The activity and selectivity should be correlated with particle sizes, interfacial density, Cu^0/Cu^+ speciation and so on.

2. Practicality for Industrial Translation

(a) Continuous-flow operation

Transitioning from batch to continuous mode will involve a fixed-bed to trickle-bed reactor equipped with on-line ethanol recycle and precise gas-liquid dosing. Experiments at industrially relevant space velocities will verify steady-state selectivity, and establish the catalyst's throughout before noticeable performance loss.

(b) Long-run stability and catalyst reusability

Extended time-on-stream tests combined with multiple reduction-reaction cycles will quantify intrinsic deactivation kinetics and regeneration requirements. More post-run characterization should be employed to diagnose sintering, phase segregation of catalysts.

(c) Process simulation and sustainability metrics

Data and results from the experiments should be populated to Aspen Plus flowsheet that integrates ethanol recovery, hydrogen management and product separation. Coupled life-cycle and techno-economic analyses will deliver energy balances, environmental footprints and the minimum methanol selling price, enabling a head-to-head comparison with conventional syngas routes.

REFERENCES

[1] W. Gao, S. Liang, R. Wang, Q. Jiang, Y. Zhang, Q. Zheng, B. Xie, C.Y. Toe, X. Zhu, J. Wang, L. Huang, Y. Gao, Z. Wang, C. Jo, Q. Wang, L. Wang, Y. Liu, B. Louis, J. Scott, A.-C. Roger, R. Amal, H. He, S.-E. Park, Industrial carbon dioxide capture and utilization: state of the art and future challenges, *Chemical Society Reviews*, 49 (2020) 8584-8686. https://doi.org/10.1039/D0CS00025F

[2] P.R.a.M.R. Hannah Ritchie, CO_2 and Greenhouse Gas Emissions. (accessed 10 February 2025) https://ourworldindata.org/co2-and-greenhouse-gas-emissions

[3] Record carbon emissions highlight urgency of Global Greenhouse Gas Watch, World Meteorological Organization, 2024. https://doi.org/https://wmo.int/media/news/record-carbon-emissions-highlight-urgency-of-global-greenhouse-gas-watch

[4] A. Rafiee, K. Rajab Khalilpour, D. Milani, M. Panahi, Trends in CO_2 conversion and utilization: A review from process systems perspective, *Journal of Environmental Chemical Engineering*, 6 (2018) 5771-5794. https://doi.org/https://doi.org/10.1016/j.jece.2018.08.065

[5] M. Yabushita, R. Fujii, Y. Nakagawa, K. Tomishige, Thermodynamic and Catalytic Insights into Non-Reductive Transformation of CO_2 with Amines into Organic Urea Derivatives, *ChemCatChem*, 16 (2024) e202301342. https://doi.org/https://doi.org/10.1002/cctc.202301342

[6] M. Aresta, A. Dibenedetto, A. Angelini, Catalysis for the Valorization of Exhaust Carbon: from CO_2 to Chemicals, Materials, and Fuels. Technological Use of CO_2, *Chemical Reviews*, 114 (2014) 1709-1742. https://doi.org/10.1021/cr4002758

[7] W. Wang, S. Wang, X. Ma, J. Gong, Recent advances in catalytic hydrogenation of carbon dioxide, *Chemical Society Reviews*, 40 (2011) 3703-3727. https://doi.org/10.1039/C1CS15008A

[8] A. Beck, M.A. Newton, L.G.A. van de Water, J.A. van Bokhoven, The Enigma of Methanol Synthesis by Cu/ZnO/Al_2O_3-Based Catalysts, *Chemical Reviews*, 124 (2024) 4543-4678. https://doi.org/10.1021/acs.chemrev.3c00148

[9] A. Goeppert, M. Czaun, J.-P. Jones, G.K. Surya Prakash, G.A. Olah, Recycling of carbon dioxide to methanol and derived products – closing the loop, *Chemical Society Reviews*, 43 (2014) 7995-8048. https://doi.org/10.1039/C4CS00122B

[10] Methanol Investor Presentation March 2024, Methanex Corporation. https://doi.org/https://www.methanex.com/wp-content/uploads/MEOH-Investor-Presentation-March-2024.pdf

[11] J. Artz, T.E. Müller, K. Thenert, J. Kleinekorte, R. Meys, A. Sternberg, A. Bardow, W. Leitner, Sustainable Conversion of Carbon Dioxide: An Integrated Review of Catalysis and Life Cycle Assessment, *Chemical Reviews*, 118 (2018) 434-504. https://doi.org/10.1021/acs.chemrev.7b00435

[12] Y.-M. Liu, J.-T. Liu, S.-Z. Liu, J. Li, Z.-H. Gao, Z.-J. Zuo, W. Huang, Reaction mechanisms of methanol synthesis from CO/CO_2 hydrogenation on Cu_2O(111): Comparison with Cu(111), *Journal of CO2 Utilization*, 20 (2017) 59-65. https://doi.org/https://doi.org/10.1016/j.jcou.2017.05.005

[13] M. Behrens, F. Studt, I. Kasatkin, S. Kühl, M. Hävecker, F. Abild-Pedersen, S. Zander, F. Girgsdies, P. Kurr, B.-L. Kniep, M. Tovar, R.W. Fischer, J.K. Nørskov, R. Schlögl, The Active Site of Methanol Synthesis over Cu/ZnO/Al_2O_3 Industrial Catalysts, *Science*, 336 (2012) 893-897. https://doi.org/doi:10.1126/science.1219831

[14] K. Chang, T. Wang, J.G. Chen, Hydrogenation of CO_2 to methanol over CuCeTiOx catalysts, *Applied Catalysis B: Environmental*, 206 (2017) 704-711. https://doi.org/https://doi.org/10.1016/j.apcatb.2017.01.076

[15] A. Karelovic, P. Ruiz, The role of copper particle size in low pressure methanol synthesis via CO_2 hydrogenation over Cu/ZnO catalysts, *Catalysis Science & Technology*, 5 (2015) 869-881. https://doi.org/10.1039/C4CY00848K

[16] P. Gao, F. Li, H. Zhan, N. Zhao, F. Xiao, W. Wei, L. Zhong, H. Wang, Y. Sun, Influence of Zr on the performance of Cu/Zn/Al/Zr catalysts via hydrotalcite-like precursors for CO_2 hydrogenation to methanol, *Journal of Catalysis*, 298 (2013) 51-60. https://doi.org/https://doi.org/10.1016/j.jcat.2012.10.030

[17] M. Behrens, S. Zander, P. Kurr, N. Jacobsen, J. Senker, G. Koch, T. Ressler, R.W. Fischer, R. Schlögl, Performance Improvement of Nanocatalysts by Promoter-Induced Defects in the Support Material: Methanol Synthesis over Cu/ZnO:Al, *Journal of the American Chemical Society*, 135 (2013) 6061-6068. https://doi.org/10.1021/ja310456f

[18] A.A. Kiss, J.J. Pragt, H.J. Vos, G. Bargeman, M.T. de Groot, Novel efficient process for methanol synthesis by CO_2 hydrogenation, *Chemical Engineering Journal*, 284 (2016) 260-269. https://doi.org/10.1016/j.cej.2015.08.101

[19] S. Kattel, P. Liu, J.G. Chen, Tuning Selectivity of CO($_2$) Hydrogenation Reactions at the Metal/Oxide Interface, *J Am Chem Soc*, 139 (2017) 9739-9754. https://doi.org/10.1021/jacs.7b05362

[20] L.C. Grabow, M. Mavrikakis, Mechanism of Methanol Synthesis on Cu through CO_2 and CO Hydrogenation, *ACS Catalysis*, 1 (2011) 365-384. https://doi.org/10.1021/cs200055d

[21] N. Tsubaki, M. Ito, K. Fujimoto, A New Method of Low-Temperature Methanol Synthesis, *Journal of Catalysis*, 197 (2001) 224-227. https://doi.org/10.1006/jcat.2000.3077

[22] R. Yang, Y. Fu, Y. Zhang, N. Tsubaki, In situ DRIFT study of low-temperature methanol synthesis mechanism on Cu/ZnO catalysts from CO-containing syngas using ethanol promoter, *Journal of Catalysis*, 228 (2004) 23-35. https://doi.org/10.1016/j.jcat.2004.08.017

[23] Y. Jeong, I. Kim, J.Y. Kang, H. Jeong, J.K. Park, J.H. Park, J.C. Jung, Alcohol-assisted low temperature methanol synthesis from syngas over Cu/ZnO catalysts: Effect of pH value in the co-precipitation step, *Journal of Molecular Catalysis A: Chemical*, 400 (2015) 132-138. https://doi.org/https://doi.org/10.1016/j.molcata.2015.01.008

[24] Y. Jeong, I. Kim, J.Y. Kang, N. Yan, H. Jeong, J.K. Park, J.H. Park, J.C. Jung, Effect of the aging time of the precipitate on the activity of Cu/ZnO catalysts for alcohol-assisted low temperature methanol synthesis, *Journal of Molecular Catalysis A: Chemical*, 418-419 (2016) 168-174. https://doi.org/https://doi.org/10.1016/j.molcata.2016.03.044

[25] I. Kim, G. Lee, H. Jeong, J.H. Park, J.C. Jung, Bifunctionality of Cu/ZnO catalysts for alcohol-assisted low-temperature methanol synthesis from syngas: Effect of copper content, *Journal of Energy Chemistry*, 26 (2017) 373-379. https://doi.org/https://doi.org/10.1016/j.jechem.2017.02.003

[26] S. Likhittaphon, R. Panyadee, W. Fakyam, S. Charojrochkul, T. Sornchamni, N. Laosiripojana, S. Assabumrungrat, P. Kim-Lohsoontorn, Effect of CuO/ZnO catalyst preparation condition on alcohol-assisted methanol synthesis from carbon dioxide and hydrogen, *International Journal of Hydrogen Energy*, 44 (2019) 20782-20791. https://doi.org/https://doi.org/10.1016/j.ijhydene.2018.07.021

[27] T. Boonamnuay, N. Laosiripojana, S. Assabumrungrat, P. Kim-Lohsoontorn, Effect 3A and 5A molecular sieve on alcohol-assisted methanol synthesis from CO_2 and H_2 over Cu/ZnO catalyst, *International Journal of Hydrogen Energy*, 46 (2021) 30948-30958. https://doi.org/https://doi.org/10.1016/j.ijhydene.2021.04.161

[28] Y. Chen, S. Choi, L.T. Thompson, Low-Temperature CO_2 Hydrogenation to Liquid Products via a Heterogeneous Cascade Catalytic System, *ACS Catalysis*, 5 (2015) 1717-1725. https://doi.org/10.1021/cs501656x

[29] J. Kothandaraman, D.J. Heldebrant, Towards environmentally benign capture and conversion: heterogeneous metal catalyzed CO_2 hydrogenation in CO_2 capture solvents, *Green Chemistry*, 22 (2020) 828-834. https://doi.org/10.1039/C9GC03449H

[30] S. Xie, W. Zhang, C. Jia, S.S.G. Ong, C. Zhang, S. Zhang, H. Lin, Eliminating carbon dioxide emissions at the source by the integration of carbon dioxide capture and utilization over noble metals in the liquid phase, *Journal of Catalysis*, 389 (2020) 247-258. https://doi.org/https://doi.org/10.1016/j.jcat.2020.06.001

[31] Y. Jeong, J.Y. Kang, I. Kim, H. Jeong, J.K. Park, J.H. Park, J.C. Jung, Preparation of Cu/ZnO catalyst using a polyol method for alcohol-assisted low temperature methanol synthesis from syngas, *Korean Journal of Chemical Engineering*, 33 (2016) 114-119. https://doi.org/10.1007/s11814-015-0118-7

[32] S. Meesattham, P. Kim-Lohsoontorn, Low-temperature alcohol-assisted methanol synthesis from CO_2 and H_2: The effect of alcohol type, *International Journal of Hydrogen Energy*, 47 (2022) 22691-22703. https://doi.org/10.1016/j.ijhydene.2022.05.083

[33] Y. Chen, S. Choi, L.T. Thompson, Ethyl formate hydrogenolysis over Mo2C-based catalysts: Towards low temperature CO and CO2 hydrogenation to methanol, *Catalysis Today*, 259 (2016) 285-291. https://doi.org/https://doi.org/10.1016/j.cattod.2015.08.021

[34] H. Nieminen, G. Givirovskiy, A. Laari, T. Koiranen, Alcohol promoted methanol synthesis enhanced by adsorption of water and dual catalysts, *Journal of CO2 Utilization*, 24 (2018) 180-189. https://doi.org/https://doi.org/10.1016/j.jcou.2018.01.002

[35] J. Kothandaraman, R.A. Dagle, V.L. Dagle, S.D. Davidson, E.D. Walter, S.D. Burton, D.W. Hoyt, D.J. Heldebrant, Condensed-phase low temperature heterogeneous hydrogenation of CO2 to methanol, *Catalysis Science & Technology*, 8 (2018) 5098-5103. https://doi.org/10.1039/C8CY00997J

[36] S. Hanukovich, A. Dang, P. Christopher, Influence of Metal Oxide Support Acid Sites on Cu-Catalyzed Nonoxidative Dehydrogenation of Ethanol to Acetaldehyde, *ACS Catalysis*, 9 (2019) 3537-3550. https://doi.org/10.1021/acscatal.8b05075

[37] S.W. Colley, J. Tabatabaei, K.C. Waugh, M.A. Wood, The detailed kinetics and mechanism of ethyl ethanoate synthesis over a Cu/Cr2O3 catalyst, *Journal of Catalysis*, 236 (2005) 21-33. https://doi.org/https://doi.org/10.1016/j.jcat.2005.09.012

[38] R. Wu, K. Sun, Y. Chen, M. Zhang, L. Wang, Ethanol dimerization to Ethyl acetate and hydrogen on the multifaceted copper catalysts, *Surface Science*, 703 (2021) 121742. https://doi.org/https://doi.org/10.1016/j.susc.2020.121742

[39] T.K. Phung, Copper-based catalysts for ethanol dehydrogenation and dehydrogenative coupling into hydrogen, acetaldehyde and ethyl acetate, *International Journal of Hydrogen Energy*, 47 (2022) 42234-42249. https://doi.org/10.1016/j.ijhydene.2021.11.253

[40] N.D. Nielsen, A.D. Jensen, J.M. Christensen, The roles of CO and CO2 in high pressure methanol synthesis over Cu-based catalysts, *Journal of Catalysis*, 393 (2021) 324-334. https://doi.org/https://doi.org/10.1016/j.jcat.2020.11.035

[41] M. Kurtz, H. Wilmer, T. Genger, O. Hinrichsen, M. Muhler, Deactivation of Supported Copper Catalysts for Methanol Synthesis, *Catalysis Letters*, 86 (2003) 77-80. https://doi.org/10.1023/A:1022663125977

[42] S. Chang, W. Na, J. Zhang, L. Lin, W. Gao, Effect of the Zn/Ce ratio in Cu/ZnO–CeO_2 catalysts on CO_2 hydrogenation for methanol synthesis, *New Journal of Chemistry*, 45 (2021) 22814-22823. https://doi.org/10.1039/D1NJ04951H

[43] P. Min, S. Zhang, Y. Xu, R. Li, Enhanced oxygen storage capacity of CeO2 with doping-induced unstable crystal structure, *Applied Surface Science*, 448 (2018) 435-443. https://doi.org/https://doi.org/10.1016/j.apsusc.2018.04.103

[44] R. Ye, L. Ma, J. Mao, X. Wang, X. Hong, A. Gallo, Y. Ma, W. Luo, B. Wang, R. Zhang, M.S. Duyar, Z. Jiang, J. Liu, A Ce-CuZn catalyst with abundant Cu/Zn-O(V)-Ce active sites for CO($_2$) hydrogenation to methanol, *Nat Commun*, 15 (2024) 2159. https://doi.org/10.1038/s41467-024-46513-3

[45] J. Zhu, Y. Su, J. Chai, V. Muravev, N. Kosinov, E.J.M. Hensen, Mechanism and Nature of Active Sites for Methanol Synthesis from CO/CO_2 on Cu/CeO_2, *ACS Catalysis*, 10 (2020) 11532-11544. https://doi.org/10.1021/acscatal.0c02909

[46] H.-X. Liu, S.-Q. Li, W.-W. Wang, W.-Z. Yu, W.-J. Zhang, C. Ma, C.-J. Jia, Partially sintered copper–ceria as excellent catalyst for the high-temperature reverse water gas shift reaction, *Nature Communications*, 13 (2022) 867. https://doi.org/10.1038/s41467-022-28476-5

[47] R. Singh, K. Kundu, K.K. Pant, CO2 hydrogenation to methanol over Cu-ZnO-CeO_2 catalyst: Reaction structure–activity relationship, optimizing Ce and Zn ratio, and kinetic study, *Chemical Engineering Journal*, 479 (2024) 147783. https://doi.org/https://doi.org/10.1016/j.cej.2023.147783

doi:10.6342/NTU202502278

[48] A. Chen, X. Yu, Y. Zhou, S. Miao, Y. Li, S. Kuld, J. Sehested, J. Liu, T. Aoki, S. Hong, M.F. Camellone, S. Fabris, J. Ning, C. Jin, C. Yang, A. Nefedov, C. Wöll, Y. Wang, W. Shen, Structure of the catalytically active copper–ceria interfacial perimeter, *Nature Catalysis*, 2 (2019) 334-341. https://doi.org/10.1038/s41929-019-0226-6

[49] J.A. Rodriguez, P. Liu, D.J. Stacchiola, S.D. Senanayake, M.G. White, J.G. Chen, Hydrogenation of CO_2 to Methanol: Importance of Metal–Oxide and Metal–Carbide Interfaces in the Activation of CO_2, *ACS Catalysis*, 5 (2015) 6696-6706. https://doi.org/10.1021/acscatal.5b01755

[50] Y. Yu, Z. Bian, Z. Wang, J. Wang, W. Tan, Q. Zhong, S. Kawi, CO_2 methanation on Ni-$Ce_{0.8}M_{0.2}O_2$ (M=Zr, Sn or Ti) catalyst: Suppression of CO via formation of bridging carbonyls on nickel, *Catalysis Today*, 424 (2023) 113053. https://doi.org/https://doi.org/10.1016/j.cattod.2020.07.049

[51] T. Phongamwong, U. Chantaprasertporn, T. Witoon, T. Numpilai, Y. Poo-arporn, W. Limphirat, W. Donphai, P. Dittanet, M. Chareonpanich, J. Limtrakul, CO2 hydrogenation to methanol over CuO–ZnO–ZrO2–SiO2 catalysts: Effects of SiO2 contents, *Chemical Engineering Journal*, 316 (2017) 692-703. https://doi.org/https://doi.org/10.1016/j.cej.2017.02.010

[52] W. Wang, Z. Qu, L. Song, Q. Fu, CO2 hydrogenation to methanol over Cu/CeO2 and Cu/ZrO2 catalysts: Tuning methanol selectivity via metal-support interaction, *Journal of Energy Chemistry*, 40 (2020) 22-30. https://doi.org/https://doi.org/10.1016/j.jechem.2019.03.001

[53] G. Noh, E. Lam, D.T. Bregante, J. Meyet, P. Šot, D.W. Flaherty, C. Copéret, Lewis Acid Strength of Interfacial Metal Sites Drives CH_3OH Selectivity and Formation Rates on Cu-Based CO_2 Hydrogenation Catalysts, *Angewandte Chemie International Edition*, 60 (2021) 9650-9659. https://doi.org/https://doi.org/10.1002/anie.202100672

[54] J. Zhu, D. Ciolca, L. Liu, A. Parastaev, N. Kosinov, E.J.M. Hensen, Flame Synthesis of Cu/ZnO-CeO(2) Catalysts: Synergistic Metal-Support Interactions Promote CH(3)OH Selectivity in CO(2) Hydrogenation, *ACS Catal*, 11 (2021) 4880-4892. https://doi.org/10.1021/acscatal.1c00131

[55] T. Takeguchi, S. Manabe, R. Kikuchi, K. Eguchi, T. Kanazawa, S. Matsumoto, W. Ueda, Determination of dispersion of precious metals on CeO2-containing supports, *Applied Catalysis A: General*, 293 (2005) 91-96. https://doi.org/https://doi.org/10.1016/j.apcata.2005.07.013

[56] T. Shido, Y. Iwasawa, Reactant-promoted reaction mechanism for water-gas shift reaction on ZnO, as the genesis of surface catalysis, *Journal of Catalysis*, 129 (1991) 343-355. https://doi.org/https://doi.org/10.1016/0021-9517(91)90040-B

[57] J.F. Edwards, G.L. Schrader, In situ fourier transform infrared study of methanol synthesis on mixed metal oxide catalysts, *Journal of Catalysis*, 94 (1985) 175-186.
https://doi.org/https://doi.org/10.1016/0021-9517(85)90093-4

[58] Z.-J. Gong, Y.-R. Li, H.-L. Wu, S.D. Lin, W.-Y. Yu, Direct copolymerization of carbon dioxide and 1,4-butanediol enhanced by ceria nanorod catalyst, *Applied Catalysis B: Environmental*, 265 (2020) 118524.
https://doi.org/https://doi.org/10.1016/j.apcatb.2019.118524

[59] G.N. Vayssilov, M. Mihaylov, P.S. Petkov, K.I. Hadjiivanov, K.M. Neyman, Reassignment of the Vibrational Spectra of Carbonates, Formates, and Related Surface Species on Ceria: A Combined Density Functional and Infrared Spectroscopy Investigation, *The Journal of Physical Chemistry C*, 115 (2011) 23435-23454.
https://doi.org/10.1021/jp208050a

[60] C. Li, Y. Sakata, T. Arai, K. Domen, K.-i. Maruya, T. Onishi, Carbon monoxide and carbon dioxide adsorption on cerium oxide studied by Fourier-transform infrared spectroscopy. Part 1.—Formation of carbonate species on dehydroxylated CeO2, at room temperature, *Journal of the Chemical Society, Faraday Transactions 1: Physical Chemistry in Condensed Phases*, 85 (1989) 929-943.
https://doi.org/10.1039/F19898500929

[61] Y. Zhang, L. Liang, Z. Chen, J. Wen, W. Zhong, S. Zou, M. Fu, L. Chen, D. Ye, Highly efficient Cu/CeO2-hollow nanospheres catalyst for the reverse water-gas shift reaction: Investigation on the role of oxygen vacancies through in situ UV-Raman and DRIFTS, *Applied Surface Science*, 516 (2020) 146035.
https://doi.org/https://doi.org/10.1016/j.apsusc.2020.146035

[62] O. Pozdnyakova, D. Teschner, A. Wootsch, J. Kröhnert, B. Steinhauer, H. Sauer, L. Toth, F.C. Jentoft, A. Knop-Gericke, Z. Paál, R. Schlögl, Preferential CO oxidation in hydrogen (PROX) on ceria-supported catalysts, part I: Oxidation state and surface species on Pt/CeO2 under reaction conditions, *Journal of Catalysis*, 237 (2006) 1-16.
https://doi.org/https://doi.org/10.1016/j.jcat.2005.10.014

[63] K. Mudiyanselage, A.E. Baber, Z. Liu, S.D. Senanayake, D.J. Stacchiola, Isolation and characterization of formates on CeOx–CuyO/Cu(111), *Catalysis Today*, 240 (2015) 190-200.
https://doi.org/https://doi.org/10.1016/j.cattod.2014.06.001

[64] S.M. Fehr, K. Nguyen, I. Krossing, Realistic Operando-DRIFTS Studies on Cu/ZnO Catalysts for CO2 Hydrogenation to Methanol – Direct Observation of Mono-ionized Defect Sites and Implications for Reaction Intermediates, *ChemCatChem*, 14 (2022) e202101500.
https://doi.org/https://doi.org/10.1002/cctc.202101500

doi:10.6342/NTU202502278

[65] A.I.M. Rabee, H. Abed, T.H. Vuong, S. Bartling, L. Kraußer, H. Atia, N. Rockstroh, E.V. Kondratenko, A. Brückner, J. Rabeah, CeO2-Supported Single-Atom Cu Catalysts Modified with Fe for RWGS Reaction: Deciphering the Role of Fe in the Reaction Mechanism by In Situ/Operando Spectroscopic Techniques, *ACS Catalysis*, 14 (2024) 10913-10927. https://doi.org/10.1021/acscatal.4c01493

[66] A. Yee, S.J. Morrison, H. Idriss, The reactions of ethanol over M/CeO_2 catalysts: Evidence of carbon–carbon bond dissociation at low temperatures over Rh/CeO_2, *Catalysis Today*, 63 (2000) 327-335. https://doi.org/https://doi.org/10.1016/S0920-5861(00)00476-4

[67] M.H. Brijaldo, H.A. Rojas, J.J. Martínez, F.B. Passos, Effect of support on acetic acid decomposition over palladium catalysts, *Journal of Catalysis*, 331 (2015) 63-75. https://doi.org/https://doi.org/10.1016/j.jcat.2015.08.019

[68] S.W. Charles, G.I.L. Jones, N.L. Owen, S.J. Cyvin, B.N. Cyvin, The vibrational spectra, rotational isomerism, normal coordinate analysis and mean amplitudes of ethyl formate, ethyl chloroformate and ethyl cyanoform, *Journal of Molecular Structure*, 16 (1973) 225-257. https://doi.org/https://doi.org/10.1016/0022-2860(73)80064-X

[69] D.M. Monti, N.W. Cant, D.L. Trimm, M.S. Wainwright, Hydrogenolysis of methyl formate over copper on silica: II. Study of the mechanism using labeled compounds, *Journal of Catalysis*, 100 (1986) 28-38. https://doi.org/https://doi.org/10.1016/0021-9517(86)90068-0

[70] J. Kim, B.B. Sarma, E. Andrés, N. Pfänder, P. Concepción, G. Prieto, Surface Lewis Acidity of Periphery Oxide Species as a General Kinetic Descriptor for CO2 Hydrogenation to Methanol on Supported Copper Nanoparticles, *ACS Catalysis*, 9 (2019) 10409-10417. https://doi.org/10.1021/acscatal.9b02412

[71] S.D. Senanayake, P.J. Ramírez, I. Waluyo, S. Kundu, K. Mudiyanselage, Z. Liu, Z. Liu, S. Axnanda, D.J. Stacchiola, J. Evans, J.A. Rodriguez, Hydrogenation of CO2 to Methanol on CeOx/Cu(111) and ZnO/Cu(111) Catalysts: Role of the Metal–Oxide Interface and Importance of Ce3+ Sites, *The Journal of Physical Chemistry C*, 120 (2016) 1778-1784. https://doi.org/10.1021/acs.jpcc.5b12012

[72] J. Zhang, K. Shi, Y. Zhu, Z. An, W. Wang, X. Ma, X. Shu, H. Song, X. Xiang, J. He, Interfacial Sites in Ag Supported Layered Double Oxide for Dehydrogenation Coupling of Ethanol to n-Butanol, *ChemistryOpen*, 10 (2021) 1095-1103. https://doi.org/https://doi.org/10.1002/open.202000295

[73] H. Idriss, C. Diagne, J.P. Hindermann, A. Kiennemann, M.A. Barteau, Reactions of Acetaldehyde on CeO_2 and CeO_2-Supported Catalysts, *Journal of Catalysis*, 155 (1995) 219-237. https://doi.org/https://doi.org/10.1006/jcat.1995.1205

[74] M. Kourtelesis, T.S. Moraes, L.V. Mattos, D.K. Niakolas, F.B. Noronha, X. Verykios, The effects of support morphology on the performance of Pt/CeO_2 catalysts for the low temperature steam reforming of ethanol, *Applied Catalysis B: Environmental*, 284 (2021) 119757. https://doi.org/https://doi.org/10.1016/j.apcatb.2020.119757

[75] J.R. Jensen, T. Johannessen, H. Livbjerg, An improved N_2O-method for measuring Cu-dispersion, *Applied Catalysis A: General*, 266 (2004) 117-122. https://doi.org/https://doi.org/10.1016/j.apcata.2004.02.009

APPENDICES

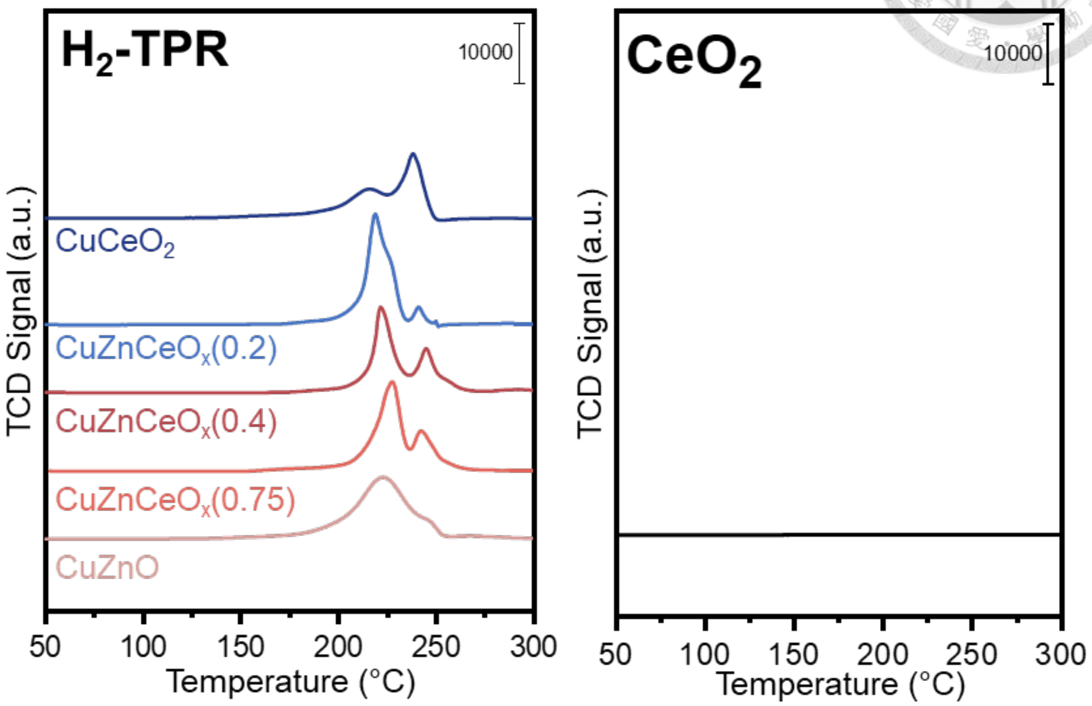

Appendix 1 H_2-TPR profile of Cu-supported catalyst compared to CeO_2.

doi:10.6342/NTU202502278

Appendix 2 H_2-TPR + N_2O flow for Cu dispersion measurement

The dispersion of surface Cu species is commonly evaluated by selectively oxidation of metallic Cu in a flow of N_2O, followed by a second H_2-TPR, by assuming that N_2O only oxidizes Cu into Cu_2O due to its relatively weaker oxidation capability compared to O_2 at low temperatures.[75] In the 1st H_2-TPR, the consumption of H_2 is attributed to the reduction of bulk CuO to metallic Cu. The consumption of H_2 in the 2nd H_2-TPR is corresponded to the reduction of surface oxidized Cu_2O due to the oxidation of N_2O.

However, this study demonstrates that this approach is not applicable to catalysts containing reducible supports or promoters such as CeO_2.

$$CuO + H_2 \rightarrow Cu^0 + H_2O \ (Cu:H_2 = 1:1)$$

$$2Cu^0 + N_2O \rightarrow Cu_2O + N_2 \ (Cu:N_2O = 2:1)$$

$$Cu_2O + H_2 \rightarrow 2Cu + H_2O \ (Cu:H_2 = 2:1)$$

Detailed procedures:

1. Pretrement:

- 50 mg of the calcined catalyst was heated in a rate of 10 °C/min to 300 °C for 10 minutes under an Ar flow of 50 mL/min to remove the moisture and impurities.
- The sample was cooled down to 50 °C while maintaining the Ar flow.
- A 50 mL/min of 10% H_2/Ar was introduced, and the TCD signal was allowed to stabilize for 30 minutes.

2. 1st H_2-TPR:

- The sample was heated to 300 °C at a rate of 5 °C/min under a 50 mL/min flow of 10% H_2/Ar.

3. N_2O oxidation:

- The sample was cooled down to 50 °C while maintaining the Ar flow.
- 50 mL/min of N_2O was introduced to the sample for 30 minutes.
- 50 mL/min of Ar was then used to purge the N_2O for 30 minutes.

4. 2nd H_2-TPR:

- A 50 mL/min of 10% H_2/Ar was introduced, and the TCD signal was allowed to stabilize for 30 minutes.
- The sample was heated to 300 °C at a rate of 5 °C/min under a 50 mL/min flow of 10% H_2/Ar.

For the CuZnO, $CuZnCeO_x$(0.2), and $CuZnCeO_x$(0.4) catalysts, the second H_2-TPR exhibited a notable decrease in both reduction peak area and temperature compared to the initial TPR. This observation aligns with previous reports [44,75], where N_2O selectively oxidizes only the surface-exposed Cu^0 species, leaving subsurface or embedded copper largely unoxidized. Consequently, only a portion of the total copper content participates in re-reduction, leading to a diminished H_2 uptake during the second TPR. Furthermore, the re-oxidized surface Cu species, being more finely dispersed and weakly coordinated, are more easily reduced, resulting in a shift of the reduction peak to lower temperatures. This behavior is consistent with the selective formation of Cu_2O upon N_2O treatment.

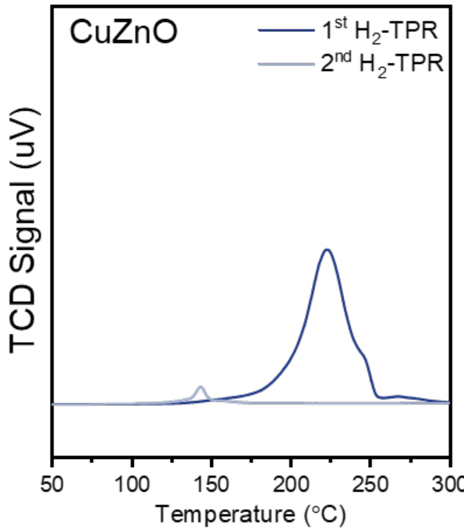

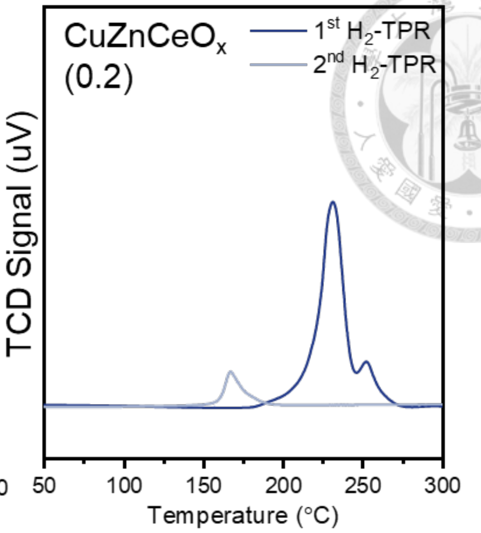

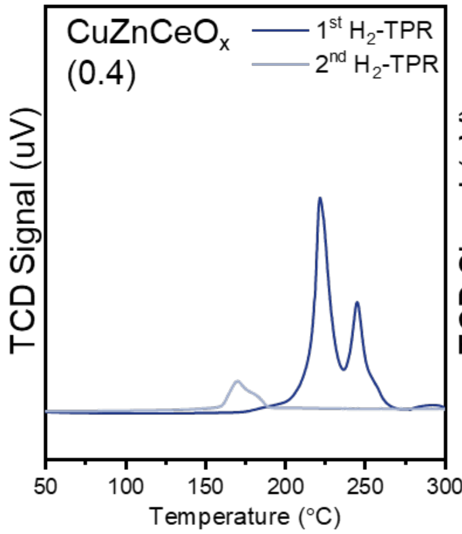

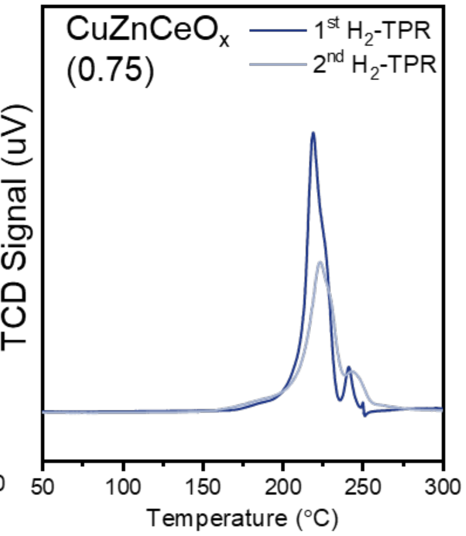

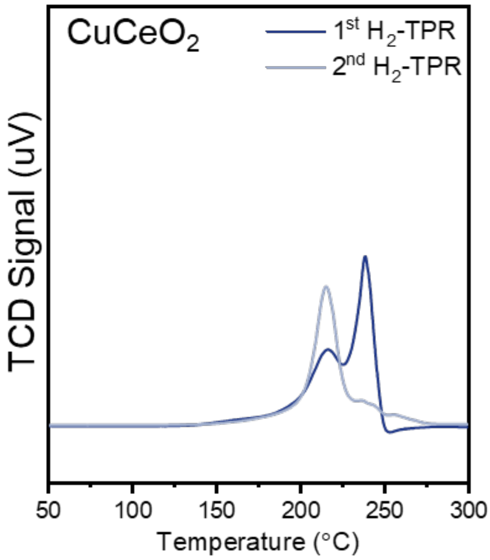

doi:10.6342/NTU202502278

In contrast, the $CuZnCeO_x$(0.75) and $CuCeO_2$ samples exhibited a markedly different behavior. The reduction peak area and temperature in the second H_2-TPR were similar to those observed in the first cycle, suggesting a non-selective oxidation process. Notable, the H_2 consumption during the second TPR was nearly twice the theoretical value expected if Cu were oxidized only to Cu^+ (i.e. Cu_2O). However, when assuming full oxidation to Cu^{2+} (i.e. CuO), the calculated H_2/Cu ratio was only slightly above unity, that is more consistent with expected stoichiometry and thus considered a more reliable scenario. This indicates that in the presence of CeO_2, N_2O oxidizes Cu beyond Cu^+ to Cu^{2+}.

To further validate this hypothesis, a control experiment was performed using O_2 in place of N_2O for the oxidation step using $CuCeO_2$ as the catalyst sample. The resulting H_2 consumption in the 2nd H_2-TPR was similar using either N_2O or O_2 as the oxidant, supporting the hypothesis that Cu in the Ce-containing catalyst was fully oxidized to Cu^{2+} under both conditions. Overall, the findings highlight that sequential H_2-TPR and N_2O oxidation cannot reliably quantify Cu dispersion in the presence of reducible oxides like CeO_2, as the strong metal-support interactions promote complete oxidation of Cu to Cu^{2+} rather than selective surface oxidation.

Amount of H_2 consumed and H_2/Cu Ratio in the sequential H_2-TPR and oxidation experiments of $CuCeO_2$.

	H_2 consumption (mmol)		H_2/Cu ratio	
	1st TPR	2nd TPR	1st TPR	2nd TPR
H_2-N_2O-H_2	0.2634	0.2322	1.34	1.18
H_2-O_2-H_2	0.2715	0.2170	1.57	1.10

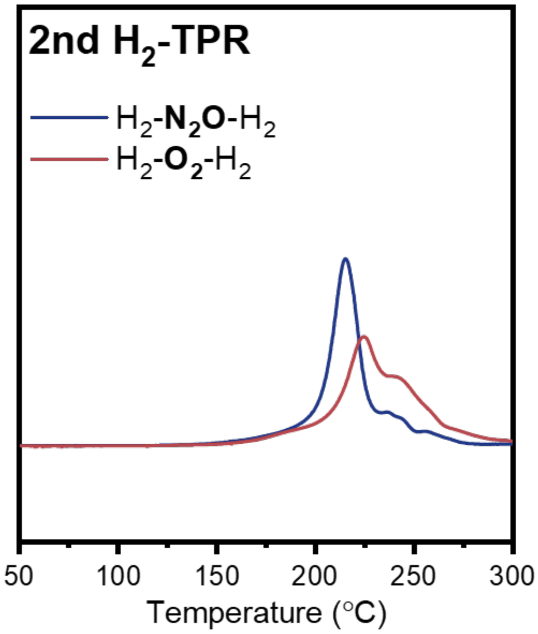

Comparison of 2nd H_2-TPR profile of $CuCeO_2$ after N_2O and O_2 oxidation.

doi:10.6342/NTU202502278

Catalytic Activity Test – $CuZnO_x$ vs $CuCeO_x$ (**Figure 3.10**)

Reaction Condition: 180 °C, 30 bar at room temperature ($H_2/CO_2 = 3$), 0.4 g catalysts, 20 mL EtOH in 100 mL reactor.

Appendix 3 Carbon balance of catalytic activity test of CuZnO vs $CuCeO_2$.

Catalyst	Carbon in (mmol)		Carbon out (mmol)							Balance (%)[e]
	CO_2	EtOH	CO_2	EtOH	MeOH	EtFm[a]	MeCHO[b]	EtAc[c]	CO[d]	
CuZnO (6 h)	25.5	685	26.0	532	0.16	0.79	0.01	1.02	0.24	78.8
CuZnO (12 h)	25.5	685	21.7	529	1.13	1.91	0.01	4.00	0.61	78.6
$CuCeO_2$ (6 h)	25.5	685	26.7	534	0.16	2.53	0.01	0.52	0.22	79.4
$CuCeO_2$ (12 h)	25.5	685	27.0	547	0.37	2.80	0.05	0.79	0.33	81.4

[a] CO_2 hydrogenation (main reaction): $CO_2 + 3H_2 \rightarrow CH_3OH + H_2O$

$CO_2 + \frac{1}{2} H_2 + Cu \rightarrow HCOOCu$

$HCOOCu + C_2H_5OH \rightarrow HCOOC_2H_5$ (EtFm) + CuOH

$HCOO_2H_5 + 2H_2 \rightarrow C_2H_5OH + CH_3OH$

$CuOH + \frac{1}{2} H_2 \rightarrow H_2O + Cu$

[b] Ethanol dehydrogenation (side reaction): $C_2H_5OH \rightarrow CH_3CHO$ (MeCHO) + H_2

[c] Ethanol coupling (side reaction): $C_2H_5OH + CH_3CHO \rightarrow CH_3COOC_2H_5$ (EtAc) + H_2

[d] Reverse water gas shift reaction (side reaction): $CO_2 + H_2 \rightarrow CO + H_2O$

[e] Carbon balance (%) = (Carbon Out)/(Carbon in) × 100%

Appendix 4 Ethanol balance of catalytic activity test of CuZnO vs $CuCeO_2$.

Catalyst	Input (mmol)	Output (mmol)				Balance (%)[a]
	EtOH	EtOH	EtFm	MeCHO	EtAc	
CuZnO (6 h)	342.5	265.8	0.264	0.005	0.255	77.7
CuZnO (12 h)	342.5	264.7	0.635	0.003	1.001	77.8
$CuCeO_2$ (6 h)	342.5	267.0	0.844	0.005	0.130	78.2
$CuCeO_2$ (12 h)	342.5	273.6	0.932	0.026	0.199	80.2

[a] Ethanol balance (%) = (Output)/(Input) × 100%

Appendix 5 Hydrogen balance of catalytic activity of CuZnO vs $CuCeO_2$.

Catalyst	Input (mmol)			Output (mmol)				Balance (%)[a]
	H_2 feed	MeCHO	EtAc	H_2 remained	MeOH	EtFm	CO	
CuZnO (6 h)	67.7	0.005	0.255	66.3	0.47	0.264	0.245	99.0
CuZnO (12 h)	67.7	0.003	1.001	55.8	3.39	0.635	0.611	93.8
$CuCeO_2$ (6 h)	67.7	0.005	0.130	63.3	0.47	0.844	0.222	95.6
$CuCeO_2$ (12 h)	67.7	0.026	0.199	60.4	1.12	0.932	0.331	92.4

[a] Hydrogen balance (%) = (Output)/(Input) × 100%

Catalytic Activity Test (**Table 3.7 & Figure 3.11**)

Reaction Condition:180 °C, 30 bar at room temperature ($H_2/N_2 = 3$), 0.4 g catalysts, 20 mL EtOH and 5 mmol (400 μL) EtFm in 100 mL reactor.

Appendix 6 Carbon balance of catalytic activity tests of catalysts with different Ce/(Ce+Zn).

Catalyst	Carbon in (mmol)		Carbon Out (mmol)							Balance (%)[f]
	CO_2	EtOH	CO_2	EtOH	MeOH	EtFm[a]	MeCHO[b]	EtAc[c]	CO[d]	
CuZnO	25.5	685	21.7	529	1.13	1.90	0.01	4.00	0.61	78.6
$CuZnCeO_x$ (0.2)	25.5	685	23.8	521	2.66	1.63	0.02	3.45	0.54	77.9
$CuZnCeO_x$ (0.4)	25.5	685	24.4	542	1.98	2.27	0.03	2.63	0.34	80.7
$CuZnCeO_x$ (0.75)	25.5	685	21.5	539	1.16	2.25	0.04	1.96	0.21	79.7
$CuCeO_2$	25.5	685	27.0	547	0.37	2.80	0.05	0.79	0.33	81.4

[a] CO_2 hydrogenation (main reaction): $CO_2 + 3H_2 \rightarrow CH_3OH + H_2O$

$CO_2 + ½ H_2 + Cu \rightarrow HCOOCu$

$HCOOCu + C_2H_5OH \rightarrow HCOOC_2H_5$ (EtFm) + CuOH

$HCOO_2H_5 + 2H_2 \rightarrow C_2H_5OH + CH_3OH$

$CuOH + ½ H_2 \rightarrow H_2O + Cu$

[b] Ethanol dehydrogenation (side reaction): $C_2H_5OH \rightarrow CH_3CHO$ (MeCHO) + H_2

[c] Ethanol coupling (side reaction): $C_2H_5OH + CH_3CHO \rightarrow CH_3COOC_2H_5$ (EtAc) + H_2

[d] Reverse water gas shift reaction (side reaction): $CO_2 + H_2 \rightarrow CO + H_2O$

[e] Carbon balance (%) = (Carbon Out)/(Carbon in) × 100%

Appendix 7 Ethanol balance of catalytic activity tests of catalysts with different Ce/(Ce+Zn).

Catalyst	Input (mmol)	Output (mmol)				Balance (%)[a]
	EtOH	EtOH	EtFm	MeCHO	EtAc	
CuZnO	342.5	264.7	0.635	0.00	1.001	77.8
CuZnCeO$_x$ (0.2)	342.5	260.7	0.542	0.01	0.862	76.5
CuZnCeO$_x$ (0.4)	342.5	270.9	0.756	0.02	0.657	79.5
CuZnCeO$_x$ (0.75)	342.5	269.6	0.751	0.02	0.489	79.1
CuCeO$_2$	342.5	273.6	0.932	0.03	0.199	80.2

[a] Ethanol balance (%) = (Output)/(Input) × 100%

Appendix 8 Hydrogen balance of catalytic activity tests of catalysts with different Ce/(Ce+Zn).

Catalyst	Input (mmol)			Output (mmol)				Balance (%)[a]
	H_2 feed	MeCHO	EtAc	H_2 remained	MeOH	EtFm	CO	
CuZnO	67.7	0.003	1.001	58.8	3.39	0.635	0.611	93.8
CuZnCeO$_x$ (0.2)	67.7	0.009	0.862	59.1	7.98	0.542	0.401	97.7
CuZnCeO$_x$ (0.4)	67.7	0.017	0.657	61.3	5.94	0.756	0.544	98.8
CuZnCeO$_x$ (0.75)	67.7	0.020	0.489	63.7	3.49	0.751	0.341	100.1
CuCeO$_2$	67.7	0.026	0.199	60.4	1.12	0.932	0.331	96.8

[a] Hydrogen balance (%) = (Output)/(Input) × 100%

Appendix 9 Catalytic activity test results and balance for hydrogenolysis of ethyl formate.

Catalyst	Product (mmol)		EtFm Conv. (%)[a]	MeOH Yield (%)[b]	Balance (%)[c]
	MeOH	EtFm			
No catalyst	0.00	4.21	15.8	-	84.3
CuZnO	3.60	0.33	93.5	72.0	78.6
$CuZnCeO_x$ (0.2)	2.69	1.51	69.8	53.8	84.1
$CuZnCeO_x$ (0.4)	1.88	2.24	55.2	44.8	82.3
$CuZnCeO_x$ (0.75)	1.17	2.86	42.8	23.4	80.7
$CuCeO_2$	0.78	3.15	37.0	15.6	78.6

Reaction condition: 180 °C, 30 bar at room temperature ($H_2/N_2 = 3$), 12 h, 0.4 g catalysts, 20 mL EtOH and 5 mmol (400 μL) EtFm in 100 mL reactor.

Hydrogenolysis of EtFm: $HCOOC_2H_5 + 2H_2 \rightarrow CH_3OH + C_2H_5OH$

[a] EtFm conversion (%) = (5 – EtFm in product)/5 × 100%

[b] MeOH yield (%) = (MeOH in product)/5 × 100%

[c] Balance (%) = (EtFm in product + MeOH in product)/5 × 100%

doi:10.6342/NTU202502278

Appendix 10 Correlation of total EtFm yields with catalytic properties of CuZnCeO$_x$ catalysts.